



THE *SPITZER* INFRARED SPECTROGRAPH SURVEY OF PROTOPLANETARY DISKS IN ORION A. I. DISK PROPERTIES

K. H. KIM^{1,2}, DAN M. WATSON², P. MANOJ^{2,3}, W. J. FORREST², ELISE FURLAN⁴, JOAN NAJITA⁵, BENJAMIN SARGENT⁶, JESÚS HERNÁNDEZ^{7,14}, NURIA CALVET⁸, LUCÍA ADAME⁹, CATHERINE ESPAILLAT¹⁰, S. T. MEGEATH¹¹, JAMES MUZEROLLE¹², AND M. K. MCCLURE¹³

¹ Korea Astronomy and Space Science Institute (KASI), 776, Daedeokdae-ro, Yuseong-gu, Daejeon 305-348, Korea; quarkosmos@kasi.re.kr

² Department of Physics and Astronomy, University of Rochester, Rochester, NY 14627, USA

³ Department of Astronomy and Astrophysics, Tata Institute of Fundamental Research, Homi Bhabha Road, Mumbai 400 005, India

⁴ Infrared Processing and Analysis Center, Caltech, 770 S. Wilson Avenue, Pasadena, CA 91125, USA

⁵ National Optical Astronomy Observatory, 950 North Cherry Avenue, Tucson, AZ 85719, USA

⁶ Center for Imaging Science and Laboratory for Multiwavelength Astrophysics, Rochester Institute of Technology, 54 Lomb Memorial Dr., Rochester, NY 14623, USA

⁷ Centro de Investigaciones de Astronomía, Apdo. Postal 264, Mérida 5101-A, Venezuela

⁸ Department of Astronomy, University of Michigan, 830 Dennison Building, 500 Church Street, Ann Arbor, MI 48109, USA

⁹ Facultad de Ciencias Físico-Matemáticas, Universidad Autónoma de Nuevo León, Av. Universidad S/N, San Nicolás de los Garza, Nuevo León, C.P. 66451, México

¹⁰ Department of Astronomy, Boston University, 725 Commonwealth Avenue, Boston, MA 02215, USA

¹¹ Ritter Astrophysical Research Center, Department of Physics and Astronomy, University of Toledo, 2801 W. Bancroft St., Toledo, OH 43606, USA

¹² Space Telescope Science Institute, 3700 San Martin Drive, Baltimore, MD 21218, USA

¹³ ESO, Karl-Schwarzschild-Str. 2, D-85748, Garching bei München, Germany

¹⁴ Instituto de Astronomía, Universidad Nacional Autónoma de México, Unidad Académica en Ensenada, Ensenada 22860, México

Received 2015 June 19; revised 2016 April 11; accepted 2016 April 12; published 2016 September 2

ABSTRACT

We present our investigation of 319 Class II objects in Orion A observed by *Spitzer*/IRS. We also present the follow-up observations of 120 of these Class II objects in Orion A from the Infrared Telescope Facility/SpEx. We measure continuum spectral indices, equivalent widths, and integrated fluxes that pertain to disk structure and dust composition from IRS spectra of Class II objects in Orion A. We estimate mass accretion rates using hydrogen recombination lines in the SpEx spectra of our targets. Utilizing these properties, we compare the distributions of the disk and dust properties of Orion A disks with those of Taurus disks with respect to position within Orion A (Orion Nebular Cluster [ONC] and L1641) and with the subgroups by the inferred radial structures, such as transitional disks (TDs) versus radially continuous full disks (FDs). Our main findings are as follows. (1) Inner disks evolve faster than the outer disks. (2) The mass accretion rates of TDs and those of radially continuous FDs are statistically significantly displaced from each other. The median mass accretion rate of radially continuous disks in the ONC and L1641 is not very different from that in Taurus. (3) Less grain processing has occurred in the disks in the ONC compared to those in Taurus, based on analysis of the shape index of the 10 μm silicate feature ($F_{11.3}/F_{9.8}$). (4) The 20–31 μm continuum spectral index tracks the projected distance from the most luminous Trapezium star, θ^1 Ori C. A possible explanation is UV ablation of the outer parts of disks.

Key words: accretion, accretion disk – infrared: stars – protoplanetary disks – stars: pre-main sequence – surveys

Supporting material: extended figures, machine-readable tables

1. INTRODUCTION

In the process of star formation, young stars have circumstellar disks called “protoplanetary disks.” Protoplanetary disks evolve from optically thick flared disks toward optically thin, flat, tenuous disks, and these disks are known as the birthplaces of planets. The infrared-based classification of the spectral energy distributions (SEDs) of young stellar objects (YSOs) by Lada (1987) divides this evolution into three stages, Classes I, II, and III. These classifications are based on the spectral slope (α) of the infrared SEDs between near-infrared ($\sim 2 \mu\text{m}$) and mid-infrared ($\sim 25 \mu\text{m}$). Class I objects ($\alpha > 0$) have SEDs with increasing infrared emission dominated by the envelope, as expected from protostars. Class II objects ($-2 < \alpha < 0$) have relatively flat or negative SED slopes, corresponding to excess emission over infrared wavelength ranges produced by a dusty and optically thick disk around a pre-main-sequence (PMS) star. Class III objects ($\alpha < -2$) have SEDs with very little or no disk emission at infrared wavelengths, indicating that a disk is much evolved

and settled toward to the midplane with large-sized grains or has largely or completely dissipated.

Andre et al. (1993) extended the classification to an earlier Class 0 based on millimeter wavelength emission. Adams et al. (1988) modeled T Tauri stars with flat infrared spectra, and Greene et al. (1994) classified spectra with spectral indices between -0.3 and 0.3 as flat-spectrum (FS) sources since their spectral slopes are between Class I and II. The SED classes are closely, though not perfectly, matched to evolutionary stages (see Robitaille et al. 2006). Classes 0, I, and FS correspond to the progress of the accretion and dispersal of the protostellar envelope and the reduction of the central star’s average accretion rate through the range 10^{-4} to $10^{-7} M_{\odot} \text{yr}^{-1}$. In the Class II phase, the disk’s gaseous and small-grain components evolve and dissipate, while the central star’s accretion rate decreases from 10^{-7} to $10^{-10} M_{\odot} \text{yr}^{-1}$. Effects of orientation can make an object from one *evolutionary* stage appear to be in a different SED class; for example, a protoplanetary disk

without an envelope, viewed edge-on, may belong to the Class I SED type, as in the case of DG Tau B (Watson et al. 2004).

Throughout a disk’s life, its material is accreted toward the central star. A classification based on accretion indicators (for instance, $H\alpha$ equivalent width being greater/less than 10 \AA) divides T Tauri stars into classical T Tauri stars (CTTSs) and weak-lined T Tauri stars (WTTSs), which generally correspond closely to Class II and Class III, respectively.

The transitional disks (TDs) have the appearance of Class III YSOs at shorter infrared wavelengths and Class II YSOs at longer wavelengths (e.g., Espaillat et al. 2014). Therefore, TDs are young systems that have AU-scale radial gaps or central clearing in their dust distribution, while they still have optically thick and gas-rich outer disks. There are several mechanisms, such as photoevaporation, dust coagulation and grain growth, MRI instability, and giant planet formation, to explain the origin of gaps and holes in TDs. An interesting finding from the previous studies is that recent observations (e.g., Andrews et al. 2011; Olofsson et al. 2011; Casassus et al. 2013) of TDs and the statistical study of the properties of TDs (Kim et al. 2009, 2013) support the idea that giant planet formation produces the gaps of TDs. Kim et al. (2013) presented observationally and statistically significant trends in mass accretion rates (\dot{M}), showing that mass accretion rates of TDs are reduced by about one order of magnitude compared to the typical \dot{M} of CTTSs (Najita et al. 2007; Espaillat et al. 2012). This strongly suggests gap opening and disk clearing by newly formed planets in disks (Lubow & D’Angelo 2006).

The direction of evolution of protoplanetary disks does not proceed in one universal way. Some disks with weak mid-IR excess suggest that their disk material depleted in a global and homologous manner (e.g., Hernández et al. 2007; Currie et al. 2009). YSOs are also known to evolve along different tracks depending on their masses. A young star called a Herbig Ae/Be star has spectral type (SpT) of A or B, with masses between 2 and $10 M_{\odot}$. T Tauri stars have SpT between F and M, with masses less than $2 M_{\odot}$. The more massive Herbig Ae/Be stars and their disks evolve much faster than T Tauri stars. T Tauri stars will end up as stars similar to the Sun.

In this paper, we focus on Class II YSOs including TDs, associated with T Tauri stars, because the seeds of planets are thought to be formed in the dusty and massive disks present during this phase of evolution. Especially we will explore the characteristics of Class II YSOs in the Orion A star-forming region, and we will compare their properties with those of YSOs in other nearby star-forming regions, such as NGC 1333, Chamaleon I, and Taurus.

The entire Orion A molecular cloud appears to be a filament that is roughly perpendicular to the line of sight at a distance of 414 pc (Menten et al. 2007). Fits of stellar-evolution models to the color–magnitude diagrams of their member stars give ages of <1 Myr in the Orion Nebular Cluster (ONC; Hillenbrand 1997) and ~ 1 Myr for the southern part of Orion A LDN 1641 (L1641; Gálfalk & Olofsson 2008). YSO association age is a difficult subject. We will assume that the ages of the young clusters addressed in this paper lie in the range 0.5–5 Myr, and that the color–magnitude diagrams correctly rank the typical ages, with the ONC, L1641, and NGC 1333 being the youngest regions, Chamaleon I being the oldest, and the Taurus star-forming region being in between. Orion A differs from other nearby (≤ 500 pc) YSO associations studied with *Spitzer*, in that it is the only one that harbors an OB association. Yet it also

includes regions in the L1641 molecular cloud with stellar density and UV intensity as low as in the fiducial low-mass star formation region, Taurus.

To reveal the evolutionary characteristics of protoplanetary disks in Orion A, we use *Spitzer*-IRS observations of 319 protoplanetary disks in Orion A and follow-up observations of 120 objects with the Infrared Telescope Facility (IRTF)/SpeX. To explore the effects of environment on disk evolution and planet formation, we compare the structural and dust properties of Orion A disks to those of the much sparser Taurus association (Furlan et al. 2006, 2009, 2011).

This paper is organized as follows. In Section 2, we describe the observations and data reduction process. We report the basic stellar properties and disk properties derived from IRS spectra in Sections 3 and 4. Then, we compare the observed and derived stellar and disk properties of Orion A young members with those of Taurus members in Section 5. The main purpose of this paper is to make available measurements of the properties we measure from IRS spectra and conduct basic analysis to find how Orion A disks differ from disks in other regions. We will discuss many detailed correlations between properties as key clues of disk evolution in a forthcoming paper (K. H. Kim et al. 2016a, in preparation). In Section 6, we discuss how the evolution of protoplanetary disks is affected by the ultraviolet radiation field, by comparing disk properties by the distance from θ^1 Ori C, the most luminous O star in the ONC. Finally, we summarize our results in Section 7.

2. OBSERVATIONS AND DATA REDUCTION

We present 319 objects observed with *Spitzer*/IRS in the Orion A star-forming region in this paper. Some of the objects classified as TDs in Section 4.3.2 of this paper were presented in Kim et al. (2013). We described the *Spitzer*/IRS and IRTF/SpeX observations and data reduction process in Kim et al. (2013). Therefore, here we will describe our observations and data reduction process more briefly.

2.1. *Spitzer*/IRS

The Orion A objects in this paper were selected based on the identification of young stars with disks by IRAC/Two Micron All Sky Survey (2MASS) color–color diagrams (Megeath et al. 2012). We observed them using *Spitzer*/IRS during campaigns 36, 39, 40, and 44 between 2006 November and 2007 October. We include 303 Class II objects that we classified based on their *Spitzer* 4.5 to $22 \mu\text{m}$ spectral index. Of these, we observed 241 with full IRS wavelength coverage of 5– $37 \mu\text{m}$ (SL and LL modules). In addition, 62 objects located close to Trapezium region were observed with partial wavelength coverage (5– $14 \mu\text{m}$; SL only) because the detectors for the longer wavelengths would have been saturated by bright background emission. To this group we added 16 additional objects (5 in the ONC; 11 in L1641) that were reclassified as Class II from Class 0/I sources observed in the Orion A protostar survey by C. Poteet et al. (2016, in preparation); 14 of these 16 were observed during campaigns 39 and 40, but 2 sources were observed in campaign 56. This gives us a total of 319 sources, with 62 near the Trapezium, 132 in the ONC, and 125 in L1641 in this paper. Table 1 gives the IRS observation log, including coordinates, observation date, observing mode, AOR ID, and campaign numbers. The positions of these IRS targets in the

Table 1
Observation and Reduction Log of IRS Spectra

Num. (1)	IRS Name (2)	R.A. (J2000) (3)	Decl. (J2000) (4)	AORID (5)	IRS Camp. (6)	Date Observed (7)	Modules (8)	Region (9)	Reduction (10)
1	8336884-5290	5 33 28.52	-5 17 26.16	18804224	39	2007 Mar 12	SLLL	ONC	AdOpt
2	8339347-5238	5 33 34.43	-5 14 17.70	18843904	39	2007 Mar 12	SLLL	ONC	AdOpt
3	8343858-5513	5 33 45.26	-5 30 49.75	18825472	39	2007 Mar 12	SLLL	ONC	AdOpt
4	8343917-6073	5 33 45.40	-6 04 25.86	18848000	39	2007 Mar 09	SLLL	L1641	man
5	8343944-5609	5 33 45.47	-5 36 32.54	18833152	39	2007 Mar 12	SLLL	ONC	opse/AdOpt ^a

Notes. Column (1): numbers in this column are from the number sequence of 303 Class II objects observed in the IRS program ID 30706 and the additional 16 Class II candidates identified from the *Herschel* Orion Protostar Survey. We use these numbers to identify objects conveniently. This number sequence will be used consistently in other future papers dealing with the objects in this work. Column (2): IRS names indicated here are used to identify objects often in other works. The IRS names come from the position of each object. Column (10): the methods of source extraction to get the SEDs in Figures 7 and 8. ECO: an automated tapered column extraction in SMART with off-nod or off-order sky subtraction; man: a manual tapered column extraction in SMART with a constant or linear sky subtraction; AdOpt: an optimal source extraction using an empirical point-response function (PRF) in SMART; opse: an optimal source extraction using an analytical PRF.

^a SL & LL1: opse; LL2: AdOpt.

^b SL: man; LL: AdOpt.

^c SL: AdOpt; LL:opse.

^d SL & LL1: AdOpt; LL2: man.

^e SL & LL2: man; LL1: opse.

^f SL: opse; LL: AdOpt.

^g SL & LL2: AdOpt; LL1: opse.

^h SL & LL2: AdOpt; LL1: ECO.

ⁱ SL: AdOpt; LL: ECO.

^j SL: opse; LL2: AdOpt; LL1: man.

^k SL: opse; LL: man.

^l SL & LL2: AdOpt; LL1:man.

^m SL2: AdOpt; SL1: man.

ⁿ The IRS program ID 30859.

^o The IRS program ID 50374.

(This table is available in its entirety in machine-readable form.)

ONC, L1641, and the Trapezium are indicated in Figures 1–3, respectively.

We began with version S15.3 of the basic calibrated data product from the Spitzer Science Center IRS pipeline for both SL and LL. As described in detail by Kim et al. (2013), we first fix bad, hot, and rogue detector-array pixels before extracting objects from the 2D spectral images. Since the spectral extraction of Orion objects needs very careful background subtraction due to the complex and strong sky emission varying spatially and the high stellar density, we used four different source extraction methods to optimize the rejection of emission from background sky and nearby sources. The first method is to extract the spectral source using an automated extractor (“auto”) with two versions of sky subtractions: sky subtraction of the two nods (“off-nod”) and sky subtraction of the sky spectrum in each grating order obtained while the target was being observed in the other order (“off-order”). If the sky-subtracted 2D images and the reduced spectra have artifacts attributable to sky subtraction and/or contamination from nearby sources, we re-extract the source by removing the sky with zeroth- or first-order polynomial fitting to the background emission on either side of the target. We call this method “man” because we selected the sky manually. In both “auto” and “man,” we extracted sources from the uniformly weighted signal along a tapered column, 3–5 pixels wide using the Spectral Modeling, Analysis, and Reduction Tool (SMART; Higdon et al. 2004).

The other two methods are to reduce spectra from optimal point-source extraction. One is the AdOpt routine in SMART (Lebouteiller et al. 2010). It uses an empirical point-response function (PRF) and can fit multiple objects along the slit. The

other script is OPSE, developed separately from SMART (C. Tayrien & W. J. Forrest 2016, in preparation). OPSE uses an analytical PRF and accounts for pointing errors along the slit. The sky is modeled as a linear function of distance in the 5–9 pixel long extraction window.

We calibrated the flux of spectra by multiplication with relative spectral response functions, which were generated by dividing a template of a calibration star’s intrinsic spectrum by the calibrator’s spectrum obtained from its raw spectral extraction, extracted in the same way as the target spectrum. Our photometric standards were α Lac (A1V; M. Cohen 2003, private communication) for SL, ξ Dra (K2III; M. Cohen 2003, private communication) for the part of LL at wavelength less than 32 μ m, and Mrk 231 (J. Marshall 2007, private communication) for LL beyond 32 μ m.

After comparing the spectra reduced from the different source extraction methods for each object, we selected the final spectrum with the fewest artifacts. To obtain such a spectrum, we combined spectra extracted in different ways to create the spectrum adopted here, if necessary. For example, we use the combined spectrum for OriA-19, which is mixed and matched with SL1 and SL2 from AdOpt and LL1 and LL2 from OPSE. We list the reduction choices for the final selection of spectra in Table 1.

Not all of our sources have been cited in the literature. We list some selected identifications of the targets in Table 2. In many cases, objects are primarily identified by their coordinates, and it is convenient to name the object according to its coordinates. However, to discuss the sources more easily, we cite the ID number given in Table 1 throughout this paper (e.g., OriA-123, or 123 if the list of objects is long).

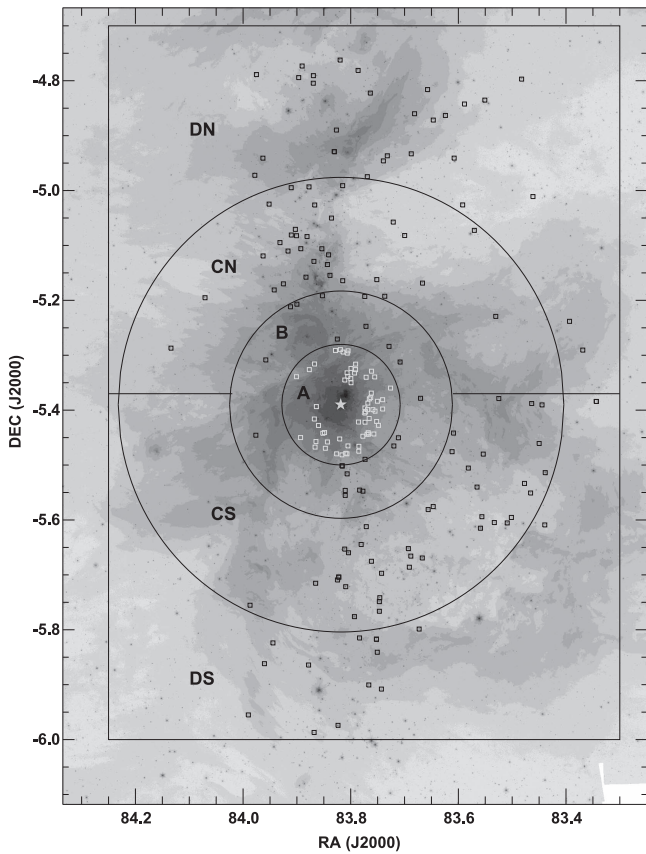


Figure 1. IRS targets in the ONC plotted over the IRAC/*Spitzer* ch2 ($4.5 \mu\text{m}$) image. The squares indicate the Class II objects observed with IRS. The black squares are for objects observed in the SLLL mode only. The gray squares are for objects observed in the SL mode only. Subsections of the ONC separated by the projected distance (d) from θ^1 Ori C (yellow star) are indicated. The criteria of the subsections are as follows: A: $d \leq 0.7$ pc; B: $0.7 \text{ pc} < d \leq 1.5$ pc; C: $1.5 \text{ pc} < d \leq 2.5$ pc; D: $d > 2.5$ pc and $\text{DEC} > -6^\circ$. Subsections B, C, and D are also separated by N and S from the DEC of θ^1 Ori C.

2.2. IRTF/*SpeX*

Of our 257 IRS targets observed in both SL and LL modules in Orion A with *Spitzer*/IRS, we observed 120 at near-IR ($0.8\text{--}2.4 \mu\text{m}$) wavelengths with the medium-resolution spectrograph *SpeX* (Rayner et al. 2003), on the NASA IRTF on Mauna Kea during the 2010A, 2011A, and 2011B semesters.

We observed all of the *SpeX* targets with the Short-wavelength Cross-Dispersed mode (SXD). We obtained spectra with various slit widths of $0''.3$, $0''.5$, and $0''.8$ for observations depending on the seeing conditions of each night. We used only the $0''.8$ slit width for the observations of 2011 February because the weather and seeing were generally poor.

During the *SpeX* observations, we discovered that some of the IRS targets are multiple systems. Among the *SpeX* targets with close companions, the companions of four objects, OriA-38, OriA-173, OriA-208, and OriA-290, were observed separately from the primary targets. For targets with very close neighbors, OriA-4, OriA-26, OriA-47, OriA-98, and OriA-280, we oriented the slit so as to observe both simultaneously and extracted the spectra of primary and secondary separately during the data reduction process. We also found that OriA-22, OriA-125, OriA-154, OriA-213, and OriA-233 were potential binary systems because they appeared

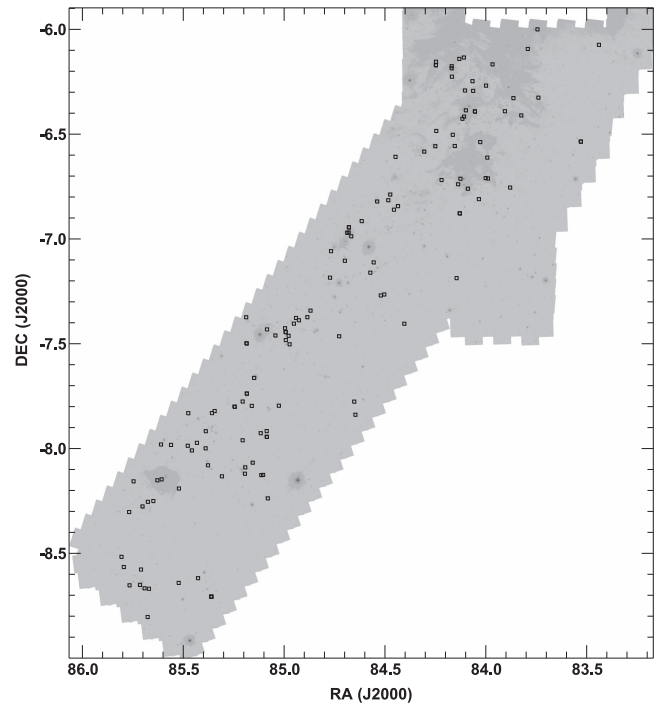


Figure 2. IRS targets in L1641 plotted over the IRAC/*Spitzer* ch2 ($4.5 \mu\text{m}$) image. The squares indicate the Class II objects observed with IRS.

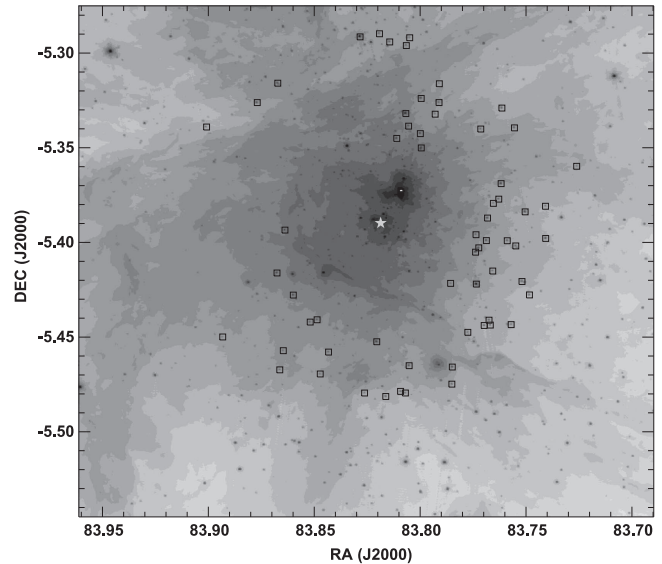


Figure 3. Close-up of subsection A (Trapezium region) in Figure 1. θ^1 Ori C is indicated with a star.

elongated and peanut shaped in the K -band guider images. The components of these systems were not clearly resolved, so we present their *SpeX* spectra as a combined spectrum from both the primary and secondary of the binary. Among those close and/or suspicious binaries observed with *SpeX*, OriA-26 is the only one identified as a spectroscopic binary (SB) based on radial velocity measurement by Tobin et al. (2009, 2013).

We observed an A0V star, HD 37887, every 30–60 minutes for flux calibration and telluric absorption correction (Vacca et al. 2003). To allow for changing the slit orientation to avoid including nearby sources, we also observed the calibrator source with the same slit position angle as the target's slit

Table 2
Identifications of the Objects

Num.	IRS Name	2MASS Name	Other Names Selected
1	8336884-5290	05332852-0517262	V719 Ori, [FHM2008] F22-ap40, Parenago 1190
2	8339347-5238	05333443-0514177	[FHM2008] S1-ap78
3	8343858-5513	05334525-0530498	VZ Ori, [FHM2008] S3-ap68, HBC 106, Parenago 1260
4	8343917-6073	05334537-0604253	V1006 Ori, HBC 108, Parenago 1267
5	8343944-5609	05334545-0536323	V726 Ori, [FHM2008] S1-ap42

Notes. The sources of selected object names: Parenago (1954) for Parenago XXX; Fűrész et al. (2008) for [FHM2008]XXX-XXXX; V* indicates the General Catalog of Variable Stars (GCVS; Kukarkin et al. 1971); HBC XXX indicates the Herbig+Bell Catalog (Herbig & Bell 1988, p. 3); HOPS-XXX indicates the identification of these sources in the *Herschel* Orion Protostar Survey (HOPS; Megeath et al. 2010).

^a The coordinate of HBC 497 (DL Ori/G3) does not exactly match the IRS coordinate of OriA-270.

^b A 2MASS source is 2–3'' away from the target.

^c *JHK* photometry is from Robberto et al. (2010).

(This table is available in its entirety in machine-readable form.)

position angle. The IRTF/SpeX observation log is given in Table 3. We reduced our spectra with the Spextool package (Cushing et al. 2004), and flux calibration and telluric absorption correction (Vacca et al. 2003) were done with a spectrum of HD 37887, observed near in time and airmass to each object. In a few exceptional cases, we used a telluric calibration spectrum taken later in time and made a light loss correction to correct a target spectrum for slit losses relative to the flux calibrator, HD 37887.

2.3. Ancillary Photometry

We compiled broadband photometry to construct SEDs in addition to IRS and SpeX spectra. We gathered optical photometry from the Naval Observatory Merged Astrometric Dataset (NOMAD; Zacharias et al. 2005), with *B*, *V*, and *R* bands at 0.44, 0.55, and 0.64 μm , respectively. For ONC sources, we acquired additional data from da Rio et al. (2010) at *U*, *B*, *V*, *TiO*, and *I* bands centered at 0.347, 0.454, 0.538, 0.6217, and 0.862 μm , respectively. More optical and near-IR photometry was added from the Sloan Digital Sky Survey (SDSS) photometric catalog (release 8; Aihara et al. 2011) at *u*, *g*, *r*, *i*, and *z* bands centered on 0.31, 0.48, 0.62, 0.76, and 0.91 μm , respectively. We also take *I*, *J*, and *K* bands at 0.8, 1.25, and 2.16 μm , respectively, from the DENIS database (DENIS Consortium 2005). We collected 2MASS *J* (1.25 μm), *H* (1.65 μm), and *K_s* (2.17 μm) magnitudes from the 2MASS catalog (Skrutskie et al. 2006). Most of our targets (except OriA-146, OriA-158, OriA-302, and OriA-306) have 2MASS photometry. We adopt *J*, *H*, and *K* magnitudes from Prisinzano et al. (2008) for OriA-306. Additionally, photometry at bands *Z* (0.88 μm), *Y* (1.03 μm), *J* (1.25 μm), *H* (1.63 μm), and *K* (2.20 μm) from the UKIRT Infrared Deep Sky Survey (UKIDSS DR8; UKIDSS Consortium 2012) were collected. IRAC (3.6, 4.5, 5.8, and 8.0 μm) and MIPS (24 μm) photometry of our sources had been acquired prior to the IRS observations (Megeath et al. 2012), and we included them. We also include near- to mid-IR observations at 3.4, 4.6, 12, and 22 μm from the *Wide-field Infrared Survey Explorer* (*WISE*) all-sky data release (Cutri et al. 2012). It is recommended to use *WISE* photometry with caution due to the source extraction methods used in the pipeline (e.g., Koenig & Leisawitz 2014). We include *WISE* photometry only if a corresponding observation has an “ex” tag value of zero, i.e., not an extended source, to avoid including neighboring objects because *WISE* has relatively coarse resolution. We find that these criteria

Table 3
Observation Log of SpeX Spectra

Num.	Obs. Date	Slit Width	Total Int. Time	PA	Note
(1)	(UT)	(arcsec)	(s)	(deg)	(6)
(1)	(2)	(3)	(4)	(5)	(6)
1	2011 Nov 06	0.5	480
2	2011 Feb 28	0.8	480	−10.73	...
3	2011 Nov 07	0.8	120
4	2011 Feb 28	0.8	320	−30	b
5	2011 Feb 28	0.8	400	−10.73	...

Note. Column (1): the numbers are assigned in Table 1. When an object was revealed to have a nearby companion and it was observed separately from the target object with SpeX, we add “a” and “b” next to the number. Column (5): the slit’s positional angle for observation of a target. Column (6): note for observation of binary systems: “a” indicates the system for which its primary and secondary were observed separately; “b” indicates the system for which its primary and secondary were observed simultaneously and extracted their spectra separately; “c” indicates the system that is suspected to have a secondary, but the spectrum of each component was not resolved, and the spectrum is the composite spectrum of a primary and a secondary.

(This table is available in its entirety in machine-readable form.)

eliminate *WISE* data, which show a spurious jump compared to IRAC and MIPS photometry in their SEDs.

In case there are multiple (mostly two or three) sets of UKIDSS and SDSS data with different designations for an object within a distance of 3 arcsec from our target position, we include the combined photometric points of multiple sets for the corresponding SEDs, as we cannot ignore the possibility of multiple systems. Tobin et al. (2009, 2013) identified 89 SBs in the ONC with high/moderate confidence. Among those 89 SBs, 13 objects match with our objects in the ONC. The corresponding objects are OriA-5, 26, 37, 45, 60, 88, 91, 111, 142, 148, 180, 189, and 205. Five of them are double-line binaries (OriA-37, 45, 60, 91, and 111), and the remaining sources are single-lined binaries. We have checked whether 13 SBs have multiple UKIDSS and/or SDSS photometry. OriA-26 is the only object with multiple sets by both SDSS and UKIDSS. OriA-37 and OriA-60 have multiple sets of UKIDSS. However, we do not discuss multiplicity further here. A comprehensive discussion of the multiplicity of these objects awaits higher spatial and spectral resolution observations.

Table 4
Spectral Type and Extinction

Num.	IRS Name	Spectral Types	Spectral Type	EW(H_{α})	EW(Li)	A_V	A_V Method
(1)	(2)	(3)	Adopted(4)	(5)	(6)	(7)	(8)
1	8336884-5290	M0.0(8)	M0.0	-22.5	0.5	$0.77^{+1.02}_{-0.39}$	J-H
2	8339347-5238	M3.0(8)	M3.0	-12.5	0.4	$1.15^{+0.52}_{-1.07}$	J-H
3	8343858-5513	K1(3)	K1.0	$4.37^{+2.50}_{-3.05}$	J-H
4	8343917-6073	M1.5(1); M1.0(23)	M1.0	-101.0	0.2	$0.09^{+2.70}_{-0.00}$	CTTS J-H
5	8343944-5609	M5.5(3); M5.5(8)	M5.5	-33.3	0.3	$0.50^{+1.24}_{-0.29}$	I-J
6	8344455-5390	$3.21^{+9.26}_{-1.79}$	CTTS J-H
7	8344987-5460	M6(3)	M6.0	$2.42^{+1.07}_{-1.09}$	J-H
8	8346141-5010	M2(3); M3.5(8)	M3.5	-8.6	0.3	$0.23^{+1.47}_{-0.00}$	I-J
9	8346378-5387	$9.88^{+5.75}_{-4.85}$	CTTS J-H
10	8346581-5550	$10.10^{+7.48}_{-0.00}$	CTTS J-H
11	8347711-5533	K7.0(SpeX)	K7.0	$8.28^{+3.70}_{-3.63}$	J-H
12	8348250-4797	$1.69^{+7.48}_{-0.59}$	CTTS J-H
13	8350150-5595	M3.5(3)	M3.5	$0.00^{+2.49}_{-0.00}$	I-J
14	8350916-5605	K7.5(8); K7(11)	K7.5	-5.5	0.4	$1.63^{+1.00}_{-0.00}$	I-J
15	8352483-5378	K7.5(8)	K7.5	-28.3	0.5	$5.26^{+3.10}_{-2.30}$	CTTS J-H
16	8353051-5229	K1.0(SpeX)	K1.0	$2.66^{+1.18}_{-2.39}$	J-H
17	8353319-5604	M4.0(8); M3.5(9)	M4.0	-116.2	0.2	$1.16^{+2.67}_{-1.16}$	J-H
18	8355083-4835	$1.00^{+7.67}_{-0.00}$	CTTS J-H
19	8355371-5480	K7.0(H)(2)	K7.0	$0.00^{+1.84}_{-0.00}$	I-J
20	8355629-5594	M1.9(9)	M2.0	$3.46^{+4.70}_{-1.21}$	CTTS J-H
21	8355898-5615	F6(5); F7.0(8); F8(12)	F7.0	$0.17^{+3.29}_{-0.17}$	I-J
22	8356531-5540	M2.0(8); K8e(3)	M2.0	-52.9	0.3	$1.17^{+5.90}_{-0.00}$	I-J
23	8357031-5072	K7(3); M0.0(8)	M0.0	-3.8	0.5	$1.49^{+1.22}_{-0.63}$	J-H
24	8358147-5505	K5(H)(2); K1e(3)	K1.0	$3.86^{+2.79}_{-2.66}$	J-H
25	8358862-4842	M3.0(7); M3.5(8)	M3.5	-15.0	0.4	$1.22^{+0.54}_{-0.45}$	J-H
26	8359203-5026	M5.5(8)	M5.5	-16.7	0.3	$0.00^{+0.49}_{-0.00}$	I-J
27	8360781-4940	M0.5(8)	M0.5	-81.1	0.2	$0.39^{+2.46}_{-0.00}$	I-J
28	8360900-5441	K2-K3e(2); K7.5(8); K2.5e(11)	K7.5	48.6	0.0	$2.96^{+5.55}_{-1.28}$	CTTS J-H
29	8361167-5475	M0.0(SpeX)	M0.0	$0.50^{+3.01}_{-0.50}$	I-J
30	8362406-4863	M0.5(8); K7(11)	M0.5	-36.2	0.4	$6.28^{+2.81}_{-3.45}$	J-H
31	8364658-4871	$4.94^{+6.75}_{-3.47}$	CTTS J-H
32	8364671-5575	M4(2); M5.0(8)	M5.0	-101.0	0.2	$0.20^{+3.17}_{-0.00}$	I-J
33	8365614-5581	K2-K5e(2); M5.0(8); K3.5(11)	M5.0	$0.00^{+5.30}_{-0.00}$	I-J
34	8365722-4816	M1.0(SpeX)	M1.0	$1.20^{+3.39}_{-0.38}$	I-J
35	8366668-5168	B8, A0(2); B8(5); A0(11)	A0.0	$1.14^{+2.17}_{-1.14}$	I-J
36	8366704-5669	K2(5); K0e(11)	K2.0	$0.56^{+3.94}_{-0.19}$	I-J
37	8367030-5378	K1e, G-Ke, K7.3(2); K7(5); G:e(11)	K7.0	$3.31^{+5.63}_{-2.47}$	J-H
38	8367284-5798	M0(3)	M0.0	$0.86^{+1.64}_{-0.86}$	I-J
39	8368137-4860	M3.5(8)	M3.5	-18.8	0.5	$0.54^{+1.19}_{-0.33}$	I-J
40	8368755-4933	K0(3)	K0.0	$7.20^{+4.87}_{-1.39}$	CTTS J-H
41	8368837-5665	$2.78^{+9.86}_{-0.71}$	CTTS H-K
42	8369106-5686	M3.5(3); M4.0(8); M3.0e(9)	M4.0	-19.5	0.4	$0.93^{+2.59}_{-0.55}$	I-J
43	8369290-5652	$2.88^{+2.35}_{-1.99}$	CTTS J-H
44	8369980-5081	K7(3); M1.0(8)	M1.0	-40.0	0.5	$0.40^{+2.93}_{-0.00}$	I-J
45	8370827-5312	A3, A2, A2Vp, A5V, A6-7V, Am(2); A3, A2(5); A7.0(8)	A7.0	$1.51^{+7.23}_{-1.51}$	I-J
46	8371143-5450	M0e(2); K7.5(8); M0(11)	K7.5	-44.1	0.5	$2.01^{+2.45}_{-1.31}$	CTTS J-H
47	8371984-5465	K7.5(8)	K7.5	-7.8	0.6	$4.44^{+0.00}_{-4.44}$	H-K
48	8372100-5057	K5(2); M0.0(8); G:e(11)	M0.0	$0.34^{+2.20}_{-0.00}$	I-J
49	8372608-5359	M2(2)	M2.0	$0.09^{+1.11}_{-0.09}$	I-J
50	8372885-5283	K4-K6e(2); K6.5(8); K4.7:e(14)	K6.5	-36.1	0.6	$4.65^{+4.29}_{-2.46}$	CTTS J-H
51	8373201-4936	M3.0(8)	M3.0	-5.0	0.5	$6.52^{+2.92}_{-3.63}$	J-H
52	8373676-5192	K5, K6(2); K5(11)	K5.0	$0.00^{+0.24}_{-0.00}$	I-J
53	8373930-6325	M3.5(1); M3.5(23)	M3.5	-9.8	0.4	$0.13^{+2.62}_{-0.13}$	I-J
54	8373936-4946	$11.00^{+3.76}_{-6.17}$	CTTS J-H
55	8374073-5397	K8(2)	K7.5	$0.93^{+0.82}_{-0.38}$	J-H
56	8374080-5380	M3(2); M3.5(8)	M3.5	-39.7	0.3	$0.69^{+1.17}_{-0.00}$	I-J
57	8374271-5697	$5.67^{+3.16}_{-3.26}$	CTTS J-H

Table 4
(Continued)

Num. (1)	IRS Name (2)	Spectral Types (3)	Spectral Type Adopted(4)	EW($H\alpha$) (5)	EW(Li) (6)	A_V (7)	A_V Method (8)
58	8374301-5908	M0.0(8)	M0.0	-46.1	0.1	$0.48^{+5.07}_{-0.36}$	CTTS J-H
59	8374388-6000	K5(3); M2.5(8); M0.1(23)	M0.0	-77.7	0.4	$0.08^{+1.40}_{-0.08}$	J-H
60	8374599-5741	$0.00^{+2.45}_{-0.00}$	CTTS J-H
61	8374677-5748	$6.58^{+5.66}_{-2.77}$	CTTS J-H
62	8374677-5766	$4.67^{+4.11}_{-1.73}$	CTTS J-H
63	8374839-5427	M2(2); M0.5(8)	M0.5	-13.6	0.5	$1.26^{+0.80}_{-0.68}$	J-H
64	8375041-5383	K0-K2e, K0e, K6(2)	K0.0	$3.03^{+1.35}_{-1.96}$	J-H
65	8375063-5840	$7.03^{+2.35}_{-2.95}$	CTTS J-H
66	8375158-5162	M5.5(2); M5.0(8)	M5.0	-10.3	0.4	$0.13^{+0.34}_{-0.13}$	I-J
67	8375190-5420	K6e(2); K7.5(8)	K7.5	-23.3	0.6	$0.85^{+7.05}_{-0.02}$	CTTS H-K
68	8375484-5401	$0.00^{+2.04}_{-0.00}$	CTTS J-H
70	8375702-5443	$2.51^{+6.62}_{-0.73}$	CTTS J-H
71	8375886-5399	$14.00^{+7.40}_{-2.04}$	CTTS J-H
73	8376154-5675	$15.00^{+5.07}_{-5.97}$	CTTS J-H
74	8376176-5368	G:(H)(2)	G0.0	$8.28^{+9.07}_{-2.53}$	CTTS H-K
75	8376287-5377	M6(2)	M6.0	$0.85^{+3.58}_{-0.06}$	I-J
76	8376356-4822	$1.00^{+3.80}_{-0.55}$	CTTS J-H
77	8376541-5379	M5.5e (2)	M5.5	$3.93^{+5.13}_{-1.21}$	H-K
78	8376571-5415	M4.3(9)	M4.5	$5.23^{+4.20}_{-5.23}$	J-H
79	8376643-5900	$6.09^{+5.22}_{-1.54}$	CTTS J-H
80	8376687-5443	M2(2); M1.0(8)	M1.0	-19.3	0.5	$1.65^{+1.73}_{-1.04}$	J-H
81	8376747-5441	M2e(2)	M2.0	$2.82^{+1.26}_{-2.03}$	J-H
82	8376817-5387	M0.5-M2e, M1.2, M3, K4-M0(2)	M3.0	$0.95^{+2.01}_{-0.00}$	I-J
83	8376871-5399	K2, M0, M4(2); G8.5(8)	G8.5	-19.9	0.5	$3.66^{+4.91}_{-1.15}$	CTTS J-H
84	8376918-4974	M0.0(8)	M0.0	-26.9	0.3	$4.53^{+5.87}_{-2.02}$	CTTS J-H
85	8376976-5443	M0.5(2); K7.5(8)	K7.5	-15.2	0.5	$2.22^{+1.00}_{-0.97}$	J-H
86	8377111-5612	M4.5(2); M4.5(8)	M4.5	-16.4	0.2	$0.54^{+2.60}_{-0.00}$	CTTS J-H
88	8377167-5247	F8, G (2); F8, G2(5); G0+F7 (15)	G5.0	$2.39^{+1.07}_{-2.39}$	J-H
89	8377232-5402	M0(2); K7.0(8)	K7.0	-88.1	0.2	$5.11^{+3.40}_{-2.70}$	J-H
90	8377335-5489	M0.5(2)	M0.5	$5.77^{+5.69}_{-3.39}$	CTTS J-H
91	8377345-5422	K0, K0-K3e, A0V+K1V, A0V, K4eIV, K3 (2); K0, K2(5)	K0.0	$3.65^{+3.65}_{-3.49}$	J-H
92	8377361-5395	<M0e(2)	M0.0	$7.54^{+5.50}_{-1.79}$	J-H
93	8377383-5405	K2-K7e(2); K6.5(8)	K6.5	-237.6	0.2	$2.47^{+6.79}_{-1.31}$	CTTS J-H
94	8377392-5193	M2.5(8)	M2.5	-27.2	0.0	$6.27^{+4.04}_{-2.87}$	H-K
95	8377737-5547	$4.88^{+8.94}_{-0.00}$	CTTS J-H
96	8377749-5447	M4.5e(2)	M4.5	$0.43^{+3.27}_{-0.43}$	CTTS J-H
97	8378059-5644	$8.57^{+3.10}_{-3.00}$	CTTS J-H
98	8378345-5545	K7.0(8); M0(11)	K7.0	-37.6	0.5	$1.02^{+4.32}_{-0.49}$	CTTS J-H
99	8378366-5814	$4.46^{+4.79}_{-2.41}$	CTTS J-H
100	8378481-5465	$5.59^{+3.24}_{-3.02}$	CTTS J-H
101	8378503-5474	K2(2)	K2.0	$5.93^{+5.71}_{-3.56}$	CTTS J-H
102	8378561-5421	M2(2)	M2.0	$0.56^{+3.63}_{-0.00}$	I-J
103	8378630-4781	$5.97^{+6.78}_{-3.94}$	CTTS J-H
106	8379192-6093	$10.80^{+5.92}_{-5.40}$	CTTS J-H
108	8379312-5776	K4(13), K0.0(7); Ke(16)	K0.0	$3.91^{+2.68}_{-2.89}$	J-H
112	8380422-5659	K3(5)	K3.0	$1.15^{+3.86}_{-0.00}$	CTTS J-H
114	8380518-5465	M2.0(11)	M2.0	$5.59^{+3.60}_{-2.49}$	H-K
117	8380667-5516	K5e, F8-G0III-IV(2); G7:e(11)	G7.0	$1.41^{+5.51}_{-0.46}$	I-J
119	8380695-5479	M2.8(9)	M3.0	$3.23^{+1.93}_{-1.41}$	H-K
120	8380923-5478	$7.12^{+6.65}_{-2.20}$	H-K
121	8380932-5721	$1.06^{+3.15}_{-0.00}$	CTTS J-H
122	8381019-5555	K5, K4-M0(2)	K5.0	$9.53^{+5.69}_{-5.78}$	J-H
123	8381020-5546	M4(11)	M4.0	$1.63^{+6.01}_{-0.00}$	I-J
125	8381120-5653	K0-K3(P)(2)	K1.5	$1.88^{+6.34}_{-0.00}$	CTTS J-H
127	8381491-5164	$5.99^{+2.20}_{-2.00}$	CTTS J-H
128	8381501-4991	$12.40^{+4.86}_{-3.96}$	CTTS J-H
129	8381622-5481	M2.5(11)	M2.5	$1.04^{+3.10}_{-0.00}$	I-J

Table 4
(Continued)

Num. (1)	IRS Name (2)	Spectral Types (3)	Spectral Type Adopted(4)	EW($H\alpha$) (5)	EW(Li) (6)	A_V (7)	A_V Method (8)
131	8381971-4762	K1e(13)	K1.0	$1.11^{+5.81}_{-0.00}$	I-J
132	8382048-5452	$13.60^{+6.48}_{-7.76}$	CTTS J-H
133	8382359-5974	$1.31^{+2.97}_{-0.92}$	CTTS J-H
134	8382412-6410	M0.5(1); M2(4); M1(10); M0.5(23)	M0.5	-12.1	0.6	$0.87^{+1.06}_{-0.56}$	J-H
135	8382467-5709	K3(5)	K3.0	$1.48^{+4.48}_{-1.48}$	H-K
136	8382490-5270	K7+M1.5(15)	K7.0	$8.48^{+3.79}_{-2.99}$	J-H
137	8382623-5479	M2.5(9)	M2.5	$1.74^{+0.78}_{-0.97}$	J-H
138	8382655-4889	$6.58^{+4.75}_{-3.45}$	CTTS J-H
139	8382835-5291	A8-F0(2)	A9.0	-2.2	0.0	$14.10^{+6.35}_{-7.92}$	J-H
140	8383581-5050	$26.50^{+4.65}_{-8.04}$	CTTS H-K
141	8383861-5154	G1, G0, F9IV, K2Ve, F8-G0III-IV, G0III (2); G1, G0(5); F8.0(8)	F8.0	$0.76^{+5.83}_{-0.76}$	I-J
142	8384113-5117	$2.40^{+3.80}_{-1.84}$	CTTS J-H
143	8384325-5457	M4.5e (2); M5.0(8)	M5.0	-119.3	0.3	$2.04^{+3.46}_{-1.07}$	CTTS J-H
144	8384331-5134	K7.0(8)	K7.0	-28.5	0.6	$5.44^{+5.21}_{-2.67}$	CTTS J-H
145	8384717-5469	M3.5(2)	M3.5	$2.83^{+1.82}_{-0.92}$	CTTS J-H
146	8384864-5440	M3.0(11)	M3.0	$1.39^{+0.00}_{-0.00}$	I-J
147	8385190-5442	M4-M4.5e, M5.3, M4(2)	M4.5	$2.35^{+2.66}_{-1.48}$	CTTS J-H
148	8385255-5191	K6e(2); K7.5(8)	K7.5	-76.2	0.2	$4.79^{+2.14}_{-2.10}$	J-H
149	8385365-5106	$21.30^{+9.91}_{-4.98}$	CTTS J-H
150	8385988-5427	G5, G0III, G-K, K1, M3(2)	G5.0	$1.91^{+1.58}_{-1.91}$	J-H
151	8386322-6328	M2.0(1); M2.5(4); M1.5(10); M2.1(23)	M2.0	-6.5	0.4	$1.03^{+0.64}_{-0.63}$	J-H
152	8386383-5393	K4(2)	K4.0	$3.76^{+2.51}_{-2.09}$	CTTS J-H
153	8386462-5457	M3, M3.2(2); M2.0(8)	M2.0	-2.0	0.5	$0.87^{+2.45}_{-0.27}$	H-K
154	8386523-5715	M3.6(9)	M3.5	$1.87^{+2.43}_{-0.00}$	J-H
155	8386627-5467	M5(2)	M5.0	$0.18^{+2.28}_{-0.00}$	I-J
156	8386694-5026	$28.60^{+4.63}_{-17.99}$	CTTS H-K
158	8386759-5416	K7.0(11)	K7.0	$1.25^{+0.00}_{-0.00}$	I-J
159	8386804-5987	M3.5(8)	M3.5	-30.8	0.3	$0.00^{+2.19}_{-0.00}$	I-J
160	8386841-5129	$19.90^{+4.66}_{-5.09}$	CTTS H-K
161	8386935-4790	K1(3); M4.5(8)	M4.5	-108.2	0.4	$0.15^{+2.93}_{-0.00}$	I-J
162	8386957-4804	$17.70^{+0.05}_{-17.70}$	H-K
163	8387691-5326	$11.00^{+6.16}_{-1.12}$	CTTS J-H
164	8387753-4993	$14.70^{+7.23}_{-2.89}$	CTTS J-H
165	8387832-5864	$4.97^{+1.88}_{-2.23}$	CTTS J-H
166	8387937-6755	M3(4); M3(10); M2.9(23)	M3.0	-95.0	0.3	$0.03^{+1.01}_{-0.00}$	I-J
167	8388119-5083	M2.0(8)	M2.0	-143.1	0.2	$0.40^{+3.14}_{-0.00}$	I-J
168	8388316-5157	K3, K6, K4-M0eIV(2); K4(5); M0.5+M1.5(15)	M1.0	$0.21^{+2.52}_{-0.00}$	I-J
169	8389033-4773	K4(3); M0.5(8)	M0.5	-66.5	0.4	$1.67^{+1.18}_{-1.50}$	J-H
170	8389275-5105	A0(5)	A0.0	$0.00^{+0.16}_{-0.00}$	J-H
172	8389673-4794	M1.0(7); M3.0(8)	M3.0	$1.25^{+1.27}_{-1.09}$	J-H
173	8390003-5207	G6-K2e (2)	K0.0	-6.2	0.5	$1.56^{+10.02}_{-0.00}$	I-J
174	8390073-5082	$8.42^{+2.16}_{-5.24}$	CTTS J-H
175	8390083-5339	$8.39^{+4.34}_{-1.23}$	CTTS J-H
176	8390285-5070	M1.5(8)	M1.5	-32.1	0.5	$0.44^{+3.05}_{-0.44}$	I-J
177	8390554-6390	M2.5(1); M2.4(23)	M2.5	-53.8	...	$0.21^{+0.20}_{-0.21}$	I-J
178	8391040-5081	$16.90^{+7.45}_{-4.46}$	CTTS J-H
179	8391058-4994	M0.0(8)	M0.0	-43.6	0.3	$2.92^{+2.72}_{-0.67}$	J-H
180	8391196-5211	K2 (2); K5.0(8)	K5.0	-5.2	0.5	$4.06^{+2.77}_{-2.17}$	CTTS J-H
181	8391648-5110	$5.47^{+2.05}_{-2.12}$	CTTS J-H
182	8392509-5169	K6-K8 (2); K6.5(8)	K6.5	-8.1	0.2	$6.39^{+2.86}_{-3.11}$	J-H
183	8393152-5094	M0.0(8)	M0.0	-27.9	0.3	$2.23^{+5.05}_{-1.68}$	CTTS J-H
184	8394216-5181	K7e (2); K7.5(8)	K7.5	-34.9	0.5	$1.40^{+2.18}_{-0.11}$	J-H
185	8394454-5823	K6.0(7)	K6.0	$0.86^{+1.42}_{-0.00}$	J-H
186	8395167-5024	M0.5(8); K5e(13)	M0.5	-89.3	0.1	$2.40^{+2.89}_{-0.00}$	CTTS J-H
187	8395780-5308	M1.5(8)	M1.5	-60.5	0.0	$3.42^{+3.55}_{-0.00}$	CTTS J-H
188	8396035-5861	$0.64^{+1.66}_{-0.00}$	CTTS J-H
189	8396285-5119	$1.63^{+0.49}_{-0.54}$	CTTS J-H

Table 4
(Continued)

Num. (1)	IRS Name (2)	Spectral Types (3)	Spectral Type Adopted(4)	EW($H\alpha$) (5)	EW(Li) (6)	A_V (7)	A_V Method (8)
190	8396319-4941	M2.5(8)	M2.5	-66.5	0.3	$4.24^{+1.90}_{-0.91}$	J-H
191	8396679-6167	K4.0(1)	K4.0	$3.65^{+2.27}_{-0.00}$	CTTS J-H
192	8397522-4788	M2.0(8)	M2.0	-94.1	0.5	$0.43^{+3.63}_{-0.00}$	CTTS J-H
193	8397632-5445	M0.5e (2); M0.5(8)	M0.5	-30.0	0.5	$0.74^{+5.03}_{-0.00}$	CTTS J-H
194	8397818-4972	$1.54^{+5.97}_{-0.00}$	CTTS J-H
195	8398707-5755	M2(3)	M2.0	$3.80^{+1.51}_{-0.17}$	CTTS J-H
196	8398936-6711	K7.5(1); M0(4); K4(10); K4.0(23)	K4.0	-27.9	0.6	$0.89^{+3.32}_{-0.00}$	CTTS J-H
197	8399022-5955	K7.5(1); M0.0(8); M0e(3); K7, M0 (13)	M0.0	-106.0	0.3	$0.47^{+3.90}_{-0.47}$	J-H
198	8399269-6612	K6.5(1); M0(4); M0(10); K7.6(23)	K7.5	-13.1	0.4	$1.55^{+2.16}_{-0.10}$	J-H
199	8399902-6268	M2.5(1); M0(4); K4.5(10); K7(17); K4.5(23)	K4.5	-4.0	0.4	$1.62^{+0.72}_{-1.62}$	J-H
200	8400080-6709	K5.5(1); K5(4); K5(10); K5.4(23)	K5.5	-42.2	1.2	$1.13^{+4.04}_{-0.00}$	CTTS J-H
201	8402765-6538	K6.5(1); K5(4); K5(10); K2.0(23)	K2.0	-22.0	0.5	$5.33^{+5.98}_{-0.00}$	CTTS J-H
202	8403455-6810	M0.5(1); M2(4); M0.5(10); M2.5(23)	M2.5	-38.8	0.4	$2.31^{+1.14}_{-0.00}$	J-H
203	8406280-6293	K5(4); K3(10); K3.3(23)	K3.5	-5.0	0.6	$0.68^{+2.78}_{-0.00}$	CTTS J-H
204	8406609-6247	M2.5(4); M2.5(8); M2.5(10); M2.6(23)	M2.5	-63.3	0.5	$0.44^{+1.34}_{-0.44}$	J-H
205	8407074-5195	K6(18); K4IV-Ve(2)	K4.0	$2.16^{+0.00}_{-1.68}$	H-K
206	8408920-6760	K5.0(1); Cs(11); K5.1(23)	K5.0	-17.0	0.5	$5.92^{+6.49}_{-1.51}$	CTTS J-H
207	8409911-6386	$12.20^{+5.56}_{-9.41}$	J-H
208	8410334-6291	K4e (11)	K4.0	$0.35^{+2.32}_{-0.35}$	I-J
209	8410779-6416	$23.60^{+10.16}_{-6.05}$	CTTS H-K
210	8410886-6134	M1.5(1); M0.0(23)	M0.0	-18.0	0.6	$1.78^{+2.52}_{-0.00}$	I-J
211	8411618-6426	M3.5(1); M3.5(8); M3(10); M4.3(23)	M4.5	-15.6	0.3	$0.31^{+0.14}_{-0.31}$	J-H
212	8412592-6712	M1.5(1); M2(4); M1.5(10); M1.3(23)	M1.5	-31.7	0.3	$8.01^{+1.37}_{-4.65}$	CTTS J-H
213	8413152-6141	K7.5(1); K5.0(23)	K5.0	-31.5	0.4	$2.00^{+2.64}_{-0.58}$	J-H
214	8413399-5287	M0.5(8); K8e (3)	M0.5	$0.61^{+5.39}_{-0.00}$	I-J
215	8413704-6739	M2.0(1); M2(4); M1.0(10); M2.0(23)	M2.0	-93.9	...	$3.74^{+5.93}_{-0.00}$	I-J
216	8414490-7187
217	8415394-6556	K7.0(1); K8(4); K8(10); K7.5(23)	K7.5	-153.0	...	$3.94^{+6.24}_{-2.49}$	J-H
218	8416389-6503	M4.5(1); M4.5(8); M4.5(23)	M4.5	-14.1	...	$0.07^{+0.89}_{-0.07}$	I-J
219	8416834-6225	M0.5(7); M0.5(8); M0.7(23)	M0.5	-8.2	0.6	$0.41^{+0.77}_{-0.35}$	I-J
220	8416914-6175	M0.0(1); K7.7(20)	K7.5	-19.2	0.3	$6.78^{+2.25}_{-4.27}$	CTTS J-H
221	8416978-6185	K7.5(1); K2.1(23)	K2.0	-45.9	0.3	$12.30^{+0.02}_{-12.12}$	H-K
222	8421949-6718	M0.5(1); M0.4(23)	M0.5	-4.1	0.5	$5.85^{+2.62}_{-3.36}$	J-H
223	8424570-6484	M3.0(7); M3.7(23)	M3.5	-10.1	0.4	$0.60^{+1.17}_{-0.60}$	I-J
224	8424689-6154	A0.0 (12); A2/3 (19); A2V (20)	A2.0	$1.26^{+7.85}_{-1.26}$	I-J
225	8425038-6557	K5.0(1); K0(13); G3.0(23)	G3.0	-18.6	0.5	$2.61^{+7.42}_{-0.45}$	I-J
226	8430527-6583	A3.5(1); A5II-IIIev (13); A6.9(23)	A7.0	-5.2	...	$0.83^{+7.56}_{-0.83}$	I-J
227	8440418-7404	M0.0(1); K7.9(23)	K8.0	-10.3	0.5	$2.02^{+6.24}_{-0.00}$	I-J
228	8443530-6843	M0.5(1); M0e(21); M1.0(23)	M1.0	-104.0	0.4	$0.66^{+1.85}_{-0.23}$	I-J
229	8444779-6608	<M0.0(7); M0.3(23)	M0.5	-3.1	0.6	$3.20^{+1.44}_{-0.95}$	J-H
230	8445558-6860	M0(SpeX); M3.5(23)	M3.5	-13.1	0.5	$1.41^{+1.05}_{-1.20}$	J-H
231	8447398-6788	M3.0(7)	M3.0	$20.20^{+9.12}_{-6.72}$	J-H
232	8448350-6815	M0.0(1)	M0.0	$8.25^{+4.39}_{-4.00}$	CTTS J-H
233	8450343-7265	M1.5(1); K7(21); M3.2(23)	M3.0	-126.0	0.4	$0.64^{+1.24}_{-0.00}$	I-J
234	8452061-7269	M0.5(1); M1.0(23)	M1.0	-7.1	0.5	$1.35^{+5.65}_{-0.00}$	I-J
235	8453876-6821	A3.5(1); A5e(22)	A3.5	$3.58^{+9.18}_{-3.58}$	I-J
236	8455602-7112	M1.0(1); K4.5(10); K4.5(23)	K4.5	-5.4	...	$8.89^{+5.73}_{-2.94}$	H-K
237	8457266-7161	M1.5(7); M2.9(23)	M3.0	-11.0	0.4	$4.20^{+1.97}_{-2.51}$	J-H
238	8461533-6914	K6.0(1); K7.5(23)	K7.5	-21.1	0.6	$0.67^{+2.44}_{-0.67}$	CTTS J-H
239	8464666-7838	M1.0(1); K5e(13); K4.2(23)	K4.0	-25.5	0.6	$0.00^{+1.51}_{-0.00}$	I-J
240	8465247-7776	M1.5(1); M2.3(23)	M2.5	-12.6	0.5	$0.85^{+0.99}_{-0.85}$	J-H
241	8466711-6987	K6.0(1); M0.5(23)	M0.5	-162.0	...	$3.70^{+5.45}_{-0.00}$	CTTS J-H
242	8468002-6969	K7.5(10)	K7.5	-88.3	...	$11.30^{+5.04}_{-0.98}$	J-H
243	8468729-6970	M1.0(10); K7.3(23)	K7.5	-77.0	0.5	$8.42^{+3.77}_{-1.29}$	J-H
244	8469891-7104	M1.5(1); M1.0(10); M1.0(23)	M1.0	-76.8	...	$9.43^{+4.21}_{-1.41}$	J-H
245	8472719-7464	M2.0(1); K7.4(23)	K7.5	-159.0	0.3	$5.81^{+4.10}_{-4.22}$	CTTS J-H
246	8476732-7058	K7.5(1)	K7.5	-66.8	...	$9.16^{+4.09}_{-3.71}$	J-H

Table 4
(Continued)

Num. (1)	IRS Name (2)	Spectral Types (3)	Spectral Type Adopted(4)	EW($H\alpha$) (5)	EW(Li) (6)	A_V (7)	A_V Method (8)
247	8477229-7184	M3.0(1); M0.2(23)	M0.0	-63.6	0.4	$5.85_{-2.36}^{+2.62}$	J-H
248	8486920-7342	$20.40_{-3.12}^{+11.34}$	CTTS H-K
249	8488472-7373	M2.5(SpeX)	M2.5	$0.39_{-0.39}^{+3.61}$	CTTS J-H
250	8492690-7387	$15.70_{-4.37}^{+6.72}$	CTTS J-H
251	8494096-7377	$14.60_{-3.88}^{+6.33}$	CTTS J-H
252	8495155-7404	$19.30_{-2.25}^{+10.44}$	CTTS H-K
253	8497290-7502	$21.50_{-4.05}^{+6.21}$	CTTS H-K
254	8497797-7462	$34.50_{-16.52}^{+4.69}$	CTTS H-K
255	8499151-7482	$32.00_{-31.32}^{+4.68}$	CTTS H-K
256	8499541-7426	$13.10_{-0.52}^{+7.98}$	CTTS J-H
257	8502614-7795	M3.0(1); M3.1(23)	M3.0	-263.0	0.3	$0.48_{-0.46}^{+1.35}$	I-J
258	8504327-7460	K7.0(1)	K7.0	$9.96_{-3.96}^{+4.45}$	J-H
259	8508083-8237	K7e(4); K7.0(10); K7.0(23)	K7.0	0.0	...	$6.92_{-4.23}^{+6.23}$	CTTS J-H
260	8508501-7431	M2.0(1); M1.3(23)	M1.5	-24.9	0.5	$0.87_{-0.56}^{+1.87}$	I-J
261	8508648-7916	$7.69_{-3.57}^{+4.90}$	CTTS J-H
262	8510403-8125	K0e(4); K0(10); G4.1(23)	G4.0	-46.9	0.3	$2.00_{-1.40}^{+6.06}$	I-J
263	8511308-8126	M3e(4); M3(10); M5.0(23)	M5.0	-57.2	0.4	$0.63_{-0.45}^{+4.39}$	CTTS J-H
264	8511602-7926	$8.46_{-4.29}^{+3.68}$	CTTS J-H
265	8514861-7663	$11.00_{-6.11}^{+4.87}$	CTTS J-H
266	8515568-8067	F0-G0e(4); F(10); F5.0(23)	F5.0	0.0	...	$6.60_{-5.76}^{+3.01}$	J-H
267	8516031-7796	$22.00_{-4.67}^{+10.21}$	CTTS H-K
268	8518798-7373	$2.36_{-1.42}^{+8.18}$	CTTS J-H
269	8519260-8090	K4.0(1); K1e(4); K1(10); K3.0(23)	K3.0	-18.3	0.5	$3.09_{-1.94}^{+3.27}$	J-H
270	8519428-8120	K7(4); K7(10); K7.0(23)	K7.0	0.0	...	$8.58_{-4.53}^{+3.83}$	J-H
271	8520557-7775	M2.0(SpeX); M0.2(23)	M0.0	-67.9	...	$6.33_{-2.09}^{+4.33}$	H-K
272	8520580-7960	$8.74_{-8.74}^{+3.89}$	J-H
273	8530851-8132	M2(1); M2(4); M2(10); M2.1(23)	M2.0	-7.2	0.4	$1.41_{-0.33}^{+2.58}$	J-H
274	8534457-7821	$17.60_{-4.14}^{+7.90}$	CTTS H-K
275	8535781-7830	<M5.0(7); K7.0(23)	K7.0	-6.9	0.5	$4.26_{-0.71}^{+4.62}$	J-H
276	8536129-8706	$14.50_{-1.54}^{+8.11}$	CTTS J-H
277	8537742-8080	K7e(4); K7(10); K7.0(23)	K7.0	-40.0	...	$6.88_{-3.10}^{+4.84}$	CTTS J-H
278	8538844-7917	M2(11); K7.0(23)	K7.0	-18.7	0.4	$0.90_{-0.00}^{+5.22}$	I-J
279	8538911-7999	M1.5(10); M1.5(23)	M1.5	-69.8	...	$8.00_{-4.26}^{+3.80}$	H-K
280	8542681-8618	K7.0(1); K1.0(23)	K1.0	-26.7	0.4	$5.43_{-3.06}^{+2.67}$	J-H
281	8543224-7972	M5.5(10); M7.4(23)	M7.5	-247.0	...	$0.59_{-0.00}^{+2.31}$	I-J
282	8545724-8008	K5(4); K5(10); K5.0(23)	K5.0	-18.0	...	$0.03_{-0.03}^{+7.29}$	I-J
283	8547523-7831	M2.0(7); M4.5(23)	M4.5	-14.5	...	$0.70_{-0.54}^{+1.65}$	J-H
284	8547770-7986	K8(4); K3.5(10); K3.5(23)	K3.5	-6.6	0.6	$5.07_{-2.05}^{+3.34}$	J-H
285	8552157-8190	$12.70_{-3.33}^{+5.54}$	CTTS J-H
286	8552280-8641	M3.0(1); M1.0(23)	M1.0	-10.0	0.8	$2.95_{-1.35}^{+1.71}$	J-H
287	8556074-7982	M3.5(10); M2.8(23)	M3.0	-34.5	0.4	$2.01_{-0.77}^{+0.89}$	J-H
288	8560743-8147	M2.5(10); M2.0(23)	M2.5	-115.0	...	$3.36_{-1.26}^{+1.93}$	J-H
289	8561044-7980	K6.0(10); K7.2(23)	K7.0	-130.0	0.3	$4.00_{-1.50}^{+3.74}$	CTTS J-H
290	8562845-8151	M2.5(1); M2.8(23)	M3.0	-46.1	...	$2.58_{-1.93}^{+4.21}$	I-J
291	8564835-8250	M2.5(1); M1.8(23)	M2.0	-40.0	0.5	$2.14_{-0.80}^{+1.17}$	J-H
292	8567003-8669	M1.0(1); M2.4(23)	M2.5	-105.0	0.3	$0.91_{-0.00}^{+7.15}$	I-J
293	8567545-8254	M3.0(1); M1(4); M1.0(10); M3.0(23)	M3.0	-155.0	0.3	$3.40_{-1.63}^{+3.55}$	CTTS J-H
294	8567670-8803	M2.5(SpeX); M2.0(23)	M2.0	-2.9	...	$7.71_{-2.38}^{+4.25}$	H-K
295	8569204-8666	K4.0(23)	K4.0	-3.1	0.4	$5.46_{-2.99}^{+4.95}$	CTTS J-H
296	8570200-8276	$17.50_{-3.00}^{+8.92}$	CTTS J-H
297	8570949-8577	$19.90_{-19.90}^{+4.61}$	CTTS H-K
298	8571439-8650	-47.0	...	$6.72_{-3.99}^{+4.28}$	CTTS J-H
299	8574645-8156	M1.0(1); M1(4); M1.0(10); M0.5(23)	M0.5	-65.8	0.4	$2.34_{-1.24}^{+2.06}$	J-H
300	8576640-8652	M1.4(23)	M1.5	-11.1	0.7	$4.70_{-1.45}^{+3.02}$	H-K
301	8576836-8303	M3.5(1); M2.5(23)	M2.5	-4.3	0.4	$2.92_{-0.14}^{+1.31}$	J-H
302	8579480-8565	M(SpeX)	M
303	8580634-8516	M3.0(7)	M3.0	$6.92_{-2.14}^{+4.90}$	H-K

Table 4
(Continued)

Num. (1)	IRS Name (2)	Spectral Types (3)	Spectral Type Adopted(4)	EW(H_{α}) (5)	EW(Li) (6)	A_V (7)	A_V Method (8)
304	HOPS-22	$7.09^{+0.94}_{-5.04}$	CTTS J-H
305	HOPS-26	M2.0(9)	M2.0	$0.73^{+4.21}_{-0.00}$	CTTS J-H
306	HOPS-51	$11.80^{+11.97}_{-0.00}$	J-H
307	HOPS-54	M3.5(3)	M3.5	$0.72^{+1.68}_{-0.72}$	J-H
308	HOPS-98	$19.40^{+11.70}_{-1.03}$	CTTS J-H
309	HOPS-113	$22.00^{+4.69}_{-21.90}$	CTTS H-K
310	HOPS-151	$4.96^{+8.82}_{-0.00}$	CTTS J-H
311	HOPS-162	M2.0(10)	M2.0	$2.25^{+1.34}_{-0.03}$	J-H
312	HOPS-180	$0.00^{+5.45}_{-0.00}$	CTTS J-H
313	HOPS-184	$1.37^{+3.49}_{-1.37}$	CTTS J-H
314	HOPS-201	M3.0(24)	M3.0	$0.24^{+0.90}_{-0.00}$	I-J
315	HOPS-222	$14.50^{+8.11}_{-1.54}$	CTTS J-H
316	HOPS-272	$12.30^{+6.02}_{-6.16}$	CTTS J-H
317	HOPS-277	$9.85^{+4.91}_{-1.72}$	CTTS J-H
318	HOPS-283	M1.0(24)	M1.0	$4.26^{+2.22}_{-1.26}$	J-H
319	HOPS-293	$2.75^{+9.91}_{-0.00}$	CTTS J-H

Notes. The methods or literature references for spectral type determination are indicated with parentheses, and the meanings of the numbers in parentheses are as follows: (1) Allen & Mosby (2008), private communication; spectral types are measured from HECTOSPEC spectra; (2) Hillenbrand (1997); (3) Rebull et al. (2000); (4) Allen (1995); (5) Wolff et al. (2004); (6) Hillenbrand & Carpenter (2000); (7) Hernandez (2008), private communication; (8) Hernandez & Tobin (2009), private communication; spectral types are measured from HECTOSPEC spectra or FAST spectra; (9) da Rio et al. (2010); (10) Fang et al. (2009); (11) Parihar et al. (2009); (12) Manoj et al. (2006); (13) Herbig & Bell (1988); (14) Glebocki & Gnacinski (2005); (15) Daemgen et al. (2012); (16) Grankin et al. (2007); (17) Riaz et al. (2006); (18) Rebull (2001); (19) Houk & Swift (2000); (20) Ochsenbein (1980); (21) Wouterloot & Brand (1992); (22) Caratti O Garatti (2012); (23) Hsu et al. (2012); (24) Fang et al. (2013); (SpeX) Spectral typing with SpeX spectra in this work.

The units for columns (5) and (6) are \AA . $EW_{H_{\alpha}}$ and EW_{Li} values are from Hernandez (2008); Hernandez & Tobin (2009); Hsu et al. (2012). Column (7) is the adopted A_V and the range of A_V values calculated by several methods described in the text. Column (8) A_V method: the method used to derive the adopted A_V in the column(7).

(This table is available in its entirety in machine-readable form.)

Table 5
K-S Test for the Visual Extinction Distribution

Regions Compared	All Objects		Available Spectral Types	
	D	p	D	p
Trapezium versus ONC	0.30	$\ll 0.001$	0.25	0.03
Trapezium versus L1641	0.30	$\ll 0.001$	0.25	0.03
ONC versus L1641	0.19	0.02	0.21	0.04

Note. D is the maximum deviation between the cumulative distribution of two groups. p indicates the probability that there is no significant difference between the distributions.

3. BASIC CHARACTERISTICS OF THE STARS

3.1. SpTs and Effective Temperatures

For the most part, we gathered the SpT of our targets from the literature (Allen 1995; Hillenbrand 1997; Rebull et al. 2000; Fang et al. 2009; Parihar et al. 2009; da Rio et al. 2010; Hsu et al. 2012). We also added unpublished results kindly provided by John Tobin and Jesús Hernández. We utilized SpeX spectra to determine SpTs for objects without SpT information from the literature. As we have described (Kim et al. 2013), to determine SpT from SpeX spectra, we compared absorption features of Na I, Al I, Mg I, Ca I, and CO in source spectra with those of template spectra (Cushing et al. 2005;

Rayner et al. 2009). In addition, we have updated SpTs adopted in Kim et al. (2013) with SpTs for L1641 young stars from Hsu et al. (2012). SpTs of OriA-230, OriA-271, and OriA-294 derived previously from SpeX spectra (M0.0, M2.0, and M2.5 respectively) were replaced with the SpTs of Hsu et al. (2012) (M3.5, M0.2, and M2.0, respectively). These modest differences in SpTs between our determination and Hsu et al. (2012) ($\Delta(\text{SpT}) = 3.5, 1.8, \text{ and } 0.5$, respectively) prove that our SpT derivation using SpeX spectra is sufficient to narrow the SpT range down to two to three subtypes. Hence, we still adopt SpTs derived from SpeX spectra for seven objects (OriA-11, 16, 29, 34, 249, and 302) because there is no alternative in the literature for them. The SpTs reported in the literature and the adopted SpTs are listed in Table 4. In most cases, the reported SpTs for an object agree in a few subtypes. Less than 10% of the objects with known SpTs have a broad range of reported SpTs.

The SpT distribution for objects with available SpT information is shown in Figure 4. The distribution shape of the histograms generally agrees with the previous studies of objects in the ONC (Hillenbrand et al. 2013) and in L1641 (Fang et al. 2013; Hsu et al. 2013), even though we do not have complete SpT information. The total number of objects with known SpT is 229: 48 objects in Trapezium with partial IRS spectra, and 181 objects for which we have the full range of IRS spectra in the ONC (89 objects) and L1641 (92 objects). The fractions of our IRS targets for which we have SpTs are 77%, 67%, and 74% for the Trapezium, the ONC, and L1641,

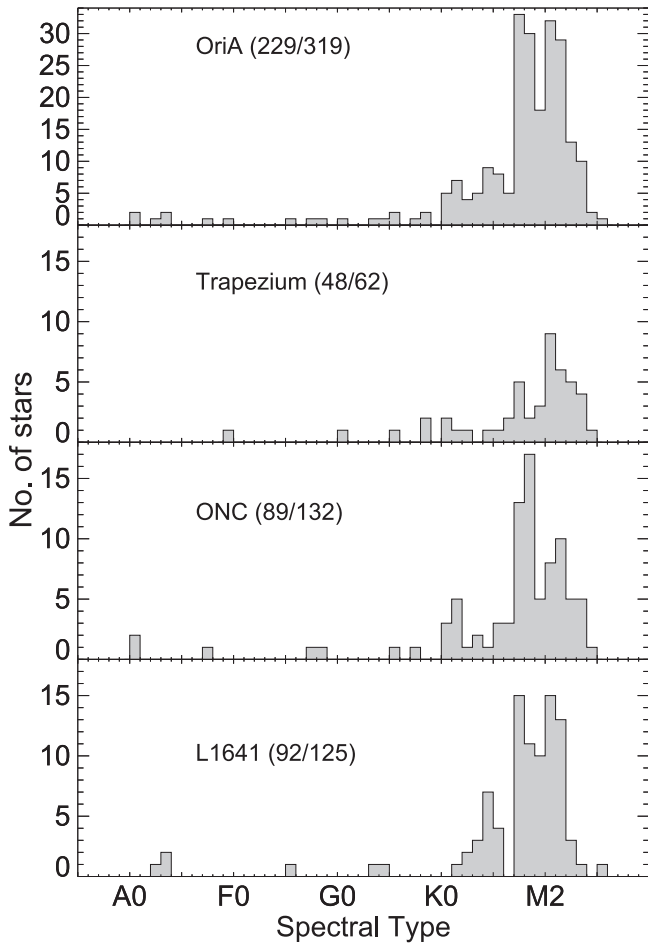


Figure 4. SpT distribution of Class II objects in Orion A that have available SpTs among those observed with IRS. (Note: OriA-227 is classified as K7.9, and it is the only one we adopted as K8. We merged the bin of K8 into the bin of M0 in order to plot the histogram in the same binning scheme in the literature.)

respectively. The median SpT of Class II objects in Orion A is M0: M1 for objects in the Trapezium, M0 for objects in the ONC, and M1 for objects in L1641 (see Figure 4).

We adopted the effective temperature (T_{eff}) and bolometric correction (BC) scale for PMS stars derived by Pecaut & Mamajek (2013). They found that PMS T_{eff} are ~ 250 K cooler than MS T_{eff} for G5 through K6 types, while other SpTs' T_{eff} agree in ~ 100 K between PMS stars and dwarfs. The accounted-for systematic plus statistical uncertainty of PMS T_{eff} is less than 1% of T_{eff} (Pecaut & Mamajek 2013). These new scales for PMS stars are fully available only for SpTs F0 to M5 in Table 6 in Pecaut & Mamajek (2013). For SpTs earlier than F0 and later than M5, we consulted with M. Pecaut & E. Mamajek (2013, private communication) to find the best way, and we adopted the following combination. For SpTs earlier than F0, we took the T_{eff} and BC scales for dwarfs in Table 5 in M. Pecaut & E. Mamajek (2013, private communication). For SpTs later than M5, we adopted the T_{eff} of dwarfs for SpTs later than M5, and we used the BC scale of PMS. For the objects of unknown SpTs, we adopted an effective temperature of 3770 K, which is the temperature of the mean SpT (M0) of Class II sources with known SpT in Orion A. The uncertainty of T_{eff} lies within the typical uncertainty of SpTs, which can be translated into about 345 K as a median temperature difference between a few (~ 3) sub-SpT differences. We adopt it as a typical uncertainty of T_{eff} .

3.2. Extinction Correction

We correct for extinction toward our sources to minimize the extinction effects on disk classification and interpretation of our data. The method for estimating visual extinction (A_V) toward our targets is described in detail in Kim et al. (2013). Basically, we use the relationship

$$A_V = \frac{\frac{A_V}{A_{\lambda_2}}}{\frac{A_{\lambda_1}}{A_{\lambda_2}} - 1} \times E(\lambda_1 - \lambda_2), \quad (1)$$

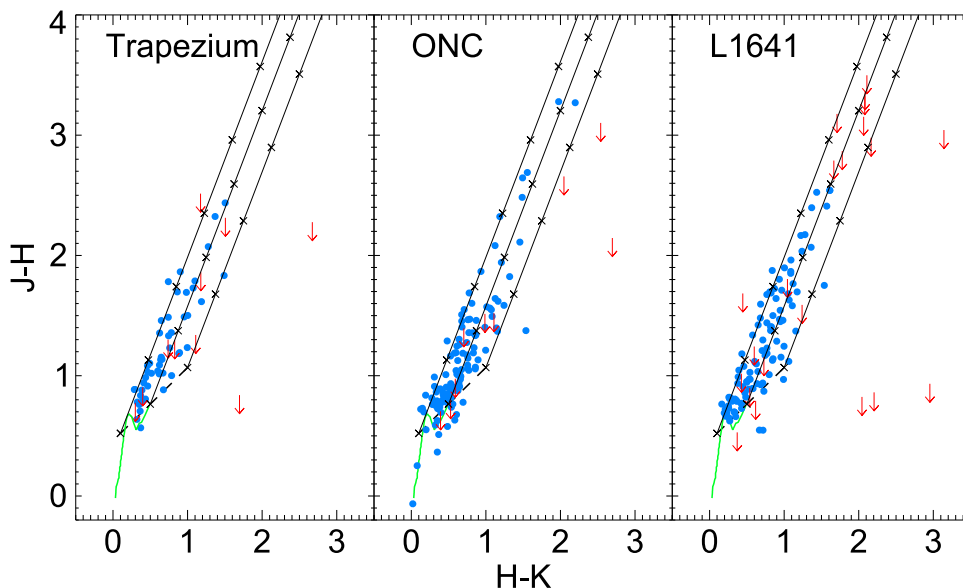


Figure 5. $J - H$ vs. $H - K$ color-color diagram of Class II objects observed with IRS in the subregions of Orion A: Trapezium (left panel), the ONC (middle panel), and L1641 (right panel). J , H , and K photometry is from 2MASS. The CTTS locus is indicated with the dashed line. The colors of main-sequence giants and dwarfs (Bessell & Brett 1998) are also plotted with a green solid line. The solid lines started from the CTTS locus indicate the increasing extinction. The increments of A_V are denoted by crosses by the interval of $A_V = 5$. The downward-pointing arrows are used for objects for which their 2MASS photometry has any bad flags.

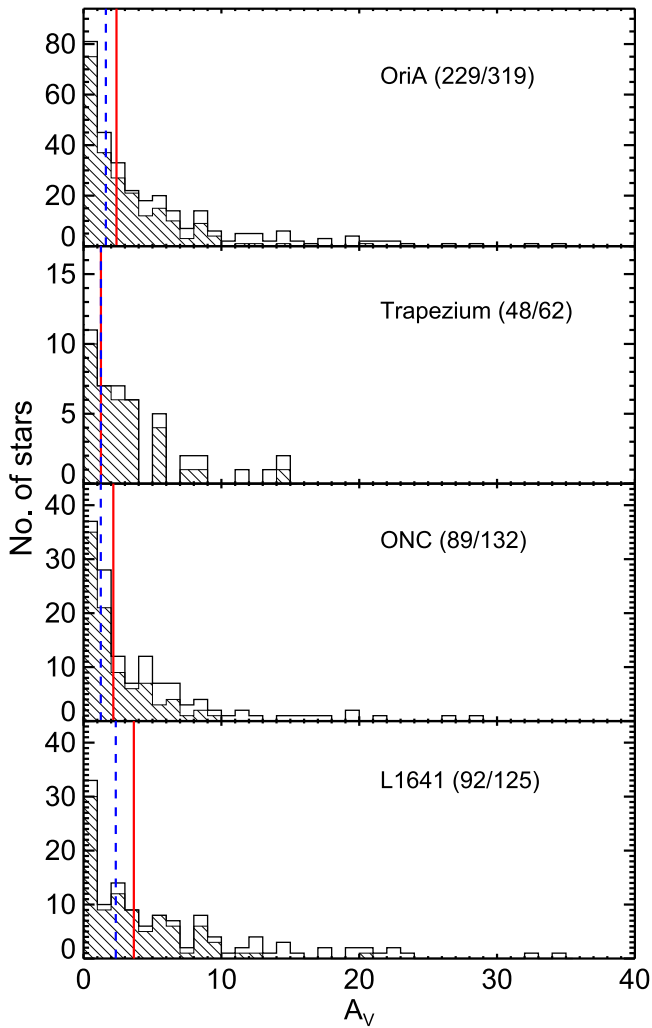


Figure 6. Distribution of visual extinction, A_V , for 319 Class II disks in Orion A observed with IRS. Hashed lines indicate the A_V distribution of the objects with known SpT information. The solid vertical lines indicate the median A_V of all objects. The dashed lines are for the median A_V of the objects with available SpTs. The numbers in each panel are for the number of objects with available SpTs and the number of objects without regard to the availability of SpT.

where $E(\lambda_1 - \lambda_2)$ is the color excess between two wavelengths (λ_1 and λ_2), which is equal to $([\lambda_1] - [\lambda_2])_{\text{obs}} - ([\lambda_1] - [\lambda_2])_{\text{int}}$. To derive the color excess, $E(\lambda_1 - \lambda_2)$, we take J , H , and K bands from 2MASS and I and J bands from DENIS and adopt $I - J$, $J - H$, and $H - K$ photospheric colors from Pecaut & Mamajek (2013). For sources without available SpT information, we adopt an intrinsic color from $J - H$ and $H - K$ of the CTTS locus of colors from Meyer et al. (1997). The CTTS locus is indicated over the color-color diagram of our sample using 2MASS photometry in Figure 5. In Equation (1), A_λ is the extinction at a wavelength of λ . We assume the optical total-to-selective extinction ratio, R_V , to be 5 because (1) R_V values of dense clouds are usually between 4 and 6 (Mathis 1990) and (2) measures of R_V for lines of sight in Orion have confirmed that $R_V \sim 5$ (Cardelli et al. 1989). Therefore, we make use of the extinction curve with $R_V = 5.0$ from Mathis (1990) to obtain A_λ at the wavelengths of the I , J , H , and K bands.

We employ extinction laws depending on the A_V values inferred from Equation (1). We take the Mathis (1990) extinction curve with $R_V = 5.0$ in the case of $A_V < 3$. If $A_V > 3$, we used the extinction curve corrected for standard-star photospheric SiO absorption near $8 \mu\text{m}$ (S. Fogerty 2014, private communication) from the empirical extinction curves of McClure (2009), which present two composite extinction curves, one for $3 < A_V < 8$ and one for $A_V > 8$.

To select a final A_V for an object, we examine the SEDs that are extinction corrected with the derived A_V values from each intrinsic color choice. We make a judgment based on freedom from artifacts of the correction (e.g., artificial CO_2 ice features or spurious structure in the silicate features) and good agreement with the photospheric spectrum of the star's type, to find the most reasonable A_V . In spite of our best effort of judgment, we have some ($\sim 10\%$) objects that show modest or strong UV/optical excess in the extinction-corrected SEDs. There are several possible explanations for the UV/optical excess, including contributions from background nebulosity, jets, over-correction of extinction, and/or less accurate photometry, if not all. The overcorrection of reddening seems to be frequent in cases in which the SpT of an object is not known. We speculate that the following objects are overcorrected: OriA-31, 54, 65, 162, 207, 251, 255, and 297 due to the limit of SpT information, and OriA-221 and 231 due to some other reason, since none of the various values of A_V are reasonable. We find frequently that photometry data from NOMAD show a sudden increment compared to other photometry, and the objects suffering this problem are OriA-30, 58, 66, 84, 97, 103, 127, 128, 183, 190, 192, 194, 206, and 222. They are usually located in nebulous regions. Another group for which we consider nebulosity and jets as possible contributors comprises OriA-3, 30, 37, 78, 81, 86, 90, 91, 122, 125, 217, 242, and 259. Among them, OriA-37, OriA-90, and OriA-91 are related to HH 505, HH 885, and HH 888, respectively. Even though we do not know the SpT of OriA-207, it could be an edge-on disk because it shows up as an hourglass shape in the SDSS9 scattered light image. As can be seen from the preceding discussion, there is difficulty in measuring accurate extinction. We present final A_V values and uncertainties along with the A_V method selected for each object: $I - J$, $J - H$, and $H - K$ in Table 4.

The estimation of extinction bears several sources of uncertainty: the uncertainties of photometry, intrinsic color, SpT, and extinction curve. We do not account for all of those uncertainties because those uncertainties are not larger than the range of A_V values estimated through different choices of color excess described above. We indicate the range of A_V values for each object with the finally selected A_V in Table 4. The range of A_V values for most objects lies in a few magnitudes: the average offset of the smallest from the adopted A_V is 1.65 for objects that have a lower offset of less than 3 mag (77%); the average difference between the highest and the adopted A_V is 1.67 for objects that have an offset less than 3 mag (43%). Only 2% of our sample has a lower or upper offset greater than 10 mag from the adopted A_V .

The distributions of the visual extinctions according to the subregions of Orion A are shown in Figure 6. When taking only objects with known SpTs, the median A_V of L1641 ($A_V = 2.34$) is higher than that of the Trapezium ($A_V = 1.26$) or the ONC ($A_V = 1.25$). We performed Kolmogorov-Smirnov (K-S) tests on the distributions of A_V of pairs of subregions and list the results in Table 5. From the K-S test, where D is the

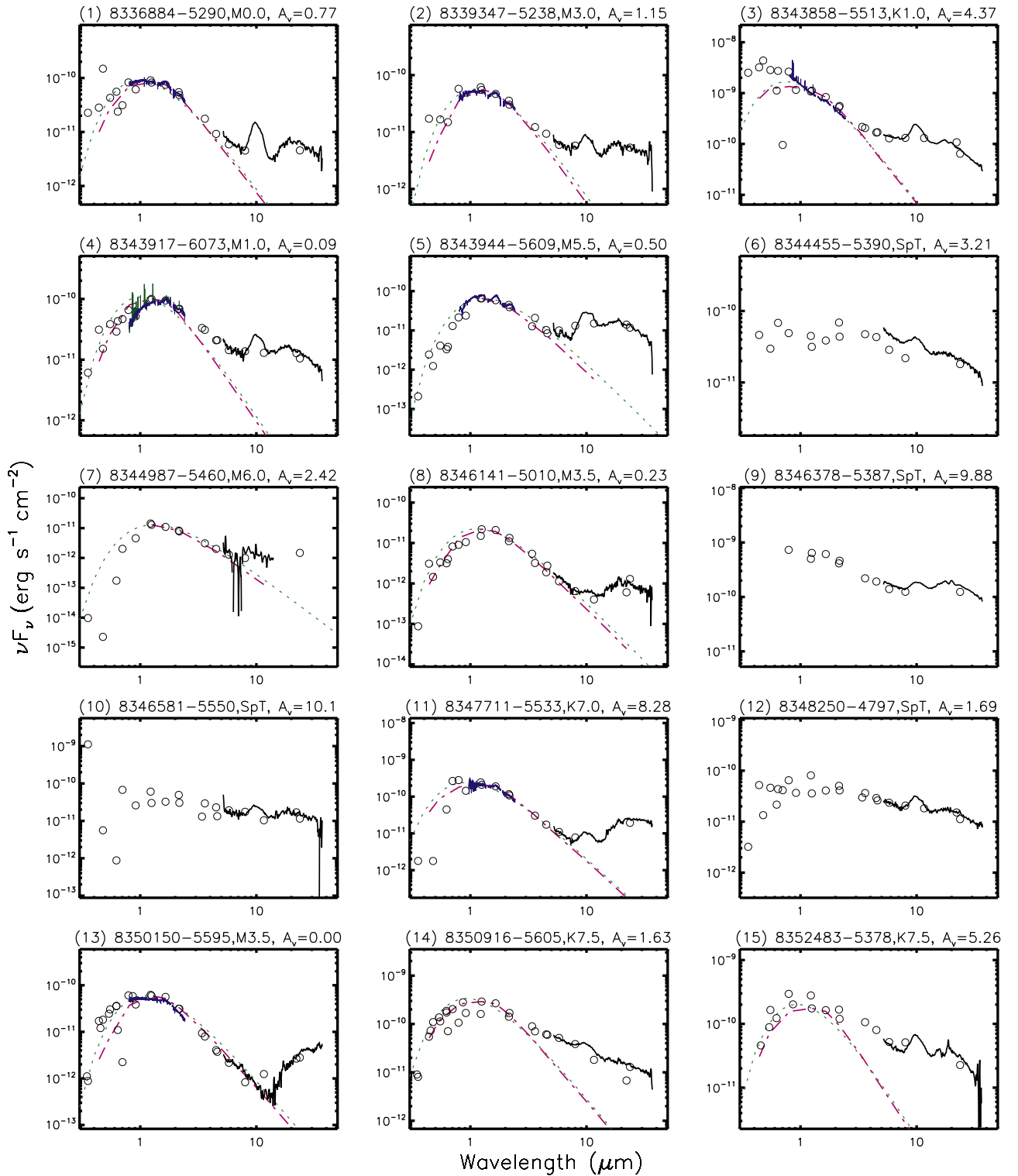


Figure 7. Dereddened SEDs of our samples in the ONC and L1641, which were observed with IRS SL and LL modules. The SEDs are composed of the following components: IRS (solid line in the wavelength range of 5.2–35 [or 14] μm); SpEx (solid line in the wavelength range of 0.8–2.4 μm); photospheric models: a blackbody radiation of the host star’s effective temperature (short-dashed line) and a photosphere derived from the intrinsic colors from Pecaut & Mamajek (2013) (long dot-dashed line); photometric data (open circles): UBVR1 from da Rio et al. (2010), SDSS, UKIDSS, *BVR* from NOMAD, DENIS *IJH*, 2MASS *JHK*, IRAC, MIPS (24 μm), and *WISE*. (An extended version of this figure is available.)

maximum difference between the empirical distribution function of two groups and p indicates the probability that there is no significant difference between the distributions, we confirm that the difference of A_V distributions by subregions is real and significant. The differences are caused by the following

mechanisms: (1) less extinction for the objects located in a cavity in the Trapezium and the ONC due to the strong UV field from OB stars in the Trapezium, which has blown out small dust grains (Hillenbrand 1997); (2) large extinction for the objects located inside of several local dark clouds in L1641.

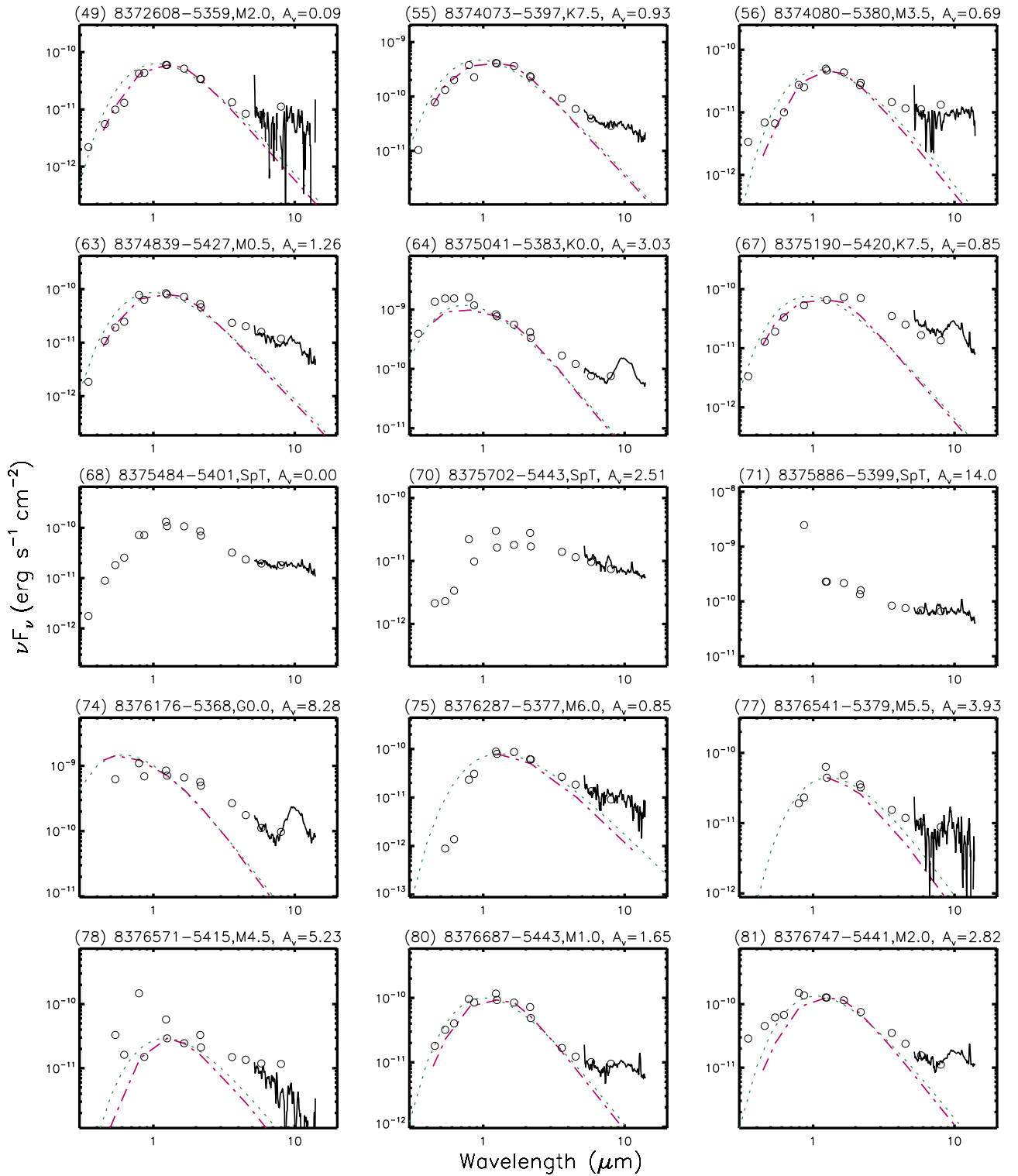


Figure 8. Dereddened SEDs of the reduced samples in Trapezium, which were observed with IRS SL module only. The meanings of symbols are the same as in Figure 7. (An extended version of this figure is available.)

We verified that the objects with the highest visual extinction values reside in denser clouds within this region. The trend of the A_V medians in the Trapezium, the ONC, and L1641 implies that most of the extinction is local, within the star-forming region and not along the largest part of the line of sight between Orion and Earth (observers).

3.3. Spectral Energy Distributions

We constructed SEDs of our sample with the broadband photometry that we assembled in Section 2.3 and SpeX and IRS spectra. We plot SEDs of 257 Class II objects observed in full IRS wavelength coverage from 5.2 to 37 μm in Figure 7. We only present the SEDs of 44 of 62 objects observed with

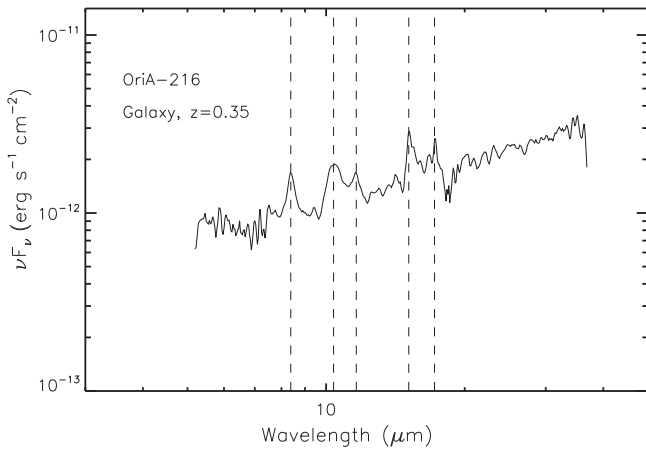


Figure 9. IRS spectrum of OriA-216, which is a background galaxy with redshift $z = 0.35$. The dashed lines indicate the PAH features of 6.2, 7.7, 8.6, 11.2, and 12.7 μm at the redshifted wavelengths at 8.38, 10.38, 11.63, 15.12, and 17.2 μm , respectively.

partial IRS wavelength coverage of 5.2–14 μm in Figure 8, because there are 18 objects in the Trapezium for which IRS spectral data were saturated at some wavelengths and hence unusable.

There are 10 spectra among 257 observed in full IRS wavelength coverage that we do not include our general analysis. We summarize these 10 objects below.

1. OriA-7, 88, 136, 148: they have incomplete spectra due to saturation.
2. OriA-247, 261, 296: they vary substantially over time.
3. OriA-216: we identify OriA-216 as a galaxy because the PAH features are located at redshifted wavelengths with $z = 0.35$ (Figure 9). It is also classified as a galaxy by SDSS classification (Aihara et al. 2011).
4. OriA-208: the SED of it includes interesting information: the system is revealed as a binary from SpeX observation, and SDSS and UKIDSS photometry agrees with our SpeX spectra of the fainter object. It was not possible to distinguish two sources from IRS because the separation is about 1–2 arcsec.
5. OriA-95: it is not a galaxy, but it has very uncertain extinction correction.

We do not include these 10 objects for the analysis in the present work, except OriA-88 in the analysis related to TDs.

There are many interesting individual objects in our survey. For example, we speculate possible variable sources based on the flux density disagreement of IRS spectrum with the IRAC and *WISE* photometry. The possible variability candidates are OriA-6, 9, 60, 61, 117, 166, 189, 190, 197, 202, 210, 212, 231, 244, 247, 256, 258, 261, 276, 277, 289, 301, 304, 316, and 318. We also find several objects with possible outer disk truncation based on the steeply decreasing emission beyond 20 μm : OriA-15, 45, 98, 173, 180, and 225.

A detailed description and discussion of individual objects are deferred to later papers.

3.4. Stellar Luminosity and Stellar Mass

The photospheric emission indicated with a long dot-dashed line in each SED in Figures 7 and 8 was derived from the intrinsic colors of Pecaut & Mamajek (2013) at temperature

T_{eff} , scaled to match the dereddened 2MASS *J*-band photometry (see SEDs in Figures 7 and 8). From the scaling factor, which is a solid angle applied to the photosphere model to get the observed flux density at *J* band and the assumed distance to Orion A ($d = 414$ pc), we estimate the stellar radius (R_*). We derived the stellar luminosity (L_*) of each object from T_{eff} and the stellar radius (R_*). The adopted T_{eff} and estimated L_* are listed in Table 6. We display the distribution of L_* of 291 objects from the samples in the ONC and L1641 in Figure 10. Performing a K-S test on the luminosity distributions of the ONC and L1641 regions, we conclude that there is no significant difference in the distribution of the luminosity of both regions.

To infer the stellar mass (M_*), we plot the derived L_* and T_{eff} of our targets on evolutionary tracks. In this paper, we use the Siess PMS evolutionary tracks (Siess et al. 2000). The adopted M_* in Table 6 are the average M_* read from the tracks of various metallicities. We take the standard deviation of M_* values measured in various metallicity conditions as the uncertainty of M_* . Figure 11 shows the objects with known SpTs in an H-R diagram along with the solar-metallicity ($Z = 0.02$) evolutionary tracks as an example. We compared M_* distribution for the Class II disks in the ONC and L1641 in Figure 12. There is no significant difference in the mass distribution of the two regions.

Since L_* and M_* distributions between the ONC and L1641 are not statistically very different, we will assume that any statistical differences between the two populations seen in further analysis with disk properties or star/disk accretion properties originate in disk properties, not in their stellar properties.

4. DISK PROPERTIES

4.1. Spectral Index

To deduce characteristics of disks, we measure the spectral indices defined as

$$n_{\lambda_1-\lambda_2} = \frac{\log(\lambda_2 F_{\lambda_2}) - \log(\lambda_1 F_{\lambda_1})}{\log(\lambda_2) - \log(\lambda_1)}, \quad (2)$$

where λ_1 and λ_2 are the anchor wavelengths. We use spectral indices to infer the radial and vertical distribution of dust. Spectral slopes between near-IR and mid-IR such as n_{K-25} , n_{5-12} , and n_{12-20} are the spectral indices commonly used for disk classification. We will discuss our usage of n_{K-25} , n_{5-12} , and n_{12-20} for disk classification in Section 4.3.

The indices most commonly used to infer the degree of dust settling (vertical structure) and inner/outer disk truncation (radial structure) are n_{K-6} , n_{6-13} , and n_{13-31} (e.g., McClure et al. 2010; Furlan et al. 2011; Manoj et al. 2011; Arnold et al. 2012). Using self-consistent disk models of T Tauri stars, D’Alessio et al. (2006) discussed the relation between the depletion (ϵ) of the small grains relative to the standard dust-to-gas mass ratio and the spatial distribution of the emergent flux, as well as the dependence of ϵ on other properties such as the radial structure and grain size distributions. The emitting regions, corresponding to fluxes emitted in certain wavelengths, change depending on dust grain sizes and degree of settling. For example, in a case of a model with ISM dust in the least settled disks with the largest depletion parameter ($\epsilon = 1$, i.e., no depletion of small grains in the upper disk layers), most (>90%) of the emergent flux

Table 6
Basic Stellar Properties and Mass Accretion Rate

Num.	IRS Name	T_{eff} (K)	L_* (L_{\odot})	M_* (M_{\odot})	\dot{M} (10^{-9}) ($M_{\odot} \text{ yr}^{-1}$)
1	8336884-5290	3770	0.66	0.49 ± 0.07	0.63 ± 0.11
2	8339347-5238	3360	0.41	0.29 ± 0.06	1.19 ± 0.96
3	8343858-5513	4920	12.12	2.67 ± 0.30	235.57 ± 133.24
4	8343917-6073	3630	0.79	0.40 ± 0.06	2.91 ± 0.45
5	8343944-5609	2840	0.48	0.15 ± 0.03	<9.79

(This table is available in its entirety in machine-readable form.)

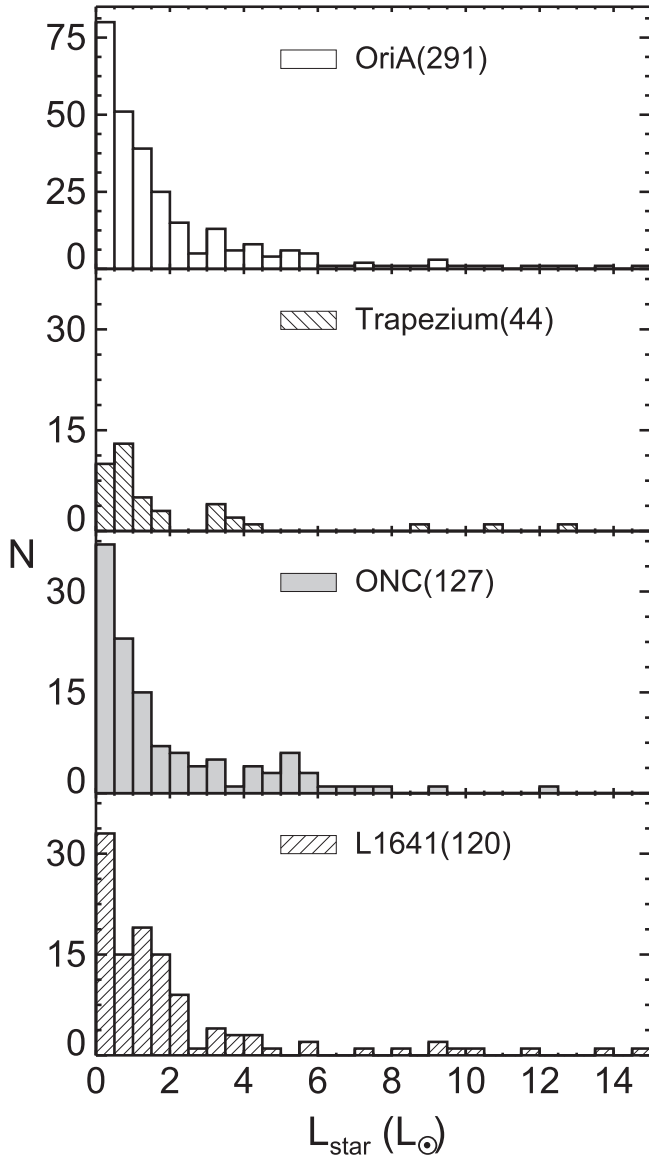


Figure 10. Distributions of L_* of the objects in Orion A.

at 6, 13, and 31 μm comes from less than 0.3, 10, and 75 AU from the host star, respectively, while the most emitted fluxes at 6, 13, and 31 μm are from less than 0.3, 5, and 10 AU, in the case of the most settled disk ($\epsilon = 0.001$, i.e., a factor of 1000 depletion of small grains in the upper disk layers; D’Alessio et al. 2006, Figure 9). The stellar temperature also affects the distance of the emitting regions from a host star.

Stars with higher effective temperature will have a 6 μm flux disk-emitting region beyond 0.3 AU, while this region will be closer to the host star if the star is colder than the effective temperature (4000 K) of a typical T Tauri star. Regardless of the host star’s temperature or the degree of disk settling, the wavelengths of 6, 13, and 31 μm are between the silicate emission features around 10 and 20 μm . Therefore, the spectral indices between two adjacent wavelength regions of them (n_{6-13} and n_{13-31}) are considered continuum spectral indices that can probe different regions of disks. In addition, we make use of n_{K-6} in order to measure characteristics of the innermost parts of disks.

The anchor positions for measuring spectral indices have been selected to be useful in comparison with radial properties of disks from various previous studies (Furlan et al. 2006; McClure et al. 2010; Manoj et al. 2011; Arnold et al. 2012). At each anchor wavelength, we averaged flux values from a small wavelength region to derive a representative flux value; so, for the 5 μm flux (“5”) we used the wavelength region 5.2–5.54 μm ; for “6” we used 5.4–6.0 μm ; for “12” we used 12.7–13.1 μm ; for “13” we used 12.8–14.0 μm ; for “20” we used 19.7–19.95 μm ; for “25” we used 24.5–25.5 μm ; for “31” we used 30.3–31.0 μm . For “K” we adopted the 2MASS K_s band: 2.00–2.31 μm).

Spectral indices measured with any combinations of two wavelengths, n_{K-6} , n_{6-13} , n_{13-31} , n_{5-12} , n_{12-20} , and n_{K-25} , are listed in Table 7. We report n_{20-31} , which is used as an index of outer disk truncation/evaporation in Section 6, in Table 11. The uncertainties reported with these spectral indices in Tables 7 and 11 are the propagated uncertainties from their spectra without including other uncertainties of determination of effective temperatures and extinction.

4.2. Parameters of the Degree of Dust Processing

Along with the continuum spectral indices, which are sensitive to the dust distribution within the disk, we can utilize some parameters that can be extracted from silicate features at 10, 20, and/or 33 μm to acquire¹⁵ clues of how many small dust grains are processed.

A parameter commonly used for understanding the strength of absorption or emission features is the equivalent width. The equivalent width for the silicate emission features is a measure of optically thin emission per unit area of underlying optically

¹⁵ We note that the crystalline olivine features at 33 μm are not reliable for most objects because there were many noisy pixels over this wavelength range. Therefore, we do not use EW33 for analysis in this work.

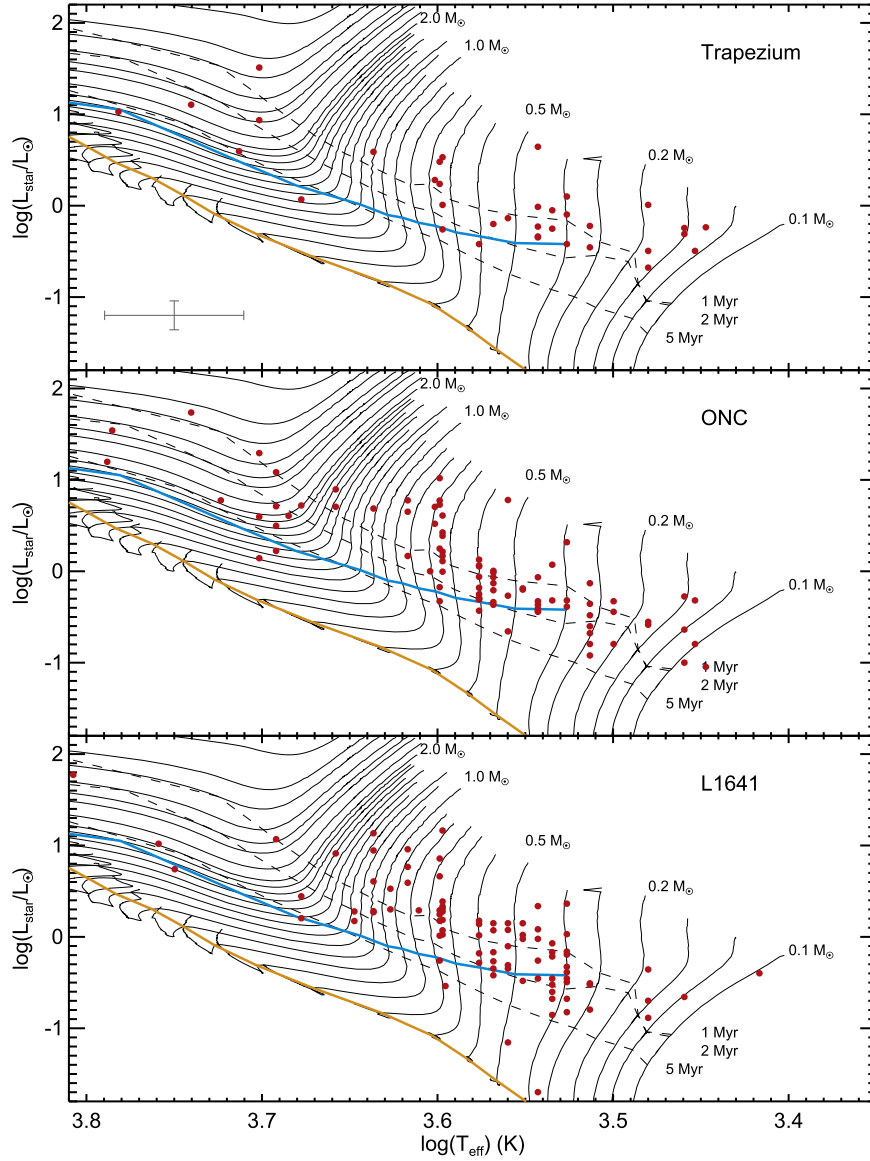


Figure 11. H-R diagrams for host stars of Class II objects in Orion A. Evolutionary tracks and isochrones are from Siess et al. (2000) ($Z = 0.02$). Isochrone ages of systems of Class II objects in Orion A range from <1 Myr to ~ 5 Myr. The average disk lifetime in Tau-Aur (Bertout et al. 2007) and the zero-age main sequence (ZAMS) are also shown as cyan and orange solid lines, respectively, for reference. The cross on the left bottom of the top panel represents a typical uncertainty in the SpTs of a few (~ 3) subclasses. The represented uncertainty is calculated by assuming that the uncertainty of T_{eff} is about 345 K, which is 0.16 in $\log(L_*/L_\odot)$ and 0.04 in $\log(T_{\text{eff}})$.

thick continuum:

$$EW(\lambda) = \int_{\lambda_1}^{\lambda_2} \frac{F_\lambda - F_{\lambda,\text{cont}}}{F_{\lambda,\text{cont}}} d\lambda, \quad (3)$$

where $F_{\lambda,\text{cont}}$ is the continuum emission determined from a polynomial fit to certain wavelength regions where the silicate emission features do not exist.

In the limit of small silicate feature optical depth, the equivalent width is proportional to the optical depth itself, or similarly the column density of dust in the inner disk (Watson et al. 2009). We compute EW10 and EW20 for amorphous silicate emission features around 10 and 20 μm . The wavelength ranges for integrating are 8–13 μm and 16–28 μm for 10 and 20 μm features, respectively. We list EW10 and EW20 in Table 8.

Another useful parameter is the integrated flux of the feature, $F(\lambda)$:

$$F(\lambda) = \int_{\lambda_1}^{\lambda_2} (F_\lambda - F_{\lambda,\text{cont}}) d\lambda. \quad (4)$$

$F(\lambda)$, the integrated flux after continuum subtraction, is a probe of the mass of dust lying in the uppermost surface of the disk, while $EW(\lambda)$ indicates the relative strength of the optically thin emission feature to the continuum emission from optically thick dust in the disk. We calculate $F10$ and $F20$ in the same wavelength limits used for the measurement of EW10 and EW20.

A parameter generally adopted as an index of the degree of dust processing is the ratio of the continuum-subtracted and normalized flux at 11.3 and 9.8 μm . This index, $F_{11.3}/F_{9.8}$, has been used to probe the degree of grain growth and crystallinity

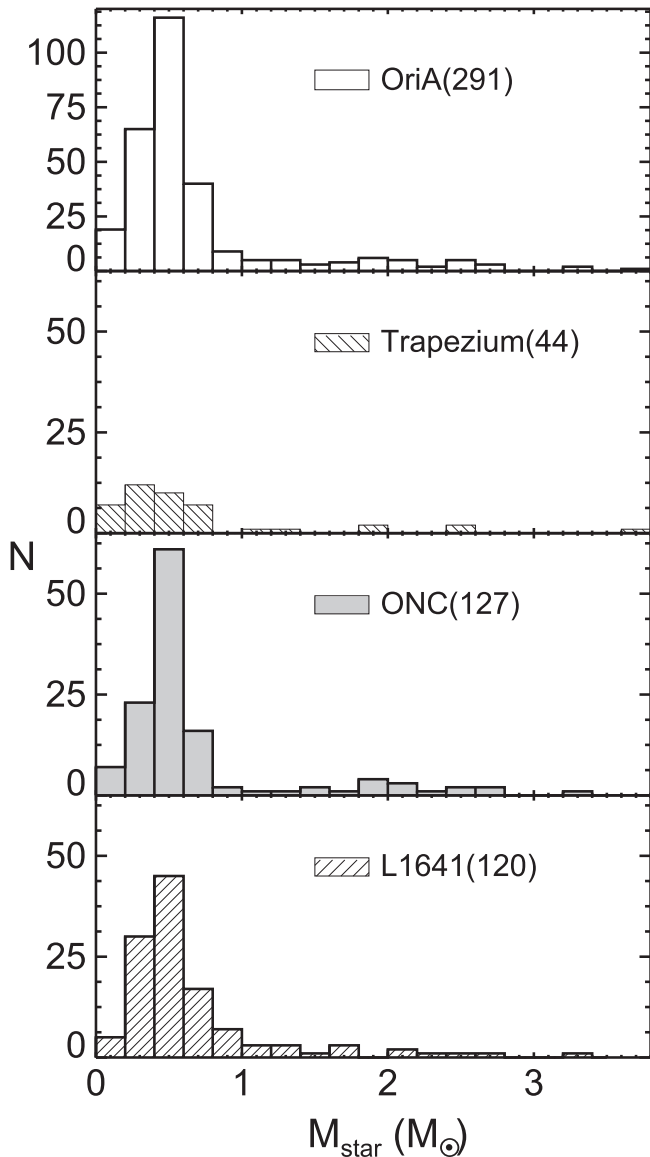


Figure 12. Distributions of M_{star} of the objects in Orion A.

in the inner (1–2 AU) parts of disks (Przygodda et al. 2003; van Boekel et al. 2005; Honda et al. 2006; Kessler-Silacci et al. 2006; Bouwman et al. 2008; Olofsson et al. 2009). When grains are still unprocessed and in their pristine state, amorphous silicate grains show a broad emission peak at $9.8 \mu\text{m}$. As small grains become crystallized, a strong feature at $11.2 \mu\text{m}$, due to forsterite, appears. Also, as grains grow, the broad amorphous silicate feature becomes flat topped. Therefore, $F_{11.3}/F_{9.8}$ is also known as a shape index because the shape of the silicate feature at $10 \mu\text{m}$ gets broader and flatter as the degree of crystallinity and grain growth gets higher with the larger values of $F_{11.3}/F_{9.8}$. Interstellar grains show narrow silicate profiles indicative of submicron, amorphous grains; protoplanetary-disk grains in addition have profiles with narrow substructure owing to crystallization and widening long wavelengths due to grain growth. Both forms of processing are captured in the $F_{11.3}/F_{9.8}$ (“shape”) index. Previous studies of dust features in Taurus disks (Sargent et al. 2009; Watson et al. 2009) found that the change in shape is mostly due to crystallization.

The major contributor to the uncertainties of extracting information from the silicate emission features at 10 and $20 \mu\text{m}$ is how to determine the underlying continuum. Based on our previous experiences (e.g., Manoj et al. 2011; Arnold et al. 2012), the determination of continuum of the $10 \mu\text{m}$ silicate feature is better than that of the $20 \mu\text{m}$ feature. We estimate the uncertainties of properties measured with $10 \mu\text{m}$ silicate features by assuming an uncertainty of 10% in the underlying continuum. We assume an uncertainty of 20% of the continuum for the measurement of EW20 and other properties measured from the $20 \mu\text{m}$ silicate feature. We report the parameters related to dust processing and their uncertainties in Table 8.

4.3. Disk Classification

4.3.1. Classification of Disks Using Continuum Spectral Indices

One assessment of the evolutionary state of a YSO comes from the slope of its SED (Lada 1987). Two wavelengths at near- and mid-IR, typically K ($\sim 2 \mu\text{m}$) and $25 \mu\text{m}$, have been used for YSO classification. n_{K-25} is used to define the SED classes: Class I if $n_{K-25} > 0.3$; FS if $-0.3 < n_{K-25} < 0.3$; Class II if $-1.6 < n_{K-25} < -0.3$; Class III for $n_{K-25} < -1.6$. However, as is well known, SED classification can also give a wrong impression of evolutionary state for objects viewed close to face-on or edge-on (Robitaille et al. 2006; Crapsi et al. 2008; McClure et al. 2010).

To minimize the extinction effect on evolutionary classification based on spectral indices, McClure et al. (2010) made good use of the “extinction-free” indices, n_{5-12} and n_{12-20} , which are independent of extinction because A_{λ} at the anchors are the same as in the McClure (2009) extinction curves, to classify the evolutionary stages of the YSOs in the Ophiuchus star-forming region (Oph). They calibrated their classification scheme with Class I, II, and III samples in Taurus (Furlan et al. 2006, 2008) and applied to Oph objects. It divides objects into photospheres ($n_{5-12} < -2.25$), disks ($-2.25 < n_{5-12} < -0.2$), and envelope ($n_{5-12} > -0.2$). The second extinction-free index, n_{12-20} , includes not only continuum but also the $20 \mu\text{m}$ silicate feature. This index is used to determine roughly how much the disk is cleared, i.e., to suggest candidates of debris disks or TDs. These extinction-free indices have been used in the literature (e.g., Furlan et al. 2011; Manoj et al. 2011; Arnold et al. 2012) as an initial filter to classify evolutionary stages of objects in the format of n_{K-25} versus n_{5-12} and n_{12-20} versus n_{5-12} .

In Figures 13 and 14 we apply n_{K-25} , n_{5-12} , and n_{12-20} spectral indices of the objects in our Orion A sample to classify their evolutionary stages. We see that our sample is mostly placed in the “Class II” (from n_{K-25}) and “disks” (from n_{5-12} and n_{12-20}) areas in Figures 13 and 14. Some objects, however, are located in the area for “TDs,” “FS,” or “envelopes.” We confirm that all Orion A objects that fall into the “TDs” region in Figure 14 are the TDs previously identified by Kim et al. (2013). Almost half of the objects in the “envelopes” area are also previously identified TDs, as indicated with open circles in Figure 14.

We notice that TDs that lie in the “envelopes” region due to their n_{5-12} values have $n_{12-20} \gtrsim 0$ for both the ONC and L1641 (see Figure 14). The list of objects that are not identified as TDs but located in the “envelopes” area is as follows, from high to low n_{12-20} : OriA-123, 159, 190, 21, 86, and 305 in the

Table 7
Spectral Indices

Num.	Module	n_{K-6}	$\sigma_{n_{K-6}}$	n_{6-13}	$\sigma_{n_{6-13}}$	n_{13-31}	$\sigma_{n_{13-31}}$	n_{5-12}	$\sigma_{n_{5-12}}$	n_{12-20}	$\sigma_{n_{12-20}}$	n_{K-25}	$\sigma_{n_{K-25}}$
1	SLLL	-2.07	0.10	-0.89	0.13	0.29	0.23	-1.03	0.10	0.95	0.15	-1.01	0.04
2	SLLL	-1.70	0.08	-0.53	0.11	0.06	0.16	-0.65	0.13	-0.18	0.18	-0.89	0.03
3	SLLL	-1.51	0.03	-0.27	0.03	-1.11	0.06	-0.32	0.04	-0.76	0.04	-1.01	0.01
4	SLLL	-1.62	0.11	-0.13	0.13	-0.66	0.06	-0.49	0.07	-0.17	0.24	-0.87	0.02
5	SLLL	-1.77	0.16	0.71	0.20	-0.80	0.11	0.35	0.10	-0.23	0.09	-0.66	0.04

Note. The wavelength interval for each anchor is as follows: The K band is at 2.17 μm ; 5 is for wavelengths of 5.2–5.54 μm ; 6 for 5.4–6.0 μm ; 12 for 12.7–13.1 μm ; 13 for 12.8–14.0 μm ; 20 for 19.7–19.95 μm ; 25 for 24.5–25.5 μm ; 31 for 30.3–31.0 μm .

(This table is available in its entirety in machine-readable form.)

ONC; OriA-311, 289, 191, 266, 209, 231, 258, 272, and 312 in L1641. We examine their SEDs and do not find strong evidence for envelopes, such as silicate absorption at 10 μm , CO₂ ice absorption at 15 μm , or steeply increasing flux after 20 μm . Instead, the common characteristics of their SEDs are that they show strong 10 and 20 μm silicate emission features with rather flatter and redder spectral index between 5 and 12 μm while having low/less excess over the photosphere at near-IR wavelengths (<5 μm). We investigate the possibility of introducing a strong 10 μm silicate feature by overcorrecting of extinction. We find that most of them are not highly extinguished, except two objects, OriA-209 and OriA-231, which have A_V greater than 10. Therefore, the overcorrection of extinction of deeply embedded protostars cannot be the major reason for the objects with $n_{5-12} \gtrsim -0.2$ in the Orion sample. Even though these objects lie in the “envelopes” area in Figure 14, we do not classify them as “envelope-dominant” objects.

In order to figure out the differences of classification and sample distribution among star-forming regions, we also plot Taurus and NGC 1333 objects studied in Furlan et al. (2011) and Arnold et al. (2012) in Figure 14. We chose Taurus and NGC 1333 because Taurus is a fiducial region in many studies and NGC 1333 is one of the youngest star-forming regions. In the upper panel of Figure 14 we find that two TDs in Taurus are located in the “envelopes” area and that most of the Taurus objects having large $n_{5-12} (>-0.2)$ have $n_{12-20} > 0$. We also notice that there are many objects distributed in $-2 < n_{12-20} < 2$ in NGC 1333 in the “envelopes” area. To better demonstrate how the Orion sample and Taurus/NGC 1333 samples in the “envelopes” region in Figure 14 are different, we plot n_{12-20} versus n_{K-25} for them in Figure 15. The objects located in the “envelopes” area in Figure 14 are indicated with colored symbols: magenta for the ONC and L1641 and blue for Taurus and NGC 1333. We find that YSOs in our sample of Orion A falling in the “envelope” region as marked in magenta lie in “Class II” by n_{K-25} and “disks” by n_{12-20} , while most Taurus and NGC 1333 objects marked by blue squares are located in the “Class I” or “FS” area in Figure 15.

The classification scheme by n_{5-12} versus n_{12-20} has worked well to reclassify as disks some disk-dominant objects that fall into the Class I region according to n_{K-25} . Conversely, we would like to understand why so many YSOs in Orion A that lie in the “envelopes” region of the n_{5-12} index are classified as Class II based on n_{K-25} . Considering that the Orion sample was selected as exclusively disk candidates from IRAC/2MASS color-color diagrams from Megeath et al. (2012), the possible dominant reason of this different classification is because we have several TDs with a steep rise between 5 and 12 μm but more moderate changes between 12 and 20 μm than envelope

sources. If an object is in an initial stage of inner disk dissipation, it would have little excess around 5 μm , but still a strong excess at longer wavelengths, so its 5–12 μm spectral index would be large and thus in the “envelopes” area, while its K –25 μm index would be more typical of Class II objects.

From the comparison of sample distributions and source classifications done in Figures 13–15, we reaffirm that the disk classification schemes based on spectral indices (n_{K-25} , n_{5-12} , and n_{12-20}) work well as a first classification filter and they are complementary to each other, but one needs to check the SEDs carefully to avoid ambiguous classifications.

4.3.2. Transitional Disks

TDs have radial gap(s) or central holes, so their SEDs are different from the SEDs of radially continuous full disks (FDs). Thus, TDs are distributed in a separate region from the FDs on the spectral index diagrams. We have described how spectral indices and EW10 can be used to find TD candidates in Kim et al. (2013). Here we revisit the selection criteria for TDs that we described previously (Kim et al. 2013): $n_{K-6} \leq -2.1$, $n_{13-31} \geq 0.5$, EW10 ≥ 4.3 . After updating SpT information and adding 16 objects in Orion A Class II disk sources, we recalculate the selection criteria to check whether any significant changes are needed for the thresholds of n_{K-6} , n_{13-31} , and EW10. We find that the lowest 12.5% (octile) of n_{K-6} and the highest 12.5% of EW10 for Class II disks in Ori A, Tau, Cha I, Ophiuchus, and NGC 1333 are very similar to the previous values. The highest 12.5% of n_{13-31} has somewhat noticeably changed from 0.5 to 0.57, but this change is still uncertain and does not affect much the TDs already identified. Therefore, we keep the selection criteria used by Kim et al. (2013). We indicate how TDs are separated from the distribution of FDs in the ONC and L1641 in Figure 16. We identify three more TDs from the 16 Class II disks added in our sample.

There are three subtypes of TDs depending on the disk’s radial structure inferred by the morphology of their SED and self-consistent disk modeling: CTD, PTD, and WTD. CTD is an acronym for “classical TD”—a TD with a central hole. The characteristics of an SED of a CTD is no/negligible disk excess over 2–6 μm and a steep flux increment after 13 μm . A “pre-transitional disk” (PTD) shows a strong disk excess similar to optically thick disk emission in the near-IR, a dip, and redder emission after 13 μm , which is explained with a radial gap between the optically thick inner and outer disk (Espaillat et al. 2007). In case there is weak excess somewhat between that of CTDs and PTDs, the excess may be due to optically thin inner disk emission. We call these TDs “weak-excess TDs” (WTDs). Kim et al. (2013) defined the inner disk excess fraction to

Table 8
Grain Properties

Num.	Mod	EW10 (μm)	σ_{EW10} (μm)	EW20 (μm)	σ_{EW20} (μm)	F10 (10^{-12} erg s $^{-1}$ cm $^{-2}$)	σ_{F10} (10^{-12} erg s $^{-1}$ cm $^{-2}$)	F20 (10^{-12} erg s $^{-1}$ cm $^{-2}$)	σ_{F20} (10^{-12} erg s $^{-1}$ cm $^{-2}$)	$F_{11.3}/F_{9.8}$	$\sigma_{F_{11.3}/F_{9.8}}$	TD/FD
1	SLLL	8.054	0.157	3.243	0.326	2.698	0.022	0.759	0.068	0.45	0.01	TD
2	SLLL	2.781	0.088	2.392	0.305	1.127	0.023	0.553	0.054	0.53	0.02	FD
3	SLLL	2.509	0.085	2.464	0.305	29.600	0.634	9.833	0.893	0.41	0.02	FD
4	SLLL	2.595	0.086	2.533	0.309	3.219	0.075	1.470	0.145	0.44	0.02	FD
5	SLLL	5.348	0.12	2.515	0.308	5.381	0.061	1.491	0.147	0.51	0.02	TD

(This table is available in its entirety in machine-readable form.)

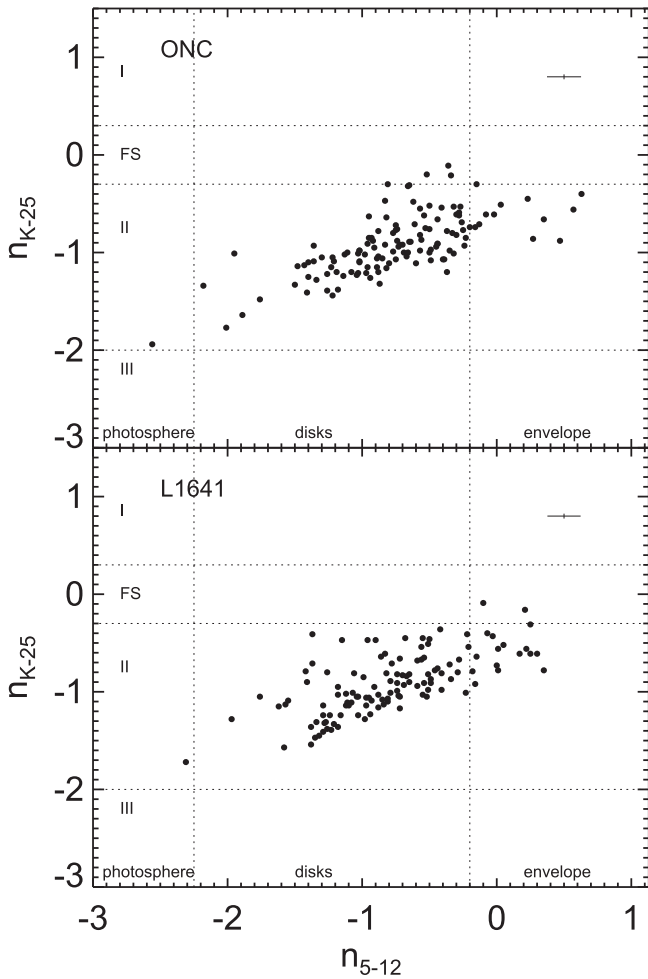


Figure 13. Comparison of the observed spectral indices and disk classification by n_{5-12} vs. n_{K-25} for the ONC (top) and L1641 (bottom). The horizontal dotted lines divide the regions occupied by Class I, FS, Class II, and Class III objects by the n_{K-25} criteria. The vertical dotted lines split the regions into photosphere, disks, and envelope by n_{5-12} . The typical errors are indicated in the top right corner of each panel.

classify three subtypes of TDs from their disk excess in 2–6 μm .

Among three newly identified TDs, OriA-306 and OriA-307 belong to the ONC, and they are subclassified as a PTD and a CTD, respectively. OriA-314 belongs to L1641 and is classified as a WTD. Thus, we have a total of 65 TDs: 34 in the ONC and 31 in L1641.

4.4. Mass Accretion Rates

We observed 120 Class II disks with IRTF/SpeX in SXD mode from 0.8 to 2.4 μm . We utilize $\text{Pa}\gamma$ (1.094 μm), $\text{Pa}\beta$ (1.282 μm), and $\text{Br}\gamma$ (2.166 μm), which are in the wavelength coverage of SpeX SXD spectra, in order to measure mass accretion rates from the hydrogen recombination lines. We start with the dereddened SpeX spectra, with the A_V determined as described in Section 3.2. We obtain mass accretion rates of 113 objects among the 120 observed. The objects excluded from the determination of mass accretion rates are OriA-21, 45, 52, 88, 135, 170, and 266, which are mostly earlier SpT objects with strong hydrogen absorption lines. We also analyze the reduced SpeX spectra of companions of nine objects, OriA-4, 26, 38, 47, 98, 173, 208, 280, and 290. Among them, six

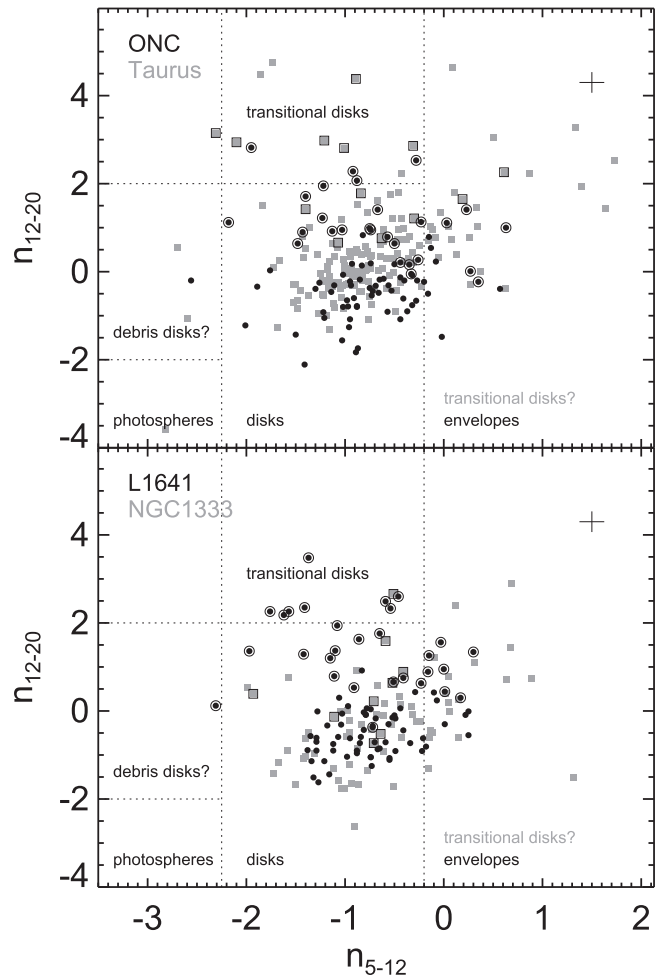


Figure 14. Comparison of the observed spectral indices and disk classification by n_{5-12} vs. n_{12-20} . The vertical dotted lines indicate general division of envelopes, disks, and photospheric objects. Envelopes usually lie at $n_{5-12} \geq -0.2$, disks at $-2.25 \leq n_{5-12} < -0.2$, and photospheres at $n_{5-12} \leq -0.2$. Transitional disks occupy the region of disks in n_{5-12} , but have $n_{12-20} > 2$; a few can also be found at $0 \leq n_{12-20} < 2$ and $n_{5-12} \geq -0.2$. Debris disks have n_{5-12} values of photospheres, but n_{12-20} in the disk range. The upper panel is for objects in the ONC (black circles) and for objects in Taurus (Furlan et al. 2011; gray squares) for comparison. The lower panel is for objects in L1641 (black circles) and for objects in NGC 1333 (Arnold et al. 2012; gray squares) for comparison. TDs classified in Kim et al. (2013) are indicated with larger open circles encompassing the filled circles for the ONC and L1641 and larger open squares encompassing the filled squares for Taurus and NGC 1333. The typical errors are indicated in the top right corner of each panel.

objects show emission of the hydrogen recombination lines, and three companions show absorption lines. We do not include the mass accretion rates of companions in the following analysis due to the lack of information about the companions' properties. In addition, we do not include the mass accretion rate of OriA-208 and OriA-247 in our analysis because they belong to the 10 objects that have incomplete IRS spectra, are variable, and/or are a galaxy as described in Section 3.3. Therefore, we use mass accretion rates of 111 objects in the ONC and L1641 for any analysis related to disk–stellar mass accretion properties in this work.

To get the mass accretion rates from three hydrogen recombination lines, we first fit each hydrogen recombination line with a Gaussian function plus a local continuum to get the line luminosity: $L_{\text{Pa}\gamma}$, $L_{\text{Pa}\beta}$, and $L_{\text{Br}\gamma}$. Then we calculate the accretion luminosity, L_{acc} , from the line luminosity of each

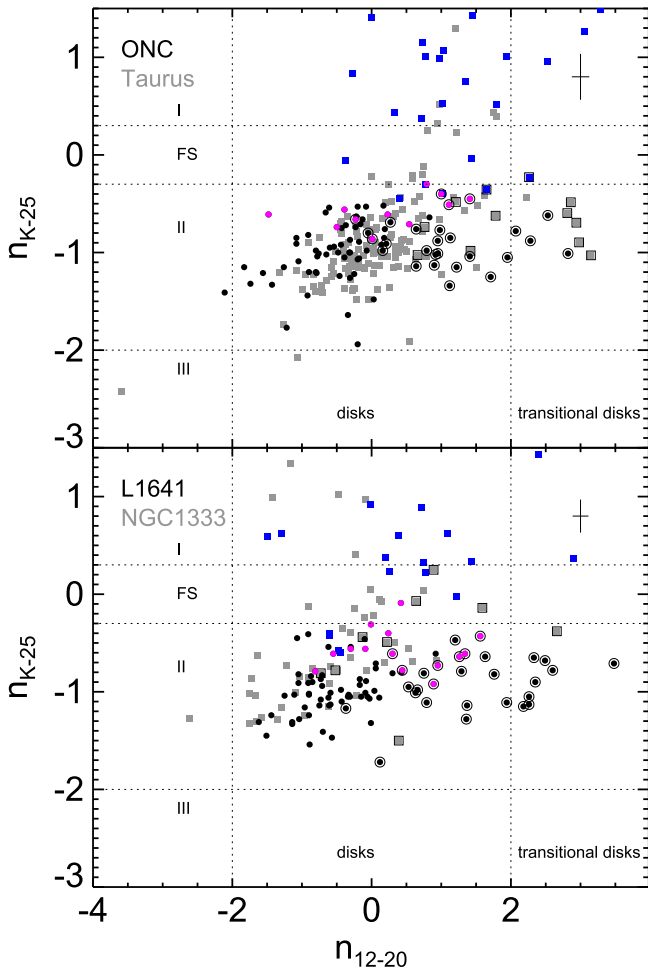


Figure 15. Comparison of the observed spectral indices and disk classification by n_{12-20} vs. n_{K-25} . TDs classified in Kim et al. (2013) are indicated with larger open circles encompassing the filled circles for the ONC and L1641 and larger open squares encompassing the filled squares for Taurus and NGC 1333. The colored symbols (magenta: the ONC and L1641; blue: Taurus and NGC 1333) indicate the objects with $n_{5-12} > -0.2$, which are in the “envelopes” area in Figure 14. The typical errors are indicated in the top right corner of each panel.

hydrogen recombination line. To do so, we adopt the empirical correlations between L_{acc} and L_{line} derived by Muzerolle et al. (1998) for $\text{Pa}\beta$ and $\text{Br}\gamma$ and Gatti et al. (2008) for $\text{Pa}\gamma$ to convert the line luminosity to the accretion luminosity as follows:

$$\log(L_{\text{acc}}/L_{\odot}) = 1.36 \times \log(L_{\text{Pa}\gamma}/L_{\odot}) + 4.1 \quad (5)$$

$$\log(L_{\text{acc}}/L_{\odot}) = 1.14 \times \log(L_{\text{Pa}\beta}/L_{\odot}) + 3.15 \quad (6)$$

$$\log(L_{\text{acc}}/L_{\odot}) = 1.26 \times \log(L_{\text{Br}\gamma}/L_{\odot}) + 4.43. \quad (7)$$

Finally, we obtain the disk–star mass accretion rate, \dot{M} , from the relation

$$\dot{M} = \frac{L_{\text{acc}} R_{\star}}{GM_{\star}}, \quad (8)$$

where R_{\star} and M_{\star} are stellar radius and stellar mass, respectively, which we calculated as described in Section 3.4, and L_{acc} is the accretion luminosity from Equations (5), (6), and (7).

The accretion rate estimates from three recombination lines in our spectra are generally within a factor of 2–3 of each other.

We adopt the average \dot{M} and report it in Table 6. We regard the resulting average \dot{M} as an upper limit when fewer than three lines were observed with poor signal-to-noise ratio or when the fitting of three lines is not reliable due to low signal-to-noise ratio. We adopt the average \dot{M} measured from two lines as a detection for some cases if two lines are prominent.

We find that the distributions of mass accretion rates of Class II objects in the ONC and L1641 are not very different when we include all possible \dot{M} in the distributions, either by visual inspection or by the K-S test (Figure 17). We compare \dot{M} distributions of two subgroups, FDs and TDs, in Figure 18 and check that \dot{M} of TDs are decreased significantly compared to those of FDs. The median values of $\log \dot{M}$ of FDs are -7.81 for the ONC and -7.99 for L1641. For TDs, they are -8.71 and -8.79 for the ONC and L1641, respectively. We confirm that the difference of the median \dot{M} between FDs and TDs in the ONC and L1641 is almost a factor of 10, as seen in the Taurus-Aurigae association by Najita et al. (2007) and their extended study including Ophiuchus (Najita et al. 2015).

We compare the median values of \dot{M} between FDs and TDs in the narrower SpT ranges, $K-M$, K type, M type, and $M3$ or later, to investigate any impact by the \dot{M} dependence on SpTs to the different mass accretion distributions between FDs and TDs because TDs are more weighted to the later types ($K-M$). The number of objects in the $K-M$ group is 56 for FDs and 50 for TDs, which are comparable sizes of samples between the two groups. The median \dot{M} of FDs and TDs for the $K-M$ group are $1.03 \times 10^{-8} M_{\odot} \text{yr}^{-1}$ and $1.76 \times 10^{-9} M_{\odot} \text{yr}^{-1}$, respectively. When we take only K -type objects, the median \dot{M} are $4.54 \times 10^{-8} M_{\odot} \text{yr}^{-1}$ for FDs with 23 objects and $4.77 \times 10^{-9} M_{\odot} \text{yr}^{-1}$ for TDs with 13 objects. We have 33 FDs and 37 TDs in the M -type group, and the median \dot{M} is $3.51 \times 10^{-9} M_{\odot} \text{yr}^{-1}$ and $1.5 \times 10^{-9} M_{\odot} \text{yr}^{-1}$, respectively. For the $M3$ or later types with 11 objects of FDs and 18 objects of TDs, the median values are $1.93 \times 10^{-9} M_{\odot} \text{yr}^{-1}$ and $1.34 \times 10^{-9} M_{\odot} \text{yr}^{-1}$, respectively. We note that the median values of \dot{M} decrease from K through $M/M3$ or later types in both FDs and TDs. We find that the median \dot{M} of the K -type objects for TDs are almost 1 mag lower than that for FDs. Even though the differences of the median \dot{M} between FDs and TDs for the M type and $M3$ or later groups are not as large as seen for the K type, the median values of TDs are lower than the median values of FDs in the corresponding subgroups. Since the numbers of objects in each subgroup divided by the SpT ranges between TDs and FDs are not very different, we confirm that the displacement of the mass accretion rate distribution of TDs from that of FDs seen in Figure 18 is not the result of the intrinsic dependency on the SpT of the mass accretion rates. The median \dot{M} of the subgroups are summarized in Table 9.

5. COMPARISON TO DISKS IN TAURUS

In this section, we compare the distribution of spectral indices of the Orion A Class II samples with those of the Class II sample in Taurus. We first compare, in Section 5.1, the whole sample without classifying sources, whether their disk is radially continuous (FDs) or not (TDs). More detailed comparisons of samples of Orion A and Taurus broken down by radial structures (FDs/TDs) follow in Section 5.2.

Our goal is to provide the measured properties of disks in Orion A, as well as to discern any differences with disks in Taurus. Therefore, results from an exhaustive study of the characteristics of Orion A Class II disks and correlations

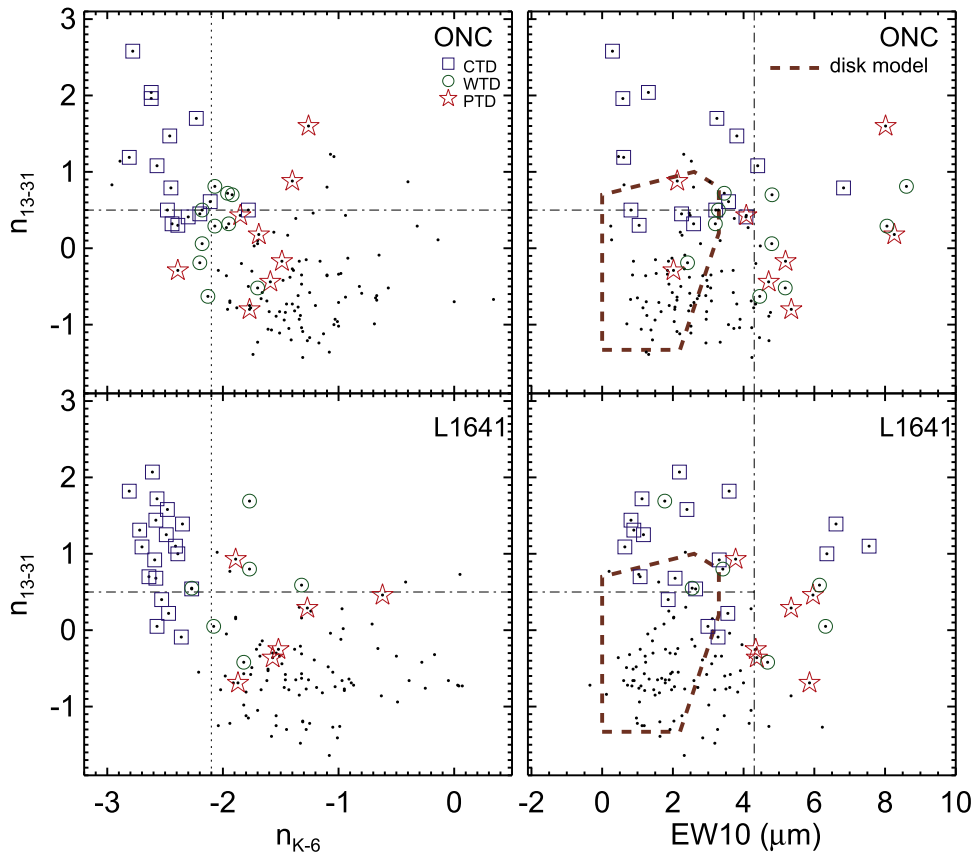


Figure 16. Classification of transitional disks in Orion A, and selection by n_{13-31} vs. n_{K-6} (left panels) and n_{13-31} vs. $EW10$ (right panels). In the right panels, the polygon with a thick dashed brown line indicates the coverage area by a typical accretion disk model (D’Alessio et al. 2006). The upper panels are for the TD selection in the ONC, and the lower panels are for the TD selection in L1641. The dot-dashed lines indicate the upper octile; the dotted lines indicate the lower octile. The blue squares indicate the candidates of CTDs. The green circles are for WTDs, and the red stars indicate PTDs.

between properties will be discussed in the next paper (K. H. Kim et al. 2016b, in preparation). Here, to measure the quantitative difference between the distributions of a given parameter among our subregion (OriA, Trapezium, the ONC, and L1641) and Taurus, we perform a K-S test and measure the median of the property for each group.

We consider a K-S difference D between two groups to be significant if p , the probability that D could result from two random selections from the same distribution, is less than 0.05. If p is less than 0.01, we take the deviation to be highly significant. With small p , the value of D indicates a significant maximum difference between the cumulative distributions. In our data D varies all the way from nearly unity to about 0.1. The largest values indicate completely distinct, nonoverlapping distributions; the smallest values indicate largely overlapping distributions with maximum differences consistent with Poisson statistics and the total numbers in our samples. We rank the significant differences as large ($D > 0.5$), medium ($0.25 \lesssim D \lesssim 0.5$), and small ($D < 0.25$). D and p for all pairs appear along with the histograms in Figures 19–24.

5.1. Index from 5 to 14 μm Spectrum: Trapezium, the ONC, L1641, and Taurus

As we described in Section 2, Class II objects in the Trapezium could only be observed with the SL module (5–14 μm). We show the distributions of n_{K-6} , n_{6-13} , $EW10$,

and $F_{11.3}/F_{9.8}$, which are the properties taken from IRS SL spectra of objects in three subregions of Orion A and Taurus, in Figure 19, without separating objects by their radial structures.

The distributions of n_{K-6} from the disks in the three subregions of Orion A in the upper left panel of Figure 19 show that n_{K-6} of the ONC and L1641 is biased toward higher values than Taurus, even though this difference is not statistically significant.

The upper right panel of Figure 19 shows that the distribution of n_{6-13} in the ONC is shifted to higher values of n_{6-13} compared to Taurus. A K-S test result for the ONC versus Taurus shows that this displacement is statistically highly significant. The n_{6-13} distribution of L1641 also tends to higher values than that of Taurus, but the displacement is not noticeably large.

The distributions of $EW10$ of the three subregions of Orion A in the lower left panel of Figure 19 are all statistically significantly different from that of Taurus: all three are skewed toward larger $EW10$. The $F_{11.3}/F_{9.8}$ distributions of Orion A disks in the lower right panel of Figure 19 show different distributions by subregion of Orion A. Comparing $F_{11.3}/F_{9.8}$ values of the Trapezium, the ONC, and L1641 to those of Taurus, the D values from K-S tests decrease and the p values increase from Trapezium through the ONC to L1641 in the lower right panel. The $F_{11.3}/F_{9.8}$ distribution of the ONC is concentrated around smaller values than that of Taurus. Considering the median age differences of the ONC, L1641,

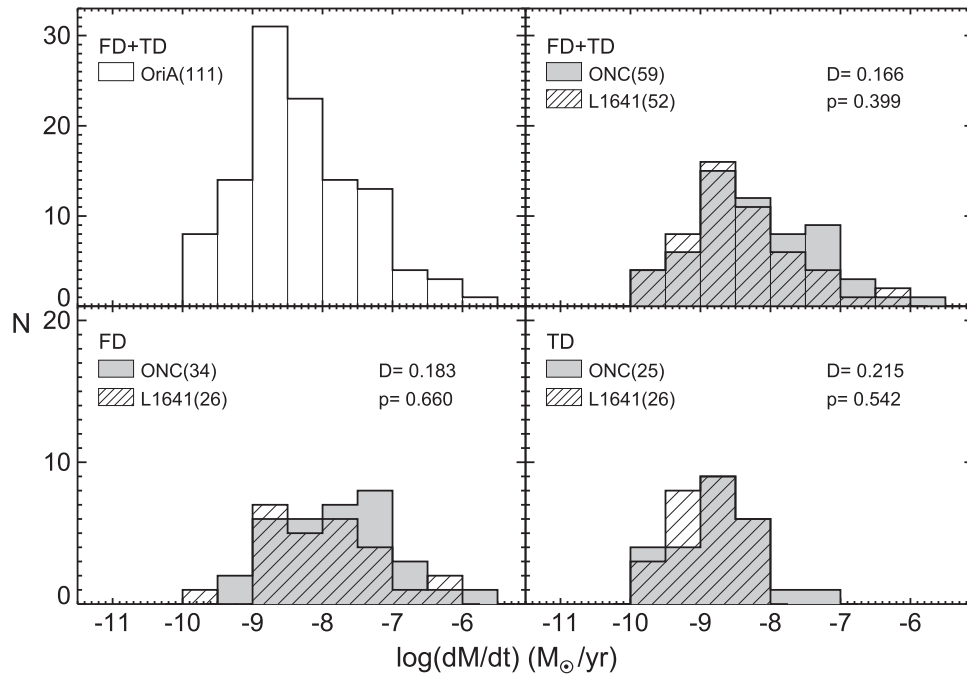


Figure 17. Distribution of \dot{M} . All objects with available \dot{M} in Orion A are in the upper left panel. The upper right panel shows the distributions of \dot{M} of objects in the ONC and L1641. The lower left panel is for the comparison of \dot{M} distribution of FDs in the ONC and L1641. The \dot{M} distribution of TDs in the ONC and L1641 is in the lower right panel. The distribution of \dot{M} is slightly skewed toward the higher value for the ONC, but there is no statistically significant difference in \dot{M} between the ONC and L1641 when the same disk group in two regions is compared. The K-S test results (D and p) are marked in each panel.

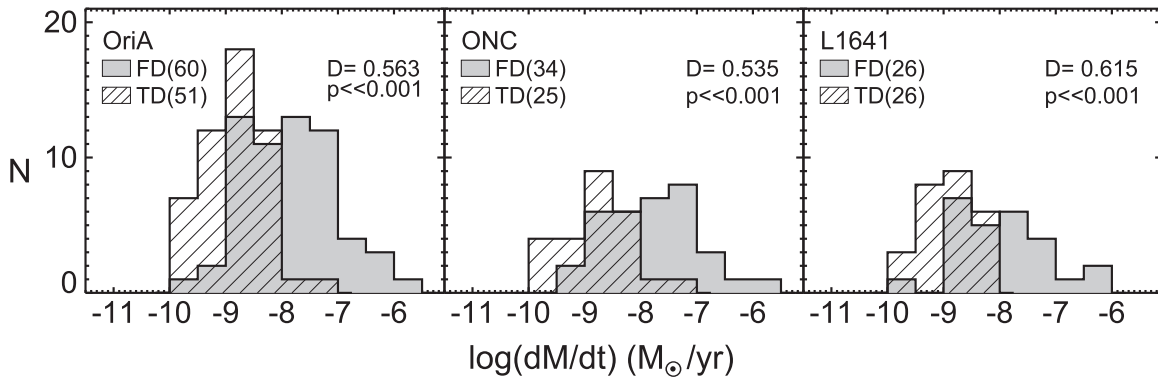


Figure 18. \dot{M} distributions between two groups, FD and TD, are compared in different regions: Orion A (left), the ONC (middle), and L1641 (right). Distributions of \dot{M} are strongly significantly different between FD and TD in all three comparison cases. The K-S test result of each comparison is shown in each panel.

Table 9
Median Mass Accretion Rates: FD vs. TD

Group	Parameters	Subgroups by Spectral Ranges			
		$K-M$	K	M	M3 and Later
FD	N	56	23	33	11
	\dot{M}	10.3	45.4	3.51	1.93
TD	N	50	13	37	18
	\dot{M}	1.76	4.77	1.50	1.34

Note. N is the number of objects. The units of \dot{M} are $10^{-9} M_{\odot} \text{ yr}^{-1}$.

and Taurus, we may infer that the $F_{11.3}/F_{9.8}$ distribution difference between the ONC and Taurus and the smaller—probably insignificant—difference between L1641 and Taurus indicate increased processing of dust as time goes on.

On the other hand, despite lots of arguments in ages, the young stars in the Trapezium (i.e., the center of the ONC) are probably somewhat younger (Getman et al. 2014; Megeath et al. 2016) than the rest of the ONC, L1641, and Taurus, but its $F_{11.3}/F_{9.8}$ distribution is broad and skewed toward higher values than that of Taurus. This large shape difference between Trapezium and Taurus, which goes in the direction of larger degrees of dust processing, is possibly a disk-evolutionary difference rather than a dust-evolutionary difference: less processed material at somewhat larger radii, which is still warm enough to contribute significantly to the $10 \mu\text{m}$ silicate feature, may have been selectively removed from the systems, by radiation from the Trapezium O/B-type stars. We discuss the outer disk evolution in Trapezium in detail in Section 6. We also compare subdivisions of $F_{11.3}/F_{9.8}$ distribution separated by the disk radial structures in the following subsection.

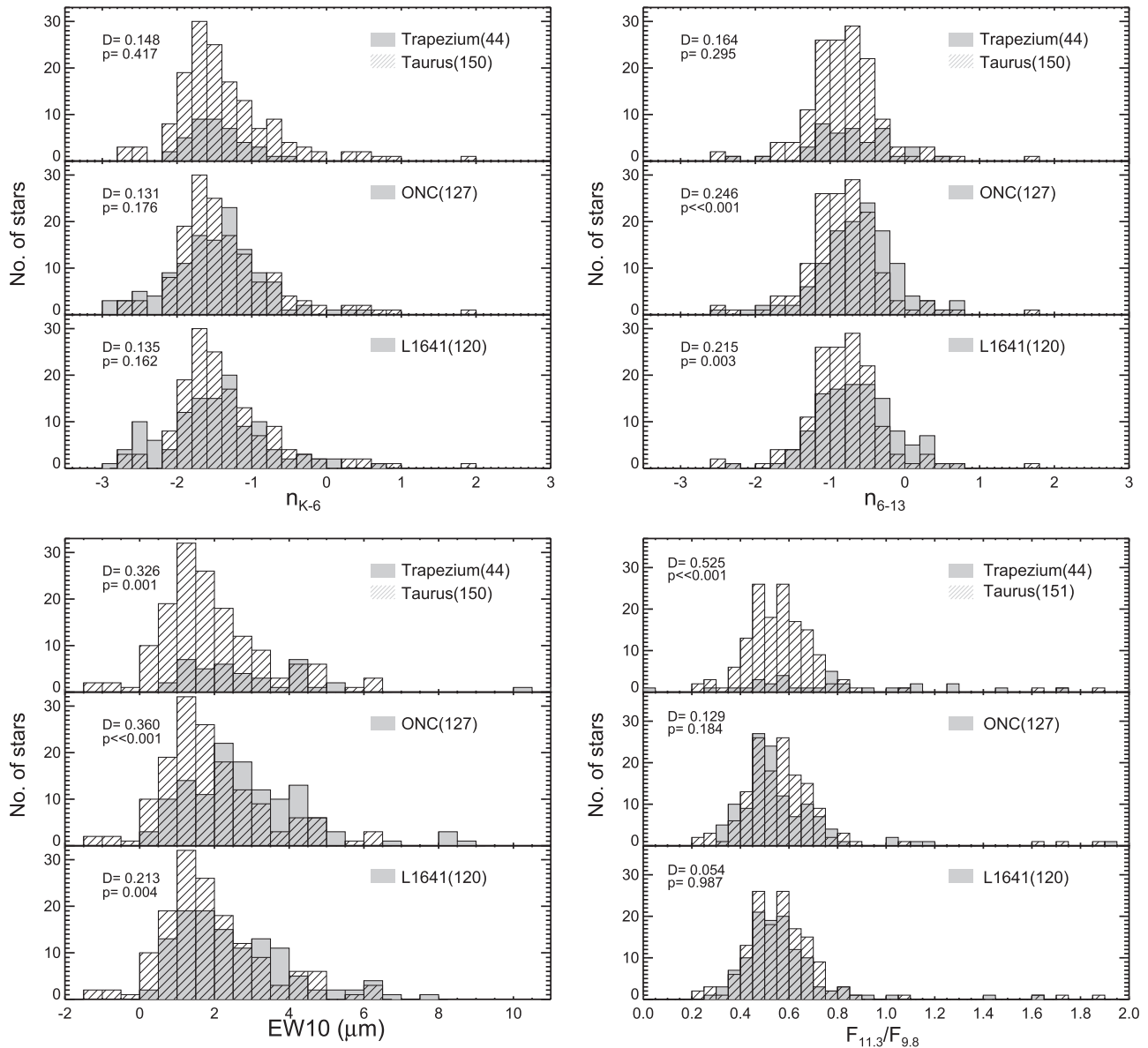


Figure 19. Histogram comparison of disk and dust properties measured from SL spectra. We include disks having n_{K-6} (upper left), n_{6-13} (upper right), EW10 (lower left), and $F_{11.3}/F_{9.8}$ (lower right) without separating the samples by their radial structures, FDs or TDs. We compare the distribution of each property in this figure in three subregions of Orion A (Trapezium, the ONC, and L1641) with that of Taurus. The K-S test result of each comparison is shown in each panel.

5.2. Disk and Dust Processing Indicators from Full IRS Spectra: The ONC, L1641, and Taurus

Now, we consider the properties of Class II samples in the ONC and L1641 observed with the full IRS spectrum, 5–37 μm . Here we look into how the distributions of disk and dust properties are different not only by the star-forming region among the ONC, L1641, and Taurus but also by the radial structure of disks between TDs and FDs. We compare the distributions of n_{K-6} , n_{6-13} , n_{13-31} , EW10, and $F_{11.3}/F_{9.8}$. A caveat concerning the comparison of the grouped subsamples in Orion A and Taurus is the small sample size of TDs in Taurus. The K-S test is a powerful two-sample nonparametric test that is reliable even for small-number samples (<10; Wall & Jenkins 2003). Therefore, we perform the K-S test for the subsamples and discuss their similarities or differences based on the performance. The output from the

statistical tests, median, and D and p from the K-S test are listed in Table 10.

We find that the distributions of TDs in Orion A or the subsets by the regions, the ONC and L1641, are not much different from the distributions of TDs in Taurus for the properties n_{K-6} , n_{6-13} , EW10, $F_{11.3}/F_{9.8}$, and n_{13-31} , by checking through histograms in the lower panels of Figures 20–24.

In the case of FDs, we notice that the properties of FDs in Orion A tend to have higher values than that in Taurus, in general, except n_{13-31} and $F_{11.3}/F_{9.8}$. Even though D is not large in both cases of OriA-Tau and L1641-Tau, D values are larger in the case of the ONC-Tau comparison of FDs than in the case of the L1641-Tau comparison, and p values indicate that the differences between the ONC and Taurus are significant for n_{K-6} , n_{6-13} , and EW10.

Table 10
Distribution of Properties and Comparison with Taurus: FD and TD

Group	Parameter	Taurus Median	K-S Test								
			Ori A			ONC			L1641		
			Median	D	p	Median	D	p	Median	D	p
FD	n_{K-6}	-1.49	-1.33	0.17	0.02	-1.33	0.20	0.02	-1.33	0.14	0.22
	n_{6-13}	-0.87	-0.64	0.22	<0.01	-0.61	0.25	<0.01	-0.64	0.22	0.01
	n_{13-31}	-0.54	-0.66	0.16	0.03	-0.67	0.16	0.09	-0.66	0.16	0.10
	EW(10 μm)	1.56	2.21	0.28	<0.01	2.47	0.38	<0.01	1.98	0.21	0.02
	$F_{11.3}/F_{9.8}$	0.55	0.52	0.13	0.11	0.52	0.16	0.10	0.53	0.12	0.38
TD	n_{K-6}	-1.89	-2.23	0.30	0.23	-2.18	0.31	0.27	-2.39	0.34	0.20
	n_{6-13}	-0.75	-0.52	0.18	0.85	-0.47	0.22	0.71	-0.62	0.14	0.99
	n_{13-31}	0.71	0.59	0.23	0.56	0.50	0.28	0.40	0.70	0.24	0.59
	EW(10 μm)	4.67	3.45	0.43	0.03	3.57	0.38	0.11	3.31	0.48	0.02
	$F_{11.3}/F_{9.8}$	0.50	0.57	0.27	0.35	0.54	0.19	0.85	0.60	0.36	0.15

Note. D is the maximum deviation between the cumulative distribution of two groups. p indicates the probability that there is no significant difference between the distributions.

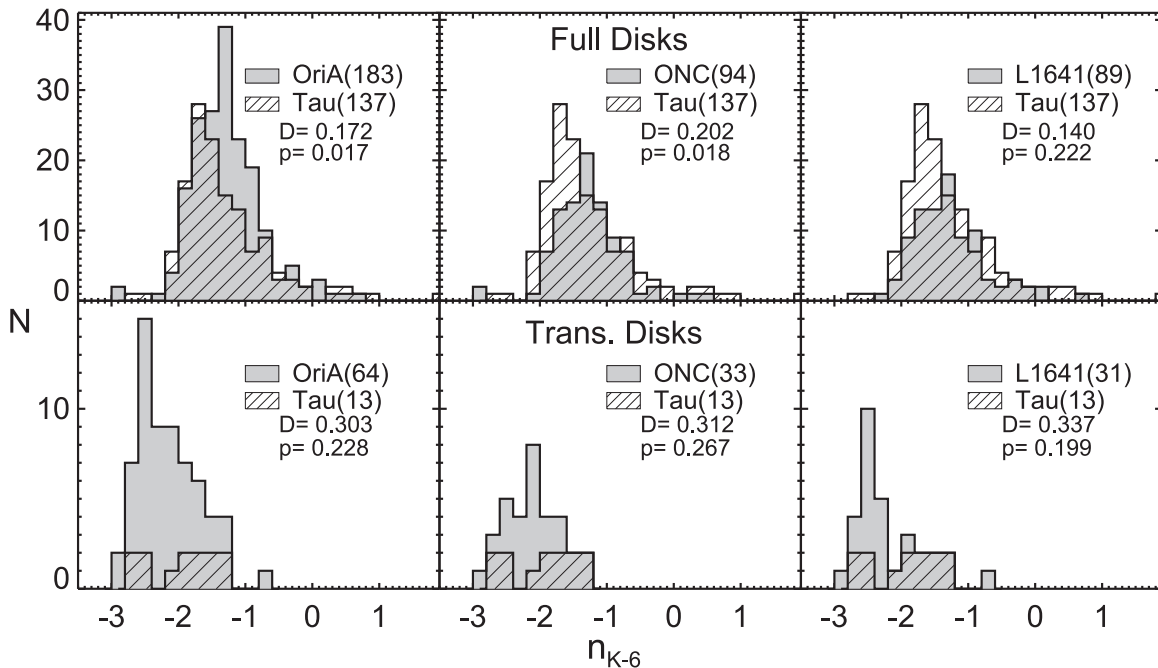


Figure 20. Comparison of n_{K-6} between Orion A (solid) and Taurus (hatched). The objects in the sample are separated by their radial structure, FDs or TDs (upper panels or lower panels), and by the subregions, OriA, the ONC, or L1641 (left, middle, or right panels). The K-S test result of each comparison is shown in each panel.

The spectral index, n_{K-6} in Figure 20, and n_{6-13} in Figure 21 are measures of the optically thick disk continuum structure in the inner radius of a disk. EW10 in Figure 22 is related to the optically thin small dust grains. Therefore, we can infer that disks in the ONC are less processed and still have more flared disks and more small grains in vertically optically thin regions than disks in Taurus. The inner disks in L1641 seem to be more processed than disks in the ONC and less processed than those in Taurus because their n_{K-6} , n_{6-13} , and EW10 are distributed somewhat in the middle of the ONC and Taurus.

Among the properties compared here, EW10 of FDs between the ONC and Taurus shows the most significant and largest difference. EW10 measures amounts of small dust relative to the underlying dust continuum. From the higher EW10, in spite of higher n_{K-6} and n_{6-13} indicating less continuum depletion in the ONC, we infer large amounts of small dust in optically thin regions in disks of the ONC.

We look into the distribution of $F_{11.3}/F_{9.8}$ to learn more about dust properties in Figure 23. The results from the K-S test for $F_{11.3}/F_{9.8}$ do not support any significantly different distribution between disks in Orion A and disks in Taurus, at a first glance. However, we note the peak and median shift of $F_{11.3}/F_{9.8}$ of FDs: the ONC has the smallest median; L1641 has a median larger than that of the ONC, but it is smaller than Taurus. These median shifts in $F_{11.3}/F_{9.8}$ along the median ages of star-forming regions may be a clue regarding dust evolution (e.g., growth/crystallization). When we extend our analysis to include the star-forming regions, NGC 1333 and Chamaeleon I, we observe an interesting evolution of $F_{11.3}/F_{9.8}$ along the median age of star-forming regions: 0.5 (NGC 1333), 0.52 (the ONC), 0.53 (L1641), 0.55 (Taurus), 0.59 (Chamaeleon I). However, the dust evolution is very complicated, and a detailed analysis to understand it is beyond the scope of this work.

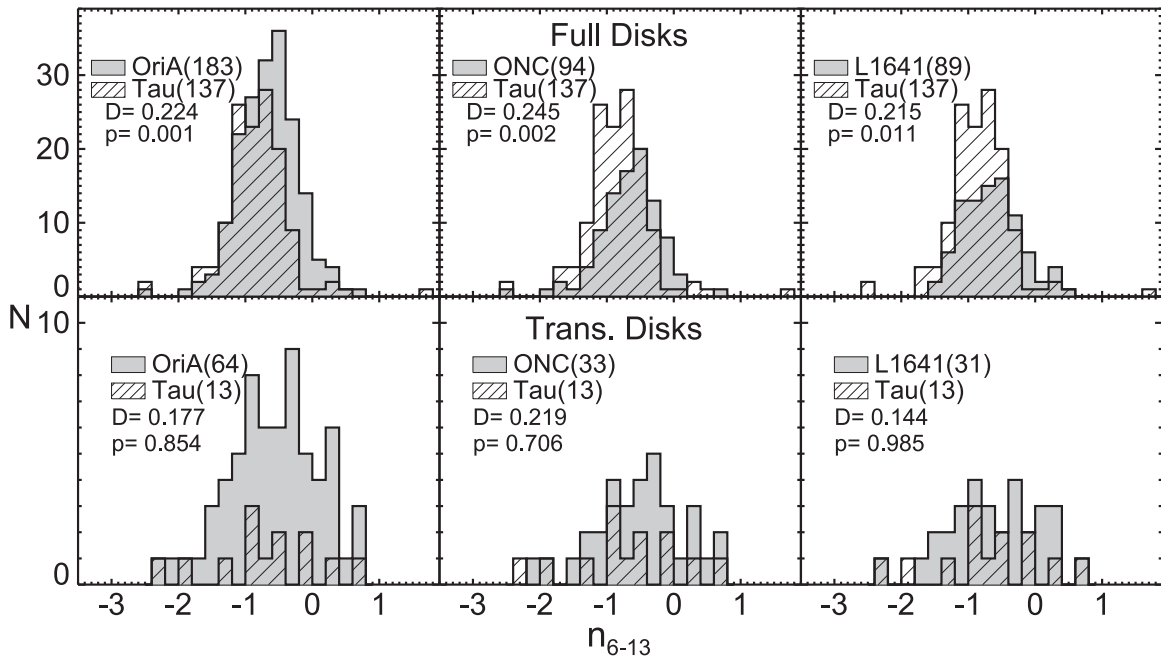


Figure 21. Comparison of n_{6-13} between Orion A (solid) and Taurus (hatched). The objects in the sample are separated by their radial structure, FDs or TDs (upper panels or lower panels), and by the subregions, OriA, the ONC, or L1641 (left, middle, or right panels). The K-S test result of each comparison is shown in each panel.

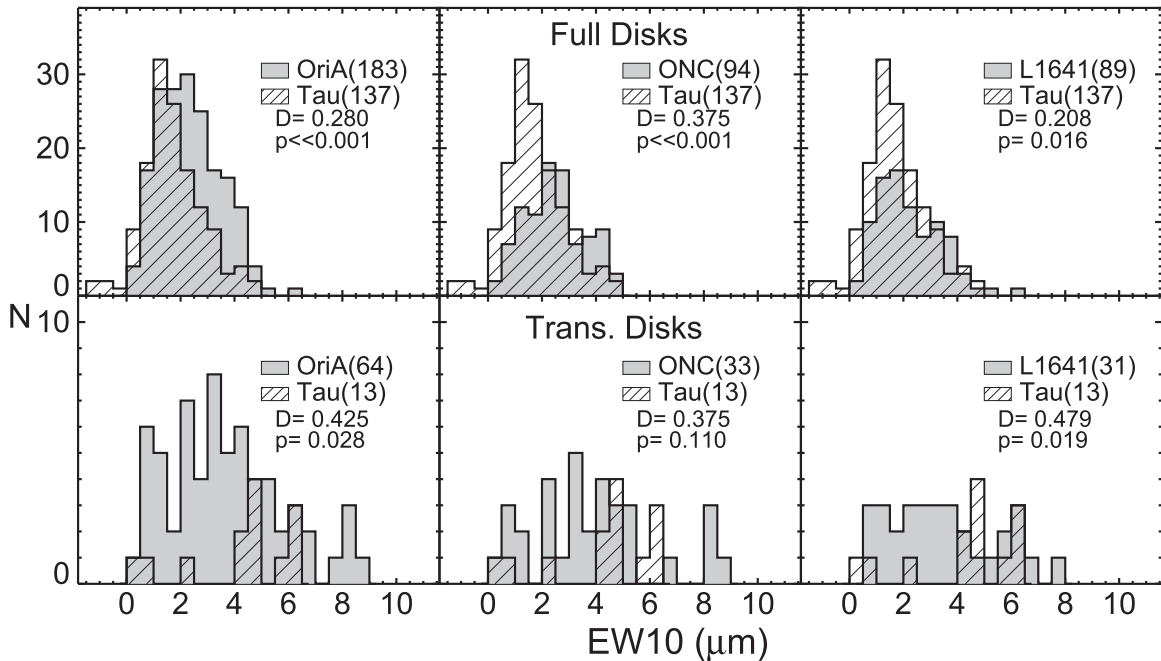


Figure 22. Comparison of EW10 between Orion A (solid) and Taurus (hatched). The objects in the sample are separated by their radial structure, FDs or TDs (upper panels or lower panels), and by the subregions, OriA, the ONC, or L1641 (left, middle, or right panels). The K-S test result of each comparison is shown in each panel.

In contrast to the comparison of the inner disk and grain processing indicators, the comparisons of the distribution of n_{13-31} of the ONC, L1641, and Taurus do not show significant differences (Figure 24). This index is sensitive to the degree of sedimentation in the outer disk (e.g., Furlan et al. 2006); thus, we find no difference in the settling of dust to the disk midplane among these three regions.

Combining our findings from the distributions of n_{K-6} , n_{6-13} , n_{13-31} , EW10, and $F_{11.3}/F_{9.8}$, we suggest that the inner disk evolves faster than the outer disk and dust grain processing (growth and/or crystallization) occurs faster with inner disk

evolution, while the outer disk is less processed and sedimented at 1–3 Myr old.

5.3. Median Spectra

Analysis with a median SED gives a general insight on how the protoplanetary disks in a star-forming region evolve. D’Alessio et al. (1999) applied a median T Tauri star SED to compare their disk models and observational data of T Tauri stars in Taurus. Their choice of a median SED was with K5–M2 stars in Kenyon & Hartmann (1995) because the majority

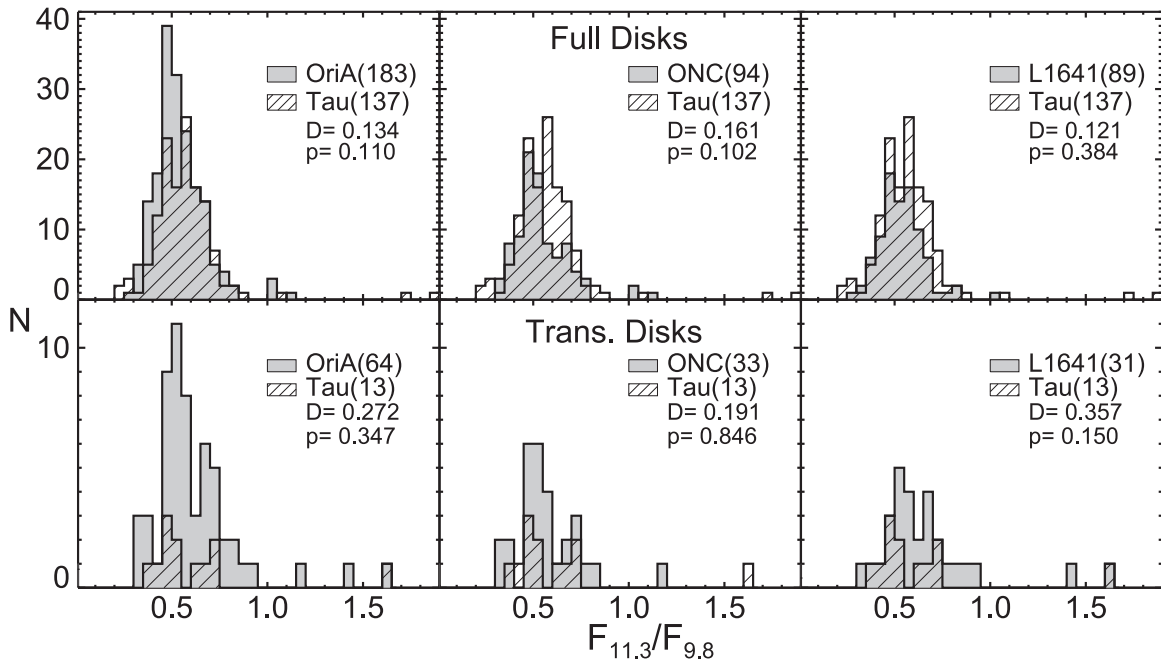


Figure 23. Comparison of $F_{11.3}/F_{9.8}$ between Orion A (solid) and Taurus (hatched). The objects in the sample are separated by their radial structure, FDs or TDs (upper panels or lower panels), and by the subregions, OriA, the ONC, or L1641 (left, middle, or right panels). The K-S test result of each comparison is shown in each panel.

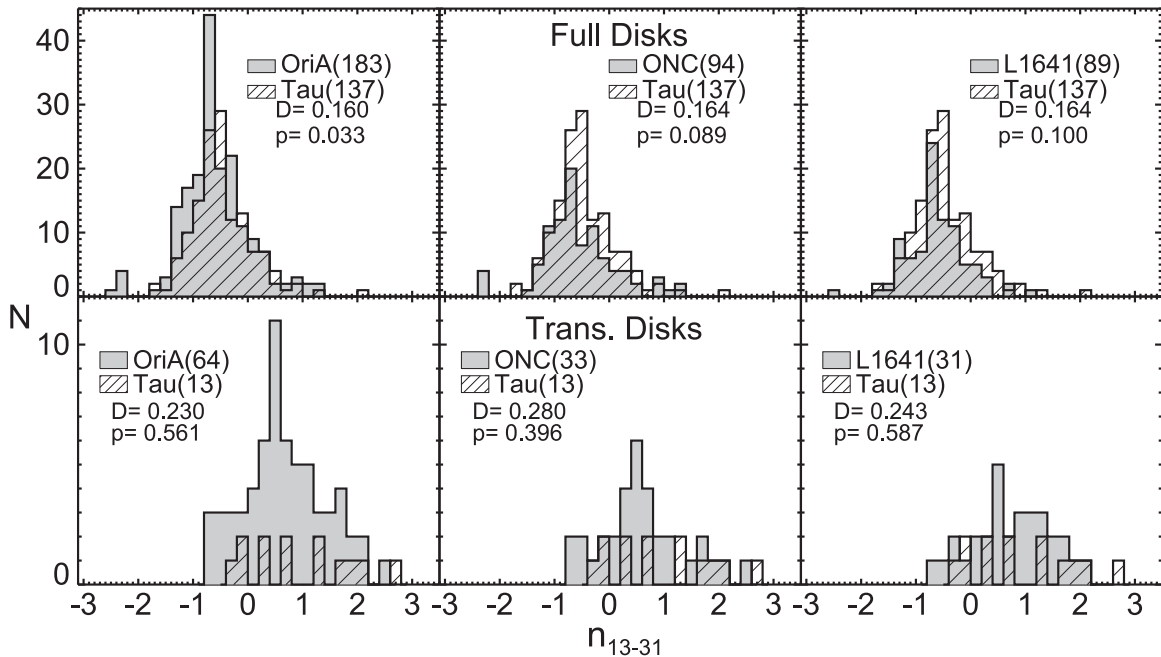


Figure 24. Comparison of n_{13-31} between Orion A (solid) and Taurus (hatched). The objects in the sample are separated by their radial structure, FDs or TDs (upper panels or lower panels), and by the subregions, OriA, the ONC, or L1641 (left, middle, or right panels). The K-S test result of each comparison is shown in each panel.

of SpTs of the disk sample in Taurus lie in SpTs of K5–M2 and the selection of narrow SpT ranges can reduce the large variation in fluxes by restricting the range of stellar effective temperatures (D’Alessio et al. 1999). In this vein, Furlan et al. (2006) generated a K5–M2 median spectrum in the 5–36 μm range with the available IRS spectra of Class II disks in Taurus. After assembling a more complete sample of disks in Taurus, Furlan et al. (2011) updated the K5–M2 median spectrum of Taurus disks. They were also able to generate median spectra of M3–M5 and M6–M9 with a large number of samples. The

analysis with the median IRS spectra of Class II disks observed in nearby star-forming regions is a broadly adopted method to evaluate generally the evolutionary state of disks by comparing median SEDs from region to region (Furlan et al. 2006, 2009, 2011; McClure et al. 2010; Manoj et al. 2011; Arnold et al. 2012). Especially the Taurus K5–M2 median has been widely used as a fiducial reference to examine the status of disk evolution in many other works (e.g., Fang et al. 2013).

Therefore, in order to figure out the general state of evolution of Class II disks in the ONC and L1641, we generate the

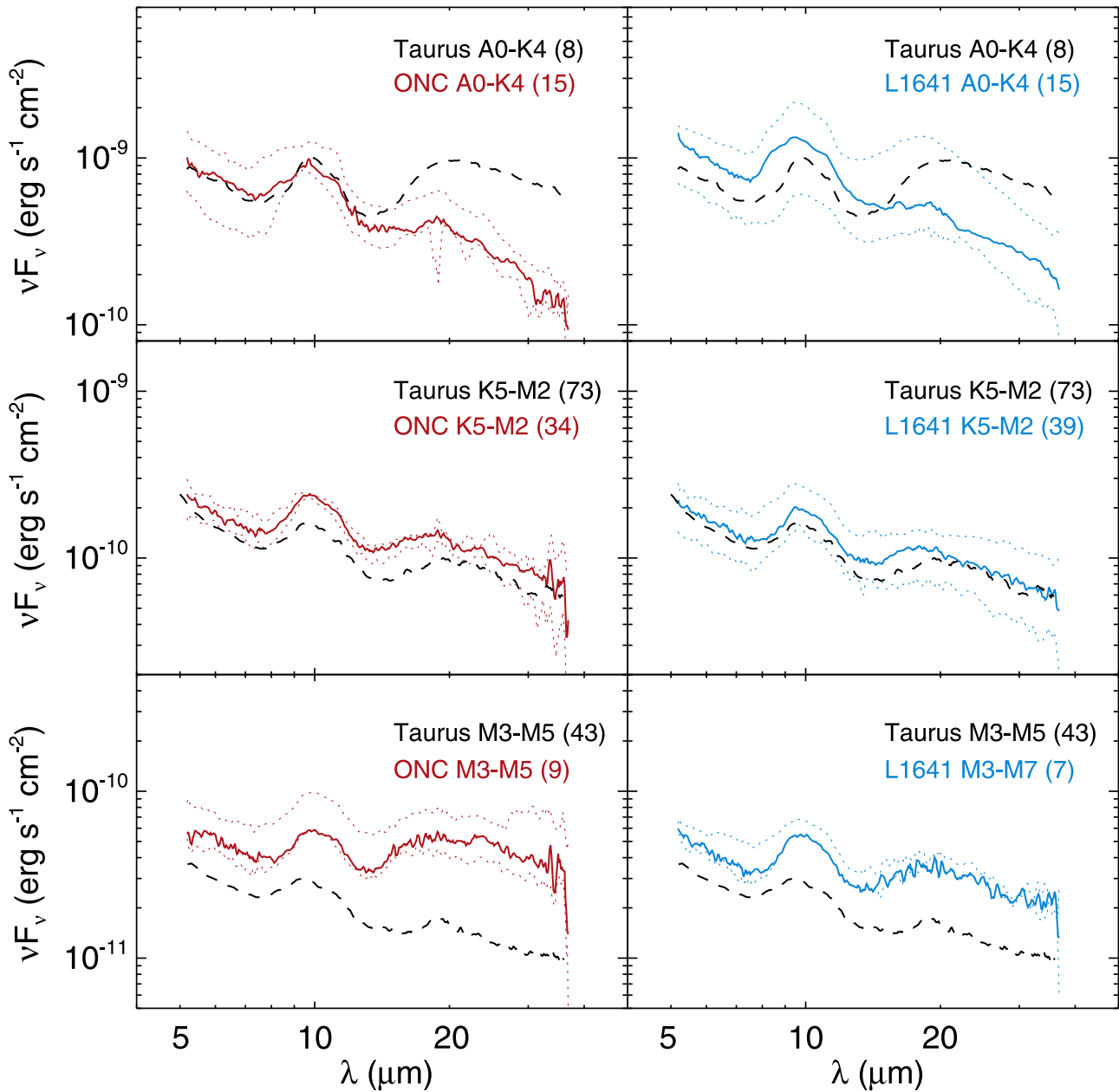


Figure 25. Median spectra of FDs in Orion A, separated by subregions and SpT ranges. They are compared with Taurus median spectra. The number of objects used to generate a median spectrum is indicated next to the sign of SpT range in each panel. The solid lines are the ONC median (left panels) and the L1641 median (right panels), and the dotted lines in each panel indicate upper and lower quartiles. The dashed lines are for the Taurus median indicated in each panel. The ONC median spectra and L1641 median spectra are normalized to the 2MASS *H*-band median flux of the Taurus median spectra in each spectral range.

median spectra of disks in the ONC and L1641 and compare them with the median spectrum of Class II disks in Taurus taken from Furlan et al. (2011). To generate median spectra, we first select the spectra of disks that do not show evidence of time variability or evidence for a radial gap or central hole. We exclude the spectra without host-star SpT information in the selection for a median. Then, we group the spectra into three SpT ranges: A0–K4, K5–M2, and M3–M5(M7). We made the group of K5–M2 because it is a prevailing selection as explained in the previous paragraph. To compare with the median SED of M3–M5 of Taurus, we calculated a median SED of the ONC and L1641 with objects having SpT of M3 or later than M3. The SpTs of all objects used for the ONC median lie between M3 and M5. We include one M7.5 object to generate the L1641 median because the number of L1641

objects in the SpT ranges (M3 or later) is small. The A0–K4 group has not been used previously with the Taurus sample due to the broad range of SpTs and low fraction of objects belonging to the group. Even though we hold a similar limitation to calculate A0–K4 median SEDs with the Orion A sample, we created the group with A0–K4 objects to check the evolution situation of objects with SpTs earlier than K5 because we have frequently noticed diminishing fluxes in longer wavelength from objects with earlier SpTs in the Orion A sample.

With three separated groups, we first normalized the *H*-band flux of each spectrum in each category to the median *H*-band flux of the corresponding group, and then we calculated the median flux at individual wavelengths, as described in D’Alessio et al. (1999), to minimize the effect of different

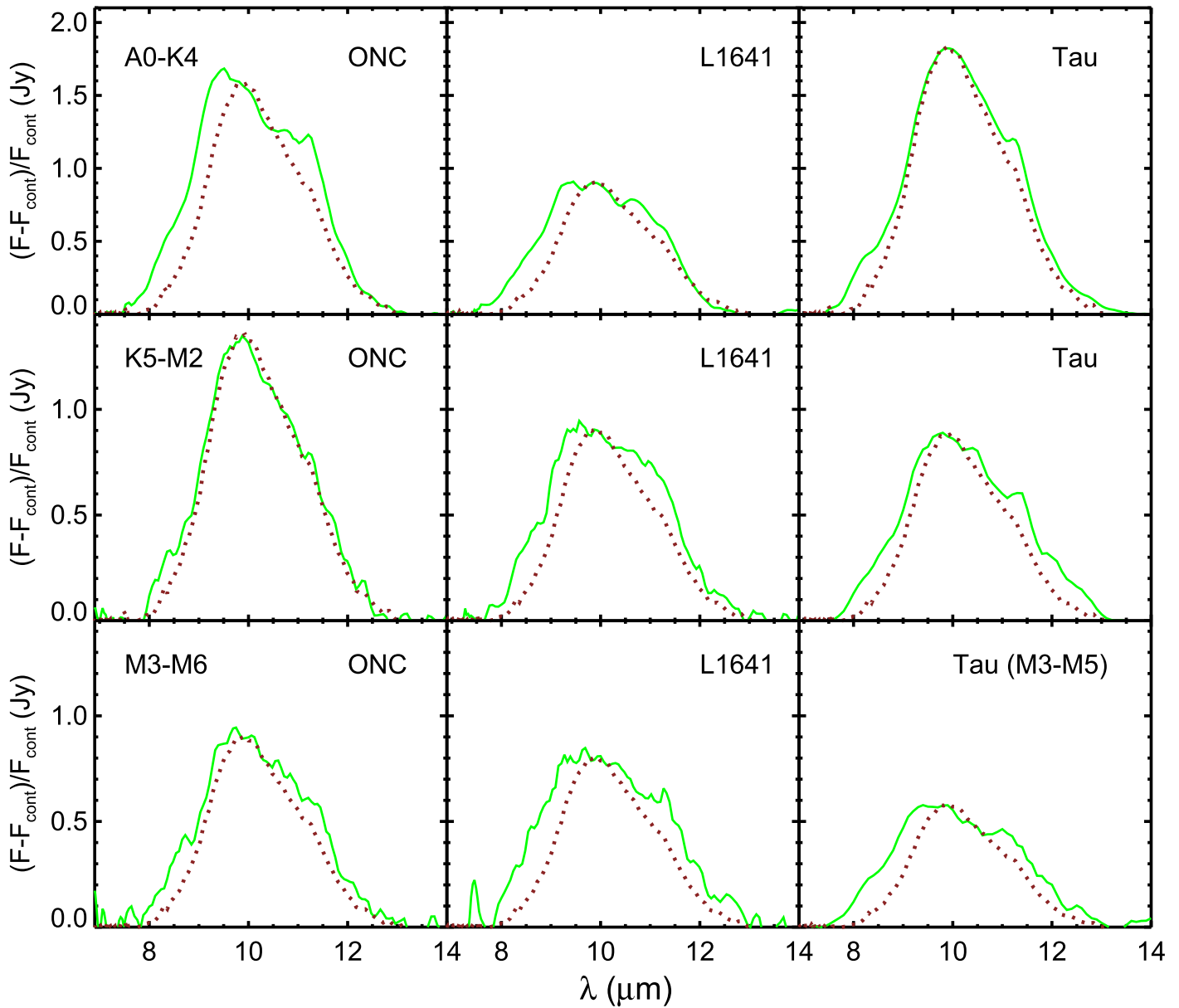


Figure 26. Comparison of continuum-subtracted and continuum-normalized $10\ \mu\text{m}$ silicate feature of median spectra (solid lines) with the pristine silicate feature (dotted lines). The pristine silicate profile is derived by averaging ISM-like reference spectra of LkCa 15 and GM Aur (Sargent et al. 2009; Watson et al. 2009) after subtracting continuum and dividing it with continuum. The pristine silicate profiles are scaled to match to each median silicate profile at $9.8\ \mu\text{m}$.

stellar luminosities in a given group. The displayed median spectra in Figure 25 were normalized to the corresponding median H -band flux of Taurus disks in each panel for the comparison with the median spectrum of Taurus. In Figure 25, the Taurus median spectra of K5–M2 and M3–M5 are adopted from Furlan et al. (2011). The Taurus median of A0–K4 is what we calculated in the same manner applied for other median spectra in order to compare with the median spectra of the ONC and L1641.

In the top panels of Figure 25, the median of the A0–K4 group for the ONC and L1641 differs noticeably from the median spectrum of Taurus. The median spectrum of the A0–K4 group in the ONC has slightly higher flux levels of disk emission than the A0–M4 median spectrum of Taurus over the wavelength range of SL coverage, but the ONC median spectrum shows steeply decreasing fluxes beyond $13\ \mu\text{m}$ with prominent crystalline-silicate features. The median spectrum of

the A0–K4 group in L1641 has high fluxes compared to the A0–K4 median of Taurus over the wavelengths of IRS SL spectral coverage, similarly to the case of the ONC median with stronger excess at 5 – $13\ \mu\text{m}$, and the L1641 median spectrum also shows lower flux in LL coverage compared to that of Taurus. We also note that the flux level of the L1641 A0–K4 median is higher than the ONC A0–K4 median. There are several possible causes contributing to the steep SEDs beyond $13\ \mu\text{m}$: disk settling as grains grow and settle toward midplane, outer disk truncation by the gravitational effect of companions, and ablation of the disk atmosphere by the strong external radiation from nearby OB stars. The objects contributing to the A0–K4 ONC median are OriA-3, 21, 35, 36, 40, 45, 112, 117, 125, 131, 135, 141, 170, 173, and 205. For the A0–K4 L1641 median, the contributing objects are OriA-191, 196, 199, 201, 224, 225, 226, 235, 236, 262, 266, 269, 280, 284, and 295. Among them, OriA-45 and OriA-

Table 11
 n_{20-31} and the Projected Distance (d) from θ^1 Ori C

Num.	n_{20-31}	$\sigma_{n_{20-31}}$	d (arcsec)	d (pc)	Section
1	-0.31	0.43	1075.8	2.2	DN
2	0.37	0.3	1103.5	2.2	DN
3	-1.31	0.1	966.8	1.9	CS
4	-0.82	0.21	2607.3	5.2	L
5	-1.12	0.17	1164.1	2.3	DS

Note. The region for each section is indicated in Figure 1. L indicates L1641 in Figure 2.

(This table is available in its entirety in machine-readable form.)

205 are reported as a double-lined and a single-lined SB, respectively. We also discussed that OriA-125 is a potential binary system from our SpeX observation as we discussed in Section 2. OriA-280 has a very close neighbor based on the SpeX observation, too. Even though there is still a lack of complete multiplicity information for objects in Orion, we can speculate that it is not rare that the outer disk truncation happens around A0–K4 host stars due to the gravitational effect by neighbor sources in the ONC and L1641. Again, a caveat of the A0–K4 median spectra comparison is that the SpT range for A0–K4 median is very broad compared to the K5–M2 and M3–M5(M7) median spectra. However, the fractions of non-K-type objects used for A0–K4 median for the ONC and L1641 are 40%, which is comparable to 37.5% of that for Taurus. Therefore, we consider that the samples for A0–K4 median spectra of the ONC, L1641, and Taurus are still comparable, even though the median spectra do not represent the disk properties in a narrow SpT range.

We compare the median spectra of the K5–M2 groups of the ONC, L1641, and Taurus in the middle panels of Figure 25. In the case of the ONC versus Taurus, the median spectrum from ONC disks has more excess over 5–35 μm , which indicates less evolution of the inner disk and less depletion of small (micron-sized) grains than that of Taurus. We notice that fluxes of 50% of objects used for the K5–M2 ONC median are higher than the Taurus K5–M2 median by examining the quartiles indicated with the dotted lines in the panel. On the other hand, the K5–M2 median spectra of L1641 and Taurus are generally similar. Even though some details like grain properties may show somewhat different characteristics, the general degree of dust settling between Class II disks with K5–M2 SpTs in L1641 and Taurus appears to be similar. The quartiles indicated in the plot with the L1641 K5–M2 median support it.

The bottom row in Figure 25 contains the comparison of the M3–M5(M7) median spectra. Due to the small numbers in the group, we included the spectra of M3 and later than M3 to compare to the M3–M5 median of Taurus. In both L1641 and the ONC, the M3–M5(M7) median spectra appear to have higher excess emission than Taurus. A possible explanation of this higher emission of disks around host stars of M3 or later SpT in Orion A is the younger ages of the systems with M3 or later SpTs in Orion A, resulting in less time for disk evolution than the systems in Taurus. Alternatively, the M3–M5(M7) systems in Orion could have had larger initial disk masses than systems with later SpT in Taurus. We will discuss the M3–M5 median in a future paper, until such time as a complete survey of Orion A including faint objects is carried out.

In Figure 26 we compare 10 μm silicate features of the A0–K4, K5–M2, and M3–M5(M7) medians of our targets and

Taurus with the pristine, ISM-like, silicate feature that is generated from LkCa 15 and GM Aur. LkCa 15 and GM Aur are protoplanetary disks, and they are transitional disks (Calvet et al. 2005) in Taurus and have silicate features that are most similar to those of ISM dust grains (Sargent et al. 2009; Watson et al. 2009). In the figure we plot the continuum-subtracted and continuum-normalized flux. From that, we can check how the silicate feature strength varies from median to median and how the feature shape differs from median to median. The profile of the 10 μm silicate feature of the K5–M2 median of the ONC is very close to the profile of the pristine silicate feature. However, the profile of L1641 for the K5–M2 median is broader than the width of the profile of the pristine silicate feature, and the height is also decreased compared to that of the K5–M2 median of the ONC. This indicates that grains grow, and there are smaller amounts of small dust grains compared to the ONC. The K5–M2 median profile shape of L1641 is similar to that of Taurus, even though detailed features and dust compositions might be different. For the M3 and later SpTs, we also see a somewhat similar pattern of profile changes in the case of K5–M2: the median profiles become broader from the ONC to Taurus. However, we suspect a greater degree of dust processing in the M3–M5 median for the ONC, because the M3–M5 profile of the ONC is neither as smooth nor as narrow as the pristine profile or the K5–M2 profile of the ONC. We notice also that the flatness of the median profile of M3 and later types is increased from the ONC toward Taurus, which supports our finding of the evolution trend of $F_{11.3}/F_{9.8}$ as we discussed before. On the other hand, for the K4 and earlier SpTs, the continuum-subtracted and continuum-normalized 10 μm silicate feature looks more evolved for the ONC and L1641 than Taurus. As we have seen and discussed in the median comparison in Figure 25, the faster outer disk evolution by dynamical effects and photoevaporative effects in Orion environments, if they are dominant and effective, seems to affect the dust processing in the inner disk and disk surface area that gives rise to the 10 μm silicate emission feature and the 10 μm features to show evidence of more processed dust.

Shuping et al. (2006) discuss the significant degree of grain processing by the UV radiation field of θ^1 Ori C in the 10 μm silicate feature of eight proplyds in the vicinity (<30 arcsec) of θ^1 Ori C. We looked up the SpTs of the proplyds in Shuping et al. (2006) and found that only four objects have known SpT information. Three objects have SpTs of early K and one with M type. It looks like our experiments with K5–M2 and M3 later SpTs show the opposite results if we consider only the distance from θ^1 Ori C. However, there is an obstacle in comparing our results directly with their result. The objects in Shuping et al. (2006) are located in much harsher environments (<0.1 pc from θ^1 Ori C), while our objects are located farther than 0.7 pc from θ^1 Ori C. Even though it is difficult to make a clear comparison between our findings regarding silicate dust processing in the A0–K4 median spectra in the ONC/L1641 and results from Shuping et al. (2006) due to the limited information, we speculate that there are similar causes of dust processing in the inner disk regions of the objects, which shows evidence of outer disk dissipation, i.e., the flux reduction at longer wavelengths suffered by proplyds due to outer disk erosion by the strong UV radiation. However, we are cautious with any further interpretation because the SpT range in the A0–K4 median is broad and the median cannot represent general characteristics of objects in a narrow range of SpTs.

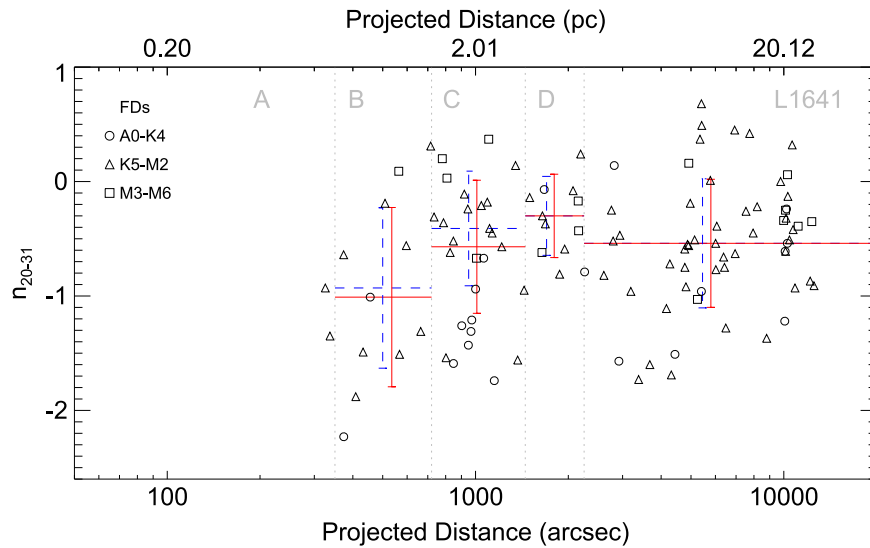


Figure 27. Variation of n_{20-31} with projected distance from θ^1 Ori C. The open symbols indicate the SpT ranges to which an object belongs: circle for A0–K4; triangle for K5–M2; square for M3–M6. The dashed horizontal lines indicate the n_{20-31} median of objects in the K5–M2 group in each subsection, which is indicated in Figures 1 and 2. The solid horizontal lines indicate the median of all objects from A to M type in each subsection. The error bars on the medians are taken from the standard deviation of n_{20-31} in each subsection.

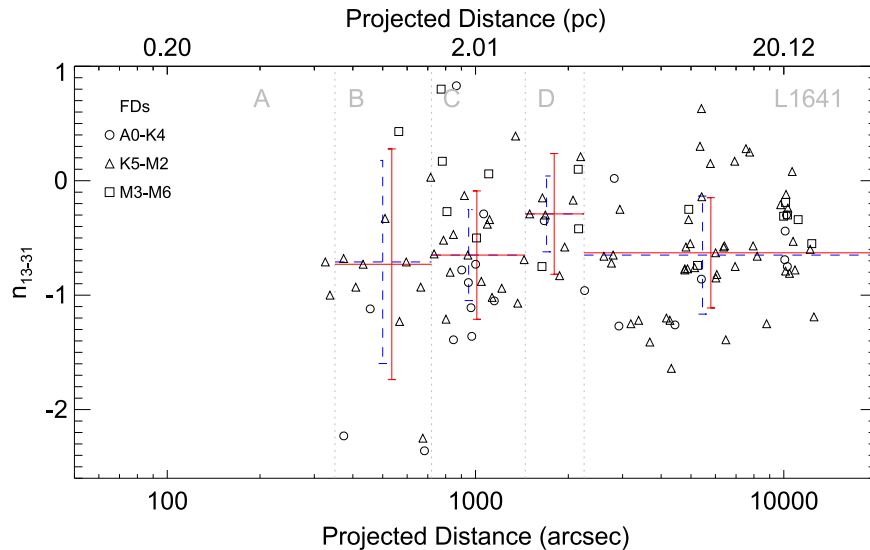


Figure 28. Variation of n_{13-31} with projected distance from θ^1 Ori C. The meanings of symbols are the same as in Figure 27. The dashed horizontal lines indicate the n_{13-31} median of objects in the K5–M2 group in each subsection, which is indicated in Figures 1 and 2. The solid horizontal lines indicate the median of all objects from A to M type in each subsection. The error bars on the medians are taken from the standard deviation of n_{13-31} in each subsection.

6. ENVIRONMENTAL EFFECTS AND EVOLUTIONARY FEATURES OF THE OUTER DISKS

The Orion A star-forming region is a much richer environment than Taurus and Cha I, in which the stellar density is small throughout, and the UV radiation field is not much larger than the interstellar field. However, most stars form in denser clusters containing high-mass stars (Lada et al. 1991; Carpenter 2000; Lada & Lada 2003; Evans et al. 2009; Koenig & Leisawitz 2014; Megeath et al. 2016), like Orion. Not only the high stellar density in Orion but also the strong ionizing radiation from OB associations affect the evolution of protoplanetary disks. The evidence of action of photoevaporative winds from the Trapezium cluster over the outer disks of protoplanetary disks within or near the Orion Nebula—“proplyds”—was observed by the *Hubble Space Telescope* (O’Dell

& Wen 1994): comet-shaped ionized gas clouds surrounding each disk, and smaller-than-usual disk sizes measured directly from the disk silhouette. The outward truncation of proplyds in the ONC has been detected at a submillimeter wavelength with Atacama Large Millimeter/submillimeter Array (Mann et al. 2014).

To better test this hypothesis of outer disk ablation by UV radiation from the Trapezium with IRS spectra, we construct a spectral index sensitive to the optically thick continuum of the outer disk ($r > 5$ AU from 5 to 37 μm coverage of IRS) and the optically thin small dust grains in the surface of the outer disk, n_{20-31} . The anchor points for 20 and 31 μm are the same as indicated in Section 4.2, 19.7–19.95 μm and 30.3–31 μm , respectively. The measured n_{20-31} and the projected distances (d) of objects from θ^1 Ori C are listed in Table 11.

We present the variation of n_{20-31} over a finer scale of distance by plotting n_{20-31} and the projected distance of each target from θ^1 Ori C in Figure 27. In the figure, we use three different symbols to break the objects into three subgroups of SpT ranges as defined in Section 5.3 for the median spectra discussion. This is to examine patterns that are dependent on properties of host stars, if any exist. At first glance, we notice that the objects of the A0–K4 group have generally low n_{20-31} , while the objects of the M3–M6 group are located on the rather higher side of n_{20-31} . We measure the K5–M2 median and the median of all objects of n_{20-31} of each subregion to see the general pattern better with the scattered data points in Figure 27. From the medians and the distribution of scattered data points, we see that n_{20-31} of FDs in region B increases as the projected distance, d , increases. At greater distance ($d > 1.5$ pc), we do not see the steep variation pattern of n_{20-31} as seen in region B, through region C to L1641.

The distribution of n_{13-31} with the projected distance is shown in Figure 28. Even though the declining pattern of n_{13-31} closer to θ^1 Ori C is not as remarkable as shown for n_{20-31} , there is also a weak declining tendency for n_{13-31} in B and C. We also notice that some objects show a significant drop of n_{13-31} in the B region.

It seems that the effect of UV illumination by the Trapezium stars, if that is the dominant one, is largest within 1.5 pc (~ 730 arcsec) from θ^1 Ori C, based on the observed variation patterns of n_{20-31} and n_{13-31} . Combining the clues acquired from the observed variation pattern in the distribution of n_{20-31} and n_{13-31} along the projected distance, we suggest a possible solution to explain our observations. Considering that n_{20-31} is the index combining optically thin small grains and the optically thick continuum while n_{13-31} more directly represents continuum variation, we infer that evaporation of small particles and gases on the surface of the outer disk may be dominant and faster than the outward truncation of the optically thick disk itself. This may be consistent with outward truncation of the disks by the photoevaporative disk erosion and small dust removal as seen in stars closer (< 0.5 pc) to O-type stars in NGC 2244 (Balog et al. 2007, 2008). The ablation of the outer disks is also seen in the disks closer to the central star (O9) in the σ Ori cluster from the smaller infrared excess at 70 and 160 μm from PACS observation than disk-bearing objects located far from the massive star (J. Hernández et al. 2014, personal communication).

We examine the parameters useful to infer the evolutionary status of inner disks ($r < 1$ AU), n_{K-6} , EW10, F_{10} , and $F_{11.3}/F_{9.8}$ via distance from θ^1 Ori C. We do not see any prominent dependence of the parameters on a target’s separation from θ^1 Ori C. An interpretation is that the external UV radiation can affect the outer disks where the thermal velocities of the ionized heated gas exceed the escape velocity from the central stars, but does not affect the inner disk much. On the other hand, as we have discussed in Section 5.2, if an object is located much closer to the UV source, the inner disk can be influenced by the UV radiation. However, we do not make any detailed inference about the environmental effect on the inner disk evolution based on our observations of n_{K-6} , EW10, F_{10} , and $F_{11.3}/F_{9.8}$.

7. SUMMARY AND CONCLUSION

We present IRS/*Spitzer* observations of 319 Class II disks in Orion A. We also present SpeX spectra of 120 objects and

report mass accretion rates measured from hydrogen recombination lines in SpeX spectra. We analyzed the distributions of stellar, disk, and dust properties of our objects. We compared their distributions separated by subregions in Orion A, and we also compared the properties of Orion A disks with those of disks in the Taurus star-forming region. We draw the following conclusions from the analysis done in this work:

1. The median visual extinction A_V is larger in L1641 than the ONC and the Trapezium. It confirms the effect of strong UV radiation from OB stars in the Trapezium to blow out small dust grains near them.
2. We confirm that the \dot{M} distribution of TDs in the ONC and L1641 is about a factor of 10 lower than that of FDs. The median \dot{M} of FDs in the ONC and L1641 are $1.55 \times 10^{-8} M_\odot \text{yr}^{-1}$ and $1.01 \times 10^{-8} M_\odot \text{yr}^{-1}$, respectively. The median \dot{M} of TDs in the ONC and L1641 are $1.95 \times 10^{-9} M_\odot \text{yr}^{-1}$ and $1.62 \times 10^{-9} M_\odot \text{yr}^{-1}$, respectively. When we compared \dot{M} for disks in the ONC and that of L1641 separately, the distribution of \dot{M} in the ONC is slightly skewed toward a higher value, but there is no statistically significant difference in \dot{M} between the ONC and L1641 when the same disk groups (FD versus FD; TD versus TD) in two subregions are compared.
3. We have compared disk properties between FDs in Orion A subregions and FDs in Taurus. We found that n_{K-6} and n_{6-13} , which probe the inner regions of disks, tend to be statistically significantly higher in the ONC compared with Taurus. We also notice that the distribution of EW10 in the ONC is statistically significantly shifted from that of Taurus toward higher values and that in L1641 is distributed in between those of the ONC and Taurus. We also detected possible evolution of the degrees of grain growth and crystallization from $F_{11.3}/F_{9.8}$ in different star-forming regions following their median ages (NGC 1333, the ONC, L1641, Tau, Cha I). By comparing the 10 μm silicate features of median spectra after subtracting continuum and normalization to the continuum, we confirmed that the ONC profile of 10 μm features is much smoother and narrower, similar to the profile of pristine silicate features, while the profile of L1641 indicates grain growth and crystallization, similar to Taurus. However, unlike the indicators of different properties of small dust grains, EW10 and $F_{11.3}/F_{9.8}$, we found no significant differences in the “sedimentation index” n_{13-31} among the ONC, L1641, and Taurus. All of these findings support the notion that the disk evolution occurs faster in the inner regions and the dust processing timescale is faster than the disk sedimentation timescale. Considering the median age of the ONC (< 1 Myr), L1641 (~ 1 Myr), and Taurus (2 Myr), grain growth and crystallization are increased in the 1–2 Myr age range.
4. We have searched for trends between disk parameters and the strength of the UV illumination upon the disks. From the examination of median spectra in subsections of Orion A, we found that the median spectra of the subsections of the ONC are blue at long wavelengths beyond 20 μm , which is consistent with outward truncation of the disks due to the UV radiation field from the Trapezium, as in the case for the proplyds. We compared the distributions of spectral indices, equivalent widths, and integrated fluxes with the variation of the

distance of objects from θ^1 Ori C. We observed a remarkable decline of n_{20-31} toward the center of the Trapezium. The distribution of n_{13-31} shows a similar declining pattern. These decreasing trends of n_{20-31} and n_{13-31} are dominantly observed within 1.5 pc from θ^1 Ori C. Considering the definitions and the implications of the parameters studied in this work, we suggest a depletion of optically thin surface material of the outer disk ($r \gtrsim 1-10$ AU).

The IRS survey of protoplanetary disks in Orion A presented in this work opens a new catalog of protoplanetary disks by offering disk properties measured from IRS spectra. We will discuss how the properties are interactively related to each other in the next paper. Future observations of the objects in this work with instruments capable of greater angular resolution and sensitivity in multiwavelength ranges from IR to submillimeter/millimeter will enhance our understanding of the process of disk evolution and planet formation.

This work is based on observations made with the *Spitzer Space Telescope*, which is operated by the Jet Propulsion Laboratory, California Institute of Technology, under NASA contract 1407. Support for this work was provided by NASA through Contract Number 1257184 issued by JPL/Caltech, and Cornell subcontracts 31419-5714 to the University of Rochester. This publication makes use of data products from the Two Micron All Sky Survey, which is a joint project of the University of Massachusetts and the Infrared Processing and Analysis Center/California Institute of Technology, funded by the National Aeronautics and Space Administration and the National Science Foundation. This research has made use of the SIMBAD database, operated at CDS, Strasbourg, France. This research has made use of the VizieR catalog access tool, CDS, Strasbourg, France. The original description of the VizieR service was published in *A&AS*, 143, 23. This publication makes use of data products from the *Wide-field Infrared Survey Explorer*, which is a joint project of the University of California, Los Angeles, and the Jet Propulsion Laboratory/California Institute of Technology, funded by the National Aeronautics and Space Administration. Funding for SDSS-III has been provided by the Alfred P. Sloan Foundation, the Participating Institutions, the National Science Foundation, and the US Department of Energy Office of Science. SDSS-III is managed by the Astrophysical Research Consortium for the Participating Institutions of the SDSS-III Collaboration, including the University of Arizona, the Brazilian Participation Group, Brookhaven National Laboratory, University of Cambridge, Carnegie Mellon University, University of Florida, the French Participation Group, the German Participation Group, Harvard University, the Instituto de Astrofísica de Canarias, the Michigan State/Notre Dame/JINA Participation Group, Johns Hopkins University, Lawrence Berkeley National Laboratory, Max Planck Institute for Astrophysics, Max Planck Institute for Extraterrestrial Physics, New Mexico State University, New York University, Ohio State University, Pennsylvania State University, University of Portsmouth, Princeton University, the Spanish Participation Group, University of Tokyo, University of Utah, Vanderbilt University, University of Virginia, University of Washington, and Yale University. The UKIDSS project is defined in Lawrence et al. (2007). UKIDSS uses the UKIRT Wide Field Camera (WFCAM; Casali et al. 2007). The photometric system is described in Hewett et al. (2006),

and the calibration is described in Hodgkin et al. (2009). The pipeline processing and science archive are described in P. G. J. Irwin et al. (in preparation) and Hambly et al. (2008). K.H.K. was a visiting Astronomer at the Infrared Telescope Facility, which is operated by the University of Hawaii under contract NNH14CK55B with the National Aeronautics and Space Administration.

Facilities: *Spitzer* (IRS), IRTF (SpeX).

REFERENCES

- Adams, F. C., Lada, C. J., & Shu, F. H. 1988, *ApJ*, 326, 865
 Aihara, H., Allende Prieto, C., An, D., et al. 2011, *ApJS*, 195, 26A
 Allen, L. E. 1995, PhD thesis, School of Physics, Univ. New South Wales
<http://lea@newt.phys.unsw.edu.au>
 Andre, P., Ward-Thompson, D., & Barsony, M. 1993, *ApJ*, 406, 122
 Andrews, S. M., Wilner, D. J., Espaillat, C., et al. 2011, *ApJ*, 732, 42
 Arnold, L. A., Watson, D. M., Kim, K. H., et al. 2012, *ApJS*, 201, 12
 Balog, Z., Muzerolle, J., Rieke, G. H., et al. 2007, *ApJ*, 660, 1532
 Balog, Z., Rieke, G. H., Muzerolle, J., et al. 2008, *ApJ*, 688, 408
 Bertout, C., Siess, L., & Cabrit, S. 2007, *A&A*, 473, L21
 Bessell, M. S., & Brett, J. M. 1988, *PASP*, 100, 1134
 Bouwman, J., Henning, T., Hillenbrand, L. A., et al. 2008, *ApJ*, 683, 479
 Calvet, N., D'Alessio, P., Watson, D. M., et al. 2005, *ApJL*, 630, L185
 Caratti O Garatti, A., Garcia Lopez, R., Antonucci, S., et al. 2012, *A&A*, 538, A64
 Cardelli, J. A., Clayton, G. C., & Mathis, J. S. 1989, *ApJ*, 345, 245
 Carpenter, J. M. 2000, *AJ*, 120, 3139
 Casali, M., Adamson, A., Alves de Oliveira, C., et al. 2007, *A&A*, 467, 777
 Casassus, S., van der Plas, G., Perez, S., et al. 2013, *Natur*, 493, 191
 Crapsi, A., van Dishoeck, E. F., Hogerheijde, M. R., Pontoppidan, K. M., & Dullemond, C. P. 2008, *A&A*, 486, 245
 Currie, T., Lada, C. J., Plavchan, P., et al. 2009, *ApJ*, 698, 1
 Cushing, M. C., Rayner, J. T., & Vacca, W. D. 2005, *ApJ*, 623, 1115
 Cushing, M. C., Vacca, W. D., & Rayner, J. T. 2004, *PASP*, 116, 362
 Cutri, R. M., et al. 2012, *yCat*, 2311, 0
 da Rio, N., Robberto, M., Soderblom, D. R., et al. 2010, *yCat*, 218, 30261
 Daemgen, S., Correia, S., & Petr-Gotzens, M. G. 2012, *A&A*, 540, A46
 D'Alessio, P., Calvet, N., Hartmann, L., Franco-Hernández, R., & Servín, H. 2006, *ApJ*, 638, 314
 D'Alessio, P., Calvet, N., Hartmann, L., Lizano, S., & Cantó, J. 1999, *ApJ*, 527, 893
 DENIS Consortium 2005, VizieR Online Data Catalog, 2263
 Espaillat, C., Calvet, N., D'Alessio, P., et al. 2007, *ApJL*, 670, L135
 Espaillat, C., Ingleby, L., Hernández, J., et al. 2012, *ApJ*, 747, 103
 Espaillat, C., Muzerolle, J., Najita, J., et al. 2014, *Protostars and Planets VI*, 497
 Evans, N. J., II, Dunham, M. M., Jørgensen, J. K., et al. 2009, *ApJS*, 181, 321
 Fang, M., Kim, J. S., van Boekel, R., et al. 2013, *ApJS*, 207, 5
 Fang, M., van Boekel, R., Wang, W., et al. 2009, *A&A*, 504, 461
 Fűrész, G., Hartmann, L. W., Megeath, S. T., Szentgyorgyi, A. H., & Hamden, E. T. 2008, *ApJ*, 676, 1109
 Furlan, E., Hartmann, L., Calvet, N., et al. 2006, *ApJS*, 165, 568
 Furlan, E., Luhman, K. L., Espaillat, C., et al. 2011, *ApJS*, 195, 3
 Furlan, E., McClure, M., Calvet, N., et al. 2008, *ApJS*, 176, 184
 Furlan, E., Watson, D. M., McClure, M. K., et al. 2009, *ApJ*, 703, 1964
 Gälfalk, M., & Olofsson, G. 2008, *A&A*, 489, 1409
 Gatti, T., Natta, A., Randich, S., Testi, L., & Sacco, G. 2008, *A&A*, 481, 423
 Getman, K. V., Feigelson, E. D., & Kuhn, M. A. 2014, *ApJ*, 787, 109
 Glebocki, R., & Gnacinski, P. 2005, *yCat*, 3244, 0
 Frankin, K. N., Melnikov, S. Y., Bouvier, J., Herbst, W., & Shevchenko, V. S. 2007, *A&A*, 461, 183
 Greene, T. P., Wilking, B. A., Andre, P., Young, E. T., & Lada, C. J. 1994, *ApJ*, 434, 614
 Hambly, N. C., Collins, R. S., Cross, N. J. G., et al. 2008, *MNRAS*, 384, 637
 Herbig, G. H., & Bell, K. R. 1988, Third Catalog of Emission-Line Stars of the Orion Population Lick Observatory Bulletin #1111 (*Jun 1988*) ed. G. H. Herbig & K. R. Bell (Santa Cruz: Lick Observatory), p 90, 1111
 Hernández, J., Calvet, N., Briceño, C., et al. 2007, *ApJ*, 671, 1784
 Hewett, P. C., Warren, S. J., Leggett, S. K., & Hodgkin, S. T. 2006, *MNRAS*, 367, 454
 Higdon, S. J. U., Devost, D., Higdon, J. L., et al. 2004, *PASP*, 116, 975
 Hillenbrand, L. A. 1997, *AJ*, 113, 1733
 Hillenbrand, L. A., & Carpenter, J. M. 2000, *ApJ*, 540, 236

- Hillenbrand, L. A., Hoffer, A. S., & Herczeg, G. J. 2013, *AJ*, 146, 85
- Hodgkin, S. T., Irwin, M. J., Hewett, P. C., & Warren, S. J. 2009, *MNRAS*, 394, 675
- Honda, M., Katata, H., Okamoto, Y. K., et al. 2006, *ApJ*, 646, 1024
- Houk, N., & Swift, C. 2000, *yCat*, 3214, 0
- Hsu, W.-H., Hartmann, L., Allen, L., et al. 2012, *ApJ*, 752, 59
- Hsu, W.-H., Hartmann, L., Allen, L., et al. 2013, *ApJ*, 764, 114
- Kenyon, S. J., & Hartmann, L. 1995, *ApJS*, 101, 117
- Kessler-Silacci, J., Augereau, J.-C., Dullemond, C. P., et al. 2006, *ApJ*, 639, 275
- Kim, K. H., Watson, D. M., Manoj, P., et al. 2009, *ApJ*, 700, 1017
- Kim, K. H., Watson, D. M., Manoj, P., et al. 2013, *ApJ*, 769, 149
- Koenig, X. P., & Leisawitz, D. T. 2014, *ApJ*, 791, 131
- Kukarkin, B. V., Kholopov, P. N., Pskovskiy, Y. P., et al. 1971, General Catalogue of Variable Stars (3rd ed.) 1971
- Lada, C. J. 1987, *Star Forming Regions*, 115, 1
- Lada, C. J., & Lada, E. A. 2003, *ARA&A*, 41, 57
- Lada, E. A., Depoy, D. L., Evans, N. J., II, & Gatley, I. 1991, *ApJ*, 371, 171
- Lawrence, A., Warren, S. J., Almaini, O., et al. 2007, *MNRAS*, 379, 1599
- Lebouteiller, V., Bernard-Salas, J., Sloan, G. C., & Barry, D. J. 2010, *PASP*, 122, 231
- Lubow, S. H., & D'Angelo, G. 2006, *ApJ*, 641, 526
- Mann, R. K., Di Francesco, J., Johnstone, D., et al. 2014, *ApJ*, 784, 82
- Manoj, P., Bhatt, H. C., Maheswar, G., & Muneer, S. 2006, *ApJ*, 653, 657
- Manoj, P., Kim, K. H., Furlan, E., et al. 2011, *ApJS*, 193, 11
- Mathis, J. S. 1990, *ARA&A*, 28, 37
- McClure, M. 2009, *ApJL*, 693, L81
- McClure, M. K., Furlan, E., Manoj, P., et al. 2010, *ApJS*, 188, 75
- Megeath, S. T., Fischer, W., Ali, B., et al. 2010, *BAAS*, 42, 215
- Megeath, S. T., Gutermuth, R., Muzerolle, J., et al. 2012, *AJ*, 144, 192
- Megeath, S. T., Gutermuth, R., Muzerolle, J., et al. 2016, *AJ*, 151, 5
- Menten, K. M., Reid, M. J., Forbrich, J., & Brunthaler, A. 2007, *A&A*, 474, 515
- Meyer, M. R., Calvet, N., & Hillenbrand, L. A. 1997, *AJ*, 114, 288
- Muzerolle, J., Hartmann, L., & Calvet, N. 1998, *AJ*, 116, 2965
- Najita, J. R., Andrews, S. M., & Muzerolle, J. 2015, *MNRAS*, 450, 3559
- Najita, J. R., Strom, S. E., & Muzerolle, J. 2007, *MNRAS*, 378, 369
- Ochsenbein, F. 1980, *BICDS*, 19, 74
- O'Dell, C. R., & Wen, Z. 1994, *ApJ*, 436, 194
- Olofsson, J., Augereau, J.-C., van Dishoeck, E. F., et al. 2009, *A&A*, 507, 327
- Olofsson, J., Benisty, M., Augereau, J.-C., et al. 2011, *A&A*, 528, L6
- Parenago, P. P. 1954, *TrSht*, 25, 1
- Parihar, P., Messina, S., Distefano, E., Shantikumar, N. S., & Medhi, B. J. 2009, *MNRAS*, 400, 603
- Pecaut, M. J., & Mamajek, E. E. 2013, *ApJS*, 208, 9
- Prisinzano, L., Micela, G., Flaccomio, E., et al. 2008, *ApJ*, 677, 401
- Przygodda, F., van Boekel, R., Àbrahàm, P., et al. 2003, *A&A*, 412, L43
- Rayner, J. T., Cushing, M. C., & Vacca, W. D. 2009, *ApJS*, 185, 289
- Rayner, J. T., Toomey, D. W., Onaka, P. M., et al. 2003, *PASP*, 115, 362
- Rebull, L. M. 2001, *AJ*, 121, 1676
- Rebull, L. M., Hillenbrand, L. A., Strom, S. E., et al. 2000, *AJ*, 119, 3026
- Riaz, B., Gizis, J. E., & Harvin, J. 2006, *AJ*, 132, 866
- Robberto, M., Soderblom, D. R., Scandariato, G., et al. 2010, *AJ*, 139, 950
- Robitaille, T. P., Whitney, B. A., Indebetouw, R., Wood, K., & Denzmore, P. 2006, *ApJS*, 167, 256
- Sargent, B. A., Forrest, W. J., Tayrien, C., et al. 2009, *ApJS*, 182, 477
- Shuping, R. Y., Kassis, M., Morris, M., Smith, N., & Bally, J. 2006, *ApJL*, 644, L71
- Siess, L., Dufour, E., & Forestini, M. 2000, *A&A*, 358, 593
- Skrutskie, M. F., Cutri, R. M., Stiening, R., et al. 2006, *AJ*, 131, 1163
- Tobin, J. J., Hartmann, L., Furesz, G., Mateo, M., & Megeath, S. T. 2009, *ApJ*, 697, 1103
- Tobin, J. J., Hartmann, L., Furesz, G., Mateo, M., & Megeath, S. T. 2013, *ApJ*, 773, 81
- UKIDSS Consortium 2012, *yCat*, 2314, 0
- Vacca, W. D., Cushing, M. C., & Rayner, J. T. 2003, *PASP*, 115, 389
- van Boekel, R., Min, M., Waters, L. B. F. M., et al. 2005, *A&A*, 437, 189
- Wall, J. V., & Jenkins, C. R. 2003, in *Practical Statistics for Astronomers*, ed. R. Ellis et al. (Cambridge: Cambridge Univ. Press)
- Watson, D. M., Kemper, F., Calvet, N., et al. 2004, *ApJS*, 154, 391
- Watson, D. M., Leisenring, J. M., Furlan, E., et al. 2009, *ApJS*, 180, 84
- Wolff, S. C., Strom, S. E., & Hillenbrand, L. A. 2004, *ApJ*, 601, 979
- Wouterloot, J. G. A., & Brand, J. 1992, *A&A*, 265, 144
- Zacharias, N., Monet, D. G., Levine, S. E., et al. 2005, *yCat*, 1297, 0